

Dissertation
submitted to the
Combined Faculties for the Natural Sciences and for
Mathematics
of the Ruperto-Carola University of Heidelberg, Germany
for the degree of
Doctor of Natural Sciences

Put forward by
Diplom-physicist: Daria Shubina
Born in: Irkutsk, Russia
Oral examination: October 31, 2012

Schottky mass measurements
of heavy neutron-rich nuclides
in the element range $70 \leq Z \leq 79$
at the ESR

Referees: Prof. Dr. Klaus Blaum
Prof. Dr. Thomas Stöhlker

Gegenstand dieser Dissertation ist die Schottky-Massen-Spektrometrie schwerer, neutronenreicher Nuklide zwischen den Protonenschalen $Z = 50$ und 82 . Dieser Bereich der Nuklidkarte ist noch nicht genau untersucht worden, obwohl die Nuklidmassen in diesem Gebiet essentiell für unser Verständnis der Kernstruktur und auch für den Ablauf der Nukleosynthese im r-Prozess sind. Die Messungen wurden 2009 am Ionenspeicherring ESR des GSI Helmholtzzentrums in Darmstadt durchgeführt. Die untersuchten interessanten Nuklide wurden aus der Fragmentation von ^{197}Au gewonnen. Experiment, Daten und deren Analyse werden im Detail in der vorliegenden Arbeit beschrieben. Die Datenanalyse erfolgte mit zwei unabhängigen Methoden, mittels der “Spline” Methode einerseits und einer Korrelationsmatrix andererseits. Vor- und Nachteile beider Methoden wurden im Detail untersucht und verglichen. Wichtige Ergebnisse dieser Arbeit sind u.a.: die erstmalige Bestimmung der Masse von neun Nukliden, $^{181,183}\text{Lu}$, $^{185,186}\text{Hf}$, $^{187,188}\text{Ta}$, ^{191}W und $^{192,193}\text{Re}$, sowie eine wesentlich genauere Bestimmung der Massen von drei Nukliden, $^{189,190}\text{W}$ und ^{195}Os . Ferner wurden Korrelationen im Verhalten von Zwei-Neutronen Separationsenergien und pairing-gap Energien jeweils mit kollektivem Verhalten der Nukleonen beobachtet und ausführlich diskutiert. Die physikalische Motivation für weitere Studien dieser Korrelationen, sowie die Perspektiven künftiger Massenmessungen in Speicherringen (einschließlich neuer, wie z.B. in Lanzhou) werden abschließend dargestellt.

The present thesis is dedicated to the Schottky mass spectrometry of heavy neutron-rich nuclides between proton shell closures at $Z = 50$ and 82 . This region on the chart of nuclides is not well-studied, though masses of these nuclides are indispensable for our understanding of nuclear structure and in turn of r-process nucleosynthesis. The measurements were conducted in 2009 at GSI employing ^{197}Au fragmentation to produce nuclei of interest. The experiment, data acquisition and data analysis are described in detail in this work. The data analysis was performed with two independent methods, namely spline and correlation-matrix approaches, advantages and disadvantages of which were investigated. The obtained results contain masses for nine nuclides, $^{181,183}\text{Lu}$, $^{185,186}\text{Hf}$, $^{187,188}\text{Ta}$, ^{191}W and $^{192,193}\text{Re}$, which were measured for the first time. Furthermore, mass uncertainties for three nuclides, $^{189,190}\text{W}$ and ^{195}Os , were improved. New data were used to investigate nuclear structure in this region. Correlations in behavior of two-neutron separation energies as well as nucleon pairing-gap energies each with nuclear collectivity have been observed and thoroughly discussed. Motivation for further studies of these correlations, as well as future perspectives of in-ring mass measurements worldwide are outlined.

Contents

Introduction	1
1 Nuclear binding energy	3
1.1 Nuclear mass models	4
1.1.1 Macroscopic-microscopic models	5
1.1.2 Microscopic nuclear models	6
1.1.3 State-of-the-art mass models	8
2 Mass spectrometry	9
2.1 History of mass measurements	9
2.2 Modern methods for mass measurements	11
2.2.1 Penning-trap mass spectrometry	11
2.2.2 Storage-ring mass spectrometry	12
2.2.3 Production and separation of exotic nuclei	13
2.3 Nuclear structure properties derived from mass values	14
2.4 Other applications of experimental mass data	19
3 Experiment	22
3.1 Experimental facilities of the GSI Helmholtz Center	22
3.1.1 Production target	22
3.1.2 The fragment separator FRS	25
3.1.3 The experimental storage ring ESR	26
3.2 Schottky Mass Spectrometry (SMS)	28
3.3 Data acquisition	30
4 Data analysis	32
4.1 Schottky frequency spectra	32
4.2 Correction for magnetic drifts	33
4.3 Peak finding procedure	33
4.4 Isotope identification	39
4.5 Reference masses	39
4.6 Mass evaluation	41
4.6.1 The correlation matrix method (CMM)	42

4.6.2	Spline method	45
5	Results and discussion	48
5.1	Mass values measured for the first time	48
5.2	Comparison to mass models	53
5.3	Two-neutron separation energies	54
5.4	Pairing-gap energies	58
6	Summary and outlook	61
6.1	Past and future of the ESR	61
6.2	CSRe storage ring	63
6.3	FAIR and ILIMA	63
	Appendices	67
A	The α_p curve	67
B	Software for data analysis	71
C	The correlation matrix method	72
	Bibliography	78

Introduction

Owing to the fact, that human thought precedes human action, the idea that everything consist of atoms was proposed more than 2000 years before it could be proven to exist.

After the discovery of the first subatomic particle, the electron, in 1897, the necessity to describe the atomic structure appeared. The development of atomic models went all the way — from J.J. Thomson’s plum pudding model (1904) through Rutherford’s planetary (1911) and Bohr (1913) models to a quantum description of the atom — amazingly fast: within only twenty years [1].

However, an accurate description of the atomic nucleus still remains a challenge. The residual strong, weak and electromagnetic interactions take place in it. However, these forces have significantly different ranges and therefore their action can be observed through different properties of atoms. The binding energy of the atomic nucleus is mainly dictated by the strong and Coulomb forces, while the lifetime of an unstable atom in respect to a β -decay is defined principally by the weak interaction.

Thus, in order to describe the atomic nucleus one has to study its various properties. A nucleus can also absorb energy and redistribute it between constituents in different ways. Therefore besides the binding energy and the lifetime, various nuclear excited states reveal the internal structure.

The present work concentrates on precision measurements of nuclear binding energies or, in other words, atomic masses, which is rather the same, as it will be shown in Chapter 1. There is only a finite number of nuclei that can exist in a form of bound particles, namely the nuclei between the so-called drip-lines. Neutron drip-line is a boundary of neutron emission, proton drip-line is the same for proton emission. The chart of nuclides is also limited by boundary of immediate spontaneous fission. Beyond these drip-lines nuclei can exist only as unbound resonances with lifetimes of about 10^{-18} – 10^{-24} s. Light nuclei are well-investigated within the limits of the drip-lines, while heavier isotopes provide huge unexplored areas of short-lived radioactive nuclides. As nuclei get heavier, complexity of the nucleonic many-body system increases drastically. Due to large number of nucleons, different effects in nuclear structure can take place (these effects will be discussed in Section 2.3). This work is aimed to investigate heavy radioactive nuclei in order to have a better understanding of their structure and collective effects in such nuclei. Moreover experimental data on these exotic nuclides can be used for many other

applications, as for example, new data are valuable for adjusting mass models in this region of the nuclidic chart, which in turn are used to calculate nuclear properties of even more exotic nuclei relevant for the understanding of stellar nucleosynthesis processes (see the discussion in Section 2.4).

Heavy neutron-rich nuclides in the region of $70 \leq Z \leq 79$ were investigated by means of Schottky mass spectrometry. These nuclides were produced by ^{197}Au fragmentation and investigated with the experimental storage ring ESR at GSI, Darmstadt. The experimental techniques, data analysis, mass evaluation as well as interpretation of obtained results are present in this work in detail. The last part of this thesis provides an outlook on future mass measurements.

CHAPTER 1

Nuclear binding energy

Forces in an atom can be separated in two main parts: interaction between the nucleus and the electrons and interaction between nucleons in the nucleus. Therefore the mass of an ion can be subdivided into three terms: nuclear mass, electron masses and electron binding energy

$$m_a = m_{nucl} + (Z - q) \cdot m_e - B_e(Z, (Z - q)), \quad (1.1)$$

where m_a is the atomic mass, m_{nucl} is the nuclear mass and m_e is the mass of the electron, Z is the atomic number of the nucleus, q is the charge state of an atom and $B_e(Z, (Z - q))$ is the electron binding energy of $Z - q$ electrons in the nucleus with Z protons.

The lightest atom is hydrogen with a mass of 0.939 GeV*, the heaviest measured mass according to [2] is the one of ^{269}Ds ($Z = 110$): about 251 GeV [3]. Since the electron is very light with respect to the nucleus, the mass of the latter corresponds to more than 99.95% of the mass of an atom. As an example, for ^{257}Fm ($Z = 100$): $m_a = 239482$ MeV, $m_{nucl} = 239432$ MeV, $100m_e = 51$ MeV and $B_e = 0.9$ MeV.

The electron mass is known up to about $10^{-14} u^\dagger$ [4]; the electron binding energies mainly depend on the atomic number only and are also well-known [5, 6]. That means, the atomic mass can easily be derived for an ion or a bare nucleus without losing too much in precision.

The mass of a nucleus m_{nucl} can be divided into different components:

$$m_{nucl} = Z \cdot m_p + N \cdot m_n - B(Z, N), \quad (1.2)$$

where m_p and m_n are the proton and the neutron masses, respectively, and $B(Z, N)$ is the nuclear binding energy. The latter is the quantity that reflects all interactions of the nuclear many body system. However, its value contributes to less than 1% of the total nuclear mass. The binding energy per nucleon B/A , where $A = Z + N$ is the mass number,

*in natural units, $c = 1$

† u is the unified atomic mass unit defined as $\frac{1}{12}m(^{12}\text{C})$, $u = 931494$ keV [7]

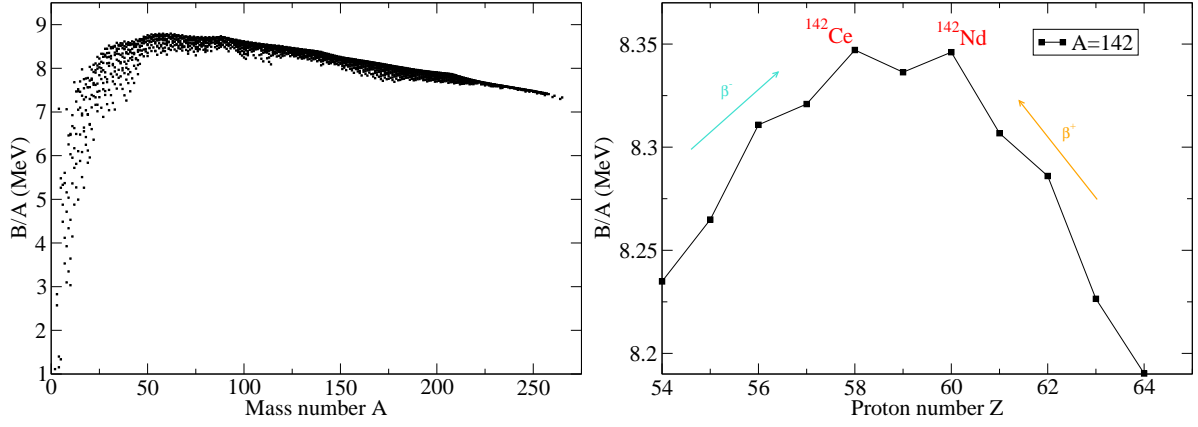


Fig. 1.1: Left panel: binding energy per nucleon as a function of mass number A . Only experimentally investigated nuclides are presented (from [7]). Right panel: the nuclear binding energy per nucleon as a function of proton number Z for the mass number $A = 142$. Stable elements of this isobar, ^{142}Ce and ^{142}Nd , are marked in red and have the highest binding energy per nucleon among these isobars.

shows how tightly nucleons are bound in the nucleus. The nuclear binding energy per nucleon as a function of A is shown in Fig. 1.1 (left panel). One can see that the largest binding energy per nucleon corresponds to the iron-nickel region. In the right panel the binding energy per nucleon for a given isobar ($A = 142$) is shown. Stable isotopes have the highest B/A values, while the others, less bound isobars ($A = \text{const}$), decay to these stable ones via β^- or β^+ decays. The odd-even staggering reflects pairing forces between the nucleons of the same type, that is, proton-proton and neutron-neutron correlations.

The proton and the neutron masses are well-defined, therefore the nuclear binding energy can precisely be derived from the atomic mass.

Besides the nuclear binding energy $B(Z, N)$ there is one other quantity, which is often used in topics related to nuclear masses. It is the mass excess $ME(Z, N)$, which is defined as

$$ME(Z, N) = m_a - A \cdot u. \quad (1.3)$$

The ME shows whether a given nucleus is more strongly bound than the ^{12}C nucleus (positive values) or less (negative values).

1.1

Nuclear mass models

In order to model the binding energy of an object, the knowledge of its structure as well as the interactions between the constituents is indispensable. As mentioned above inside the atomic nucleus the residual strong as well as the weak and the electromagnetic forces take place. During the last century many aspects of nuclear structure were investigated, such as shell closures, pairing correlations, different kinds of deformations, etc. These investigations gave rise to ideas that are used in contemporary mass models.

However, at the moment there is a variety of nuclear mass models, which use fundamentally different approaches to describe the nuclear interactions. Mass models are conventionally divided into two main classes: macroscopic-microscopic and microscopic. The former considers a nucleus as one object with complex internal properties, while the latter considers the nucleus as a composite of many simple interacting objects.

It should also be mentioned that in addition to mass models there are local mass formulas, which are aimed to extrapolate isotope masses beyond the region of experimentally measured values relying on the smooth behavior of the mass surface. The first example of this is AME-table predictions based on systematic trends of separation energies and Q -values [7]. Another example is the Garvey-Kelson relationship, which derives a certain mass based on six neighboring nuclidic masses [8, 9].

Another interesting approach to mass modeling is the so-called *ab-initio* theory with no free parameters. Based on experimental nucleon-nucleon (NN) scattering data, a two-body interaction potential can be constructed from the first principles to describe light nuclei with $A = 3$ or 4 . Usage of quantum Monte-Carlo method allows to describe nuclei up to $A = 8$ [10].

More information about state-of-the-art mass models can be found in [11, 12].

1.1.1. Macroscopic-microscopic models Under a macroscopic model of the nucleus the Bethe and Weizsäcker semi-empirical mass formula for the binding energy is understood as [13, 14]:

$$B(N, Z) = a_V A + a_S A^{2/3} + a_C \frac{Z^2}{A^{1/3}} + a_I \frac{(N - Z)^2}{A} - \delta(A), \quad (1.4)$$

where a_V , a_S , a_C and a_I are volume, surface, Coulomb and isospin coefficients, respectively. The volume and surface terms, due to which the formula is also named as “the liquid drop model”, reflect the fact that the binding energy is given by the counterplay between the volume and the surface tension. The third term reflects Coulomb repulsion between protons. The forth, the isospin term, corresponds to the asymmetry energy that originates from quantum levels filling. This can be understood considering the Pauli principle, according to which protons and neutron occupy higher levels in their potential wells as their numbers increase. Since protons and neutrons have different quantum number, i.e. the isospin, they have separate wells. Therefore, it is energetically preferable to fill both wells equally, without asymmetry between proton and neutron numbers. The last term in the formula, $\delta(A)$, is due to the pairing effect, because nuclei with even numbers of protons or neutrons are more strongly bound (see Fig. 1.1).

This formula can describe general trends in the binding energy as a function of mass number. However, it requires many additional improvements of microscopical nature to be able to follow the shell structure, such as the Strutinski shell correction [15]. Moreover, because of the pairing between nucleons of the same type, corrections for this phenomenon

are also needed, which can be done using, for example, pairing corrections based on the Bardeen-Cooper-Schrieffer (BCS) theory [16].

There is a large number of modern macroscopic-microscopic models, which are based on the liquid drop model but with further improvements. They take into account that, e.g. Coulomb, volume as well as surface tension terms depend on nuclear deformations.

Macroscopic-microscopic models are among the most accurate models, when speaking about the reliability of mass prediction. The best-known model is the Finite-Range-Droplet-Model (FRDM) of Möller, Nix, Myers and Swiatecki [17]. It is worth mentioning that a new, even further improved version has been published in 2012 [18]. For completeness one should mention that there are local macroscopic-microscopic models which are tuned to specific regions. For instance, a model of Sobiczewski et. al. can best describe the heavy and superheavy elements [19]. The model from Liran, Marinov and Zeldes [20] however, is adjusted in the region between the Z and N magic numbers and still holds the predictive-power record among the global models that are used to calculate the entire chart of nuclides with a unique set of free parameters.

1.1.2. Microscopic nuclear models The microscopic approach considers interactions of individual particles in a nucleus. The simplest approximation is to describe the nucleus as a system of independent particles moving in a “mean” field with a large mean-free path. This is the basis of the so-called shell model. It can be described with a one-body Schrödinger equation:

$$H\varphi(\vec{r}) = \left[-\frac{\hbar^2}{2m} \nabla^2 + V(r) \right] \varphi(\vec{r}) = E\varphi(\vec{r}), \quad (1.5)$$

where $V(r)$ is a central potential, in which particles are moving.

In the simplest approach, a square-well potential is used:

$$\begin{aligned} V(r) &= -V_0 & r &\leq R \\ V(r) &= \infty & r &> R, \end{aligned} \quad (1.6)$$

where $r = R$ is the radius of the nuclear surface. Other potential can also be used like, e.g., the harmonic oscillator potential:

$$V(r) = -V_0 \left[1 - \left(\frac{r}{R} \right)^2 \right] = \frac{m}{2} \omega_0^2 (r^2 - R^2), \quad (1.7)$$

where ω_0 is the oscillator frequency. Or the Woods-Saxon potential [21]:

$$V(r) = -V_0 \left[1 + \exp \left(\frac{r - R}{a} \right) \right]^{-1}, \quad (1.8)$$

where a is the diffuseness.

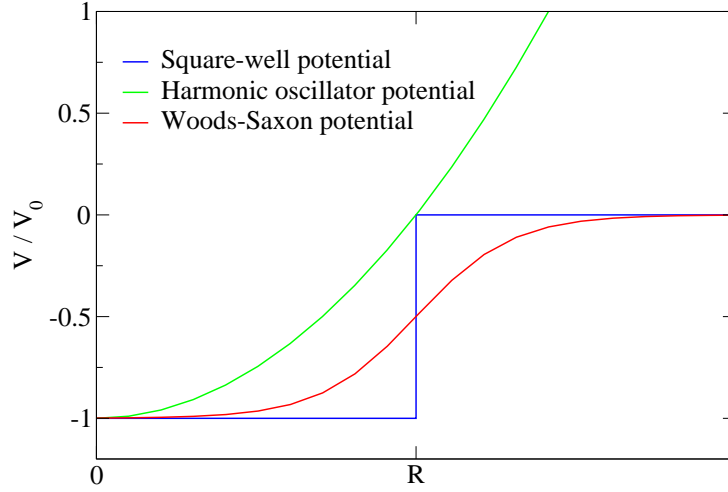


Fig. 1.2: Various types of single-particle nuclear potentials.

These three potentials are shown in Fig. 1.2. With these potentials the shell closures $N_p = N_n = 2, 8$ and 20 can be reproduced, but not the shell closures for the heavier nuclides. The latter however are well-known experimentally.

The next step would be considering the spin orbit or $\mathbf{l}s$ coupling. Similar to electrons in atom, the spin dependent force leads to the splitting of otherwise degenerated levels. This splitting was experimentally observed. However, note that unlike electrons with $l-s$, the lowest energy state of the nucleons is $l+s$. The shell model improved by incorporating strong spin orbit term into single particle Hamiltonian [22, 23] can correctly reproduce all magic numbers.

A further improvement of microscopic nuclear forces is the consideration of the two-body and three-body interactions:

$$V = \sum_{i<j} V(i, j) + \sum_{i<j<k} V(i, j, k). \quad (1.9)$$

An example of such a potential can be zero-range Skyrme potentials, which describe nucleons as point objects interacting via two- and three-body δ -forces [24]:

$$\begin{aligned} V(i, j) &\propto \delta(\vec{r}_i - \vec{r}_j) \\ V(i, j, k) &\propto \delta(\vec{r}_i - \vec{r}_j)\delta(\vec{r}_j - \vec{r}_k). \end{aligned} \quad (1.10)$$

Another example of a two- and three- body potential are the finite-range Gogny potentials [25], which differ from zero-range Skyrme by the replacement of some δ -forces by a sum of Gaussians. To solve the Schrödinger equation with these two- and three-body potentials, the variational Hartree-Fock method [26, 27] is used in many theoretical approaches [28].

Another application of mean-field is the RMF (relativistic mean-field) model [29]. Although it has comparably small predictive power, it can automatically reproduce spin

Tab. 1.1: Some present mass models

FRDM [17]	Finite Range Drop Model	Macroscopic description of a nucleus with additional microscopic corrections
HFB [30, 31]	Hartree-Fock-Bogolyubov model	HFB mean-field approach with Skyrme or Gogny interactions
DZ [32]	Duflo-Zuker	HF model with a shell model parameterization

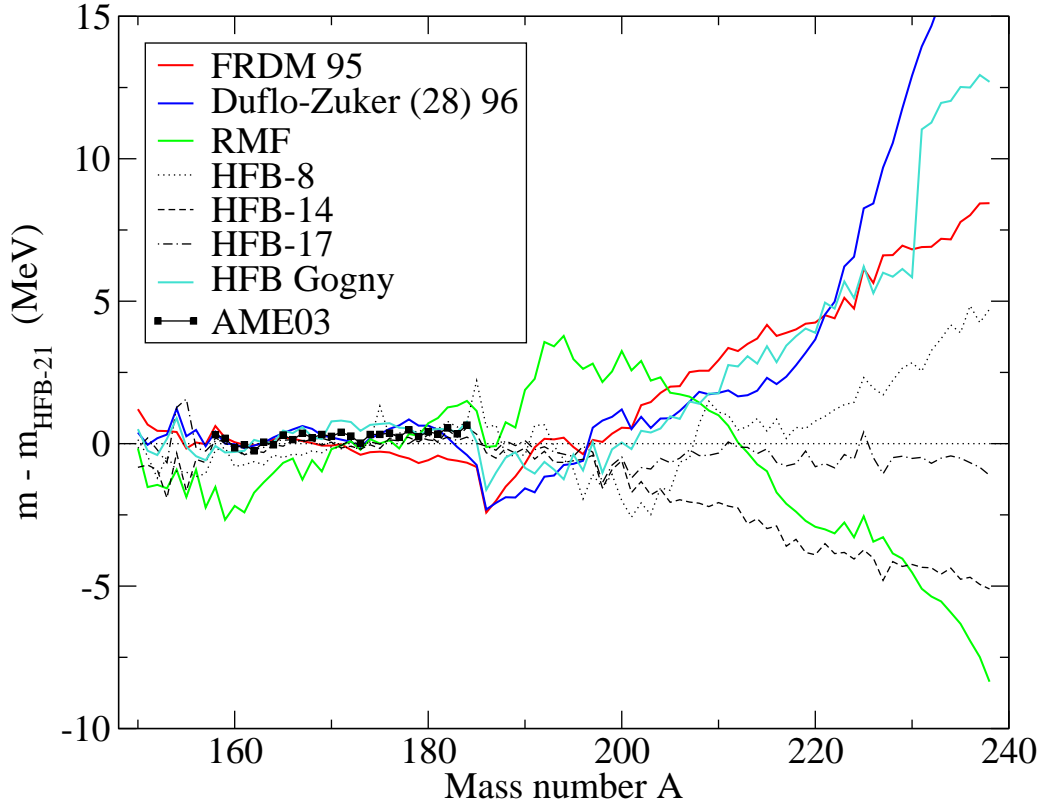


Fig. 1.3: Mass of hafnium isotopes by predictions of different theoretical mass models.

orbit coupling. The main disadvantage of mean-field approach is that the set of free parameters, which fits to existing data has unclear origin.

1.1.3. State-of-the-art mass models Some of mass models with good predictive power are listed in Tab. 1.1. The mass models quickly diverge in their predictions

beyond the experimentally investigated region (see Fig. 1.3).

This means, in spite of the variety of mass models, there are still different approaches to understanding of the nuclear structure. Therefore further experimental investigations are highly important for nuclear physics development.

CHAPTER 2

Mass spectrometry

Despite the fact that measuring atomic masses is one of the many tasks in nuclear physics, the whole branch of *mass measurements* is well-developed on its own: it serves not only the understanding of the nuclear structure, but also it can be treated as an individual topic in modern research with applications in nuclear and atomic physics, in astrophysics, in neutrino physics as well as in metrology, chemistry, biology, environmental radioprotection and safety, space missions, etc. The history of mass measurements, modern methods of mass spectrometry and direct applications of obtained results will be briefly discussed in this chapter.

2.1

History of mass measurements

To find out when the first attempt of atomic mass measurement was done, one needs to know, when it was realized that there is something to measure. It is interesting to track back on how human understanding came to the idea of a nuclide, — an atom consisting of a given number of protons and neutrons.

In fact, the history of chemical elements starts with the history of human being, because the oldest existing sample of copper is dated 6000 BC [33]. About ten metals were known already in antique. Therefore mankind knew about different — in a chemical sense — types of matter, but still had wrong ideas about the origin of these differences.

Medieval times gave birth to the idea of possible instability of elements embodied in alchemical attempts to transmute lead into gold [34]. And it is amazing that now such a "transmutation" can simply be done at many accelerator facilities.

Further developments in a more scientific way took place in 17th century with the distinction between chemistry and alchemy made by Robert Boyle [35]. And finally in 18th century chemistry became a full-fledged science as Antoine Lavoisier had done some quantitative observations [36].

It is interesting to note that until Lavoisier’s time (for about 300 years) people still thought there were four classical elements like water, earth, fire and air as elementary constituents. It was thought that metals transform into earth and fire-like element “phlogiston” in the combustion process [34].

Lavoisier made a first list of chemical elements, there were 23 of them. Eighty years later Dmitri I. Mendeleev arranged chemical elements into a periodic table, there were already 63 elements [37]. Nowadays there are 118 known elements [38], from which 20 are synthesized artificially in laboratory.

Chemical elements were originally arranged by their atomic weight*, most of the elements had a weight multiple to that of hydrogen. Nevertheless there was also chlorine with an atomic weight 35.5, which remained a puzzle until 1913, when isotopes were discovered. One year before the discovery, their existence was suggested by Frederick Soddy, who analyzed radioactive decay chains. In his work he noticed, that there must be 40 elements between lead and uranium, while the table allowed only 11 [39]. He received the 1921 Nobel Prize in chemistry for his formulation of the theory of isotopes.

Sir Joseph J. Thomson, who had been awarded the 1906 Nobel Prize in physics for the discovery of the electron, could separate neon-20 and neon-22 [40], thereby he discovered isotopes and opened up the field of mass spectrometry. Although about 2 decades still remained before the discovery of the neutron, the era of measurements of nuclidic masses began.

Francis W. Aston, Thomson’s student, built a mass spectrometer, which allowed him to identify isotopes of chlorine, bromine and krypton [41]. Aston was awarded the 1922 Nobel Prize in chemistry.

The first modern mass spectrometer was developed by Arthur J. Dempster in 1918; it allowed him to discover the uranium isotope ^{235}U in 1935. In 1932, Kenneth Bainbridge developed another spectrometer [42] to verify the equivalence of mass and energy $E = mc^2$ [43].

In 1954 nuclear-shape deformation was discovered by Benjamin G. Hogg and Henry E. Duckworth in the rare-earth region [44].

In 1970s at CERN Robert Klapisch and Catherine Thibault connected a mass spectrometer to an accelerator and were able to study unstable nuclei [45].

The resolving power of Thomson’s spectrometer was about $R=10$ ($R = \frac{M}{\Delta M} \approx \frac{20}{22-20}$ for the example ^{20}Ne and ^{22}Ne), Aston reached the resolving power of $R=2000$ in 1937, Dempster’s spectrometer had a resolving power of $R=3000$ and Bainbridge’s spectrometer had $R=10'000$ in 1936 [46]. Modern spectrometers have resolving powers of about $10^5 - 10^6$.

*average mass of an atom of a given chemical element; depends on the amount of different stable isotopes in an experimental sample

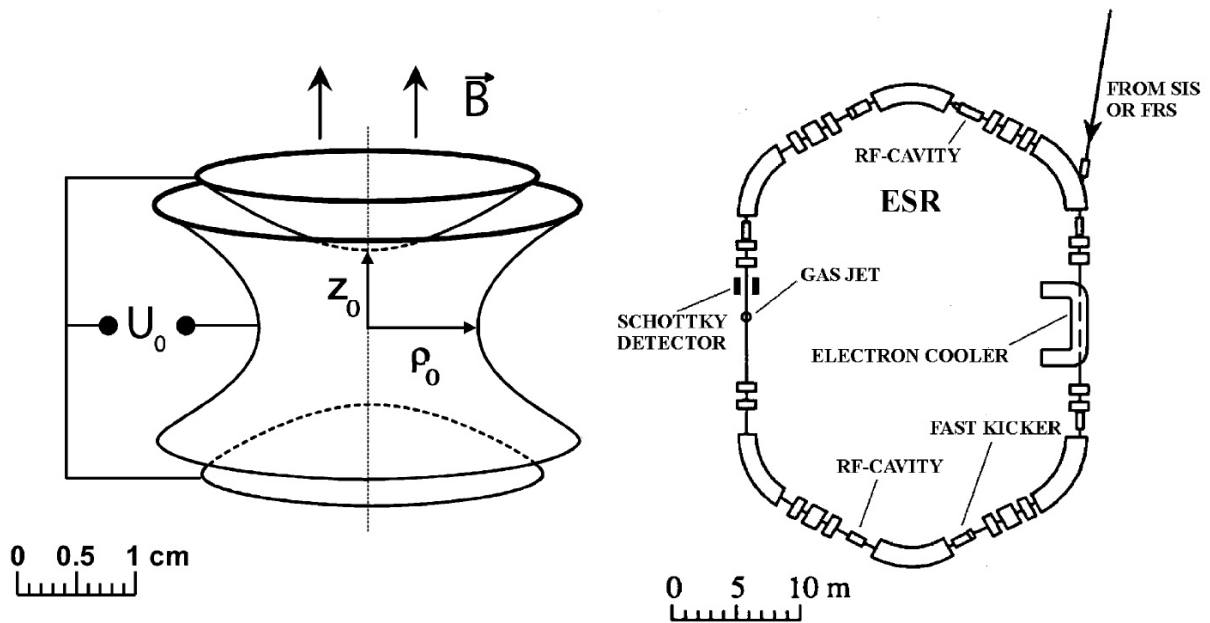


Fig. 2.1: A hyperbolic penning trap and a storage ring. From Ref. [54].

2.2

Modern methods for mass measurements

Nowadays a high-precision mass-measurement experiment on radioactive nuclei can be conducted with a Penning trap or with a storage ring, see in Fig. 2.1. On one side, penning traps are small devices, under 10 cm in size. They are relatively cheap and therefore there are many such devices in laboratories around the world. On the other side, storage rings that are used now for mass measurements of radioactive nuclides have circumferences of more than 100 meters and presently there are only two such rings in the world, namely, ESR in Darmstadt, Germany [47] and CSR in Lanzhou, China [48].

One should also note that there are other mass spectrometry techniques: indirect techniques, such as Q-value measurements from reactions (invariant-mass and missing-mass methods) or using a decay chain, which leads to known masses (superheavy elements' mass measurements), and direct techniques such as radiofrequency spectrometers (MISTRAL at CERN/ISOLDE [49]) or time-of-flight mass spectrometers (SPEG at GANIL [50]) [11] as well as a new TOF-B ρ method recently developed at Michigan State University [51].

2.2.1. Penning-trap mass spectrometry

The ion trap technique was developed in the second half of twentieth century, for which Hans G. Dehmelt and Wolfgang Paul [52, 53] received the 1989 Nobel Prize in physics. A Penning trap works as an electromagnetic potential well for charged particles. Precision mass measurements are most often performed using the destructive Time-of-Flight Ion Cyclotron Resonance (TOF-ICR) method. However, there are also non-destructive methods [54].

The particles in a trap can be excited to perform an oscillatory motion, where three

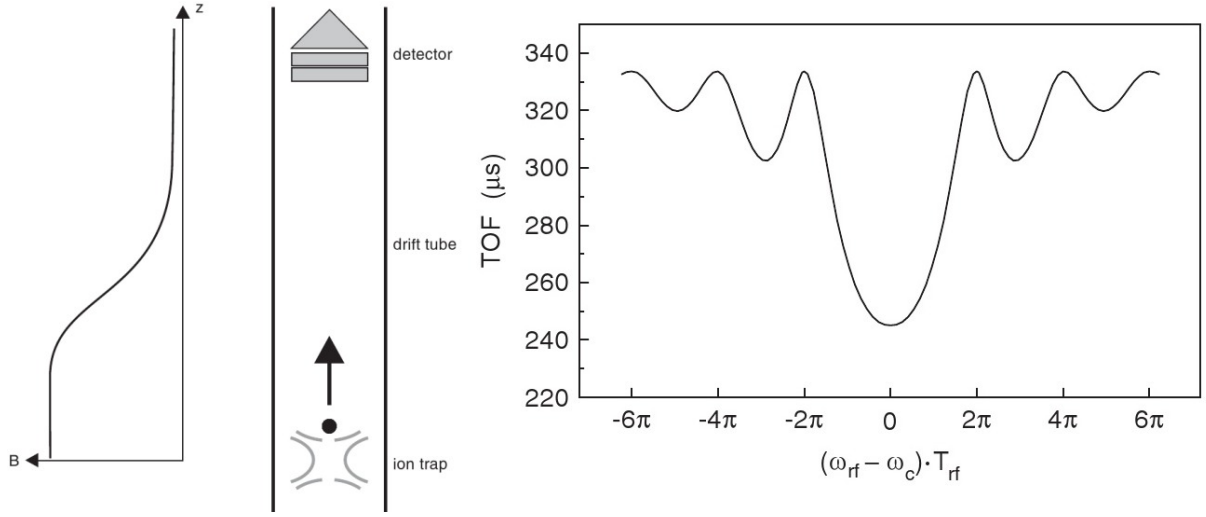


Fig. 2.2: Time-of-flight measurement in a penning trap (left panel) and measured TOF value as a function of excitation frequency (right panel). From Ref. [54].

different oscillation modes appear: axial oscillations, magnetron motion and modified cyclotron motion. These motions can be converted one into another, changing the total energy stored by the system. The eigenfrequency of the cyclotron motion ω_c is determined by the charge-to-mass ratio q/m and the magnetic field B only: $\omega_c = \frac{q}{m}B$. In destructive spectrometry, the particles are released from the trap after excitation and the time-of-flight (TOF) between the trap and the detector is measured, see Fig. 2.2. If the excitation frequency matches the cyclotron eigenfrequency, there is a full conversion of energy between two radial oscillation modes, which means the total energy stored by the system energy is at its maximum and it has the effect that the total kinetic energy of particle is maximized. This leads to a shorter time-of-flight after release from the trap. After TOF measurements the mass-to-charge can be derived from the eigenfrequency [54].

Penning-trap technique has the advantage of extremely high precision. The mass of nuclides can be measured down to a few keV or even below. However, only a single species of nuclides can be investigated at once, which means that the beam of particles has to be purified from any undesirable contamination.

2.2.2. Storage-ring mass spectrometry A storage ring is a facility where charged particles can be stored at a certain (high) energy for extended periods of time.

The revolution frequency of the stored particles can be measured by a detector placed in the ring and the mass-to-charge ratio can be derived from the revolution frequency. The advantage of this method is that the ring has a big acceptance and many various species can be stored at the same time, similar nuclides that only differ in charge state can be stored simultaneously. Signals from all stored particles form a broad spectrum containing species with known and unknown masses. Therefore the calibration and the data evaluation can be done *in situ*, that is, using the same spectrum.

The revolution frequencies f , the mass-to-charge ratios m/q and the velocities v of

stored ions are connected by the following relationship:

$$\frac{\Delta f}{f} = -\frac{1}{\gamma_t^2} \frac{\Delta \frac{m}{q}}{\frac{m}{q}} + \frac{\Delta v}{v} \left(1 - \frac{\gamma^2}{\gamma_t^2}\right), \quad (2.1)$$

where γ is the Lorentz factor for stored particles and γ_t is a non-linear ion-optical parameter of the ring, the so-called transition energy. The momentum compaction factor $\alpha_p = 1/\gamma_t^2$ describes the relative variation of orbit length per relative variation of magnetic rigidity of the particle (see Subsection 3.1.3 and Section 3.2).

The storage ring can be operated in one of two regimes: SMS (Schottky Mass Spectrometry) [55] and IMS (Isochronous Mass Spectrometry) [56]. Both regimes aim to minimize the second term in Eq. (2.1): the SMS assumes that the relative velocity spread ($\Delta v/v$ term) is negligibly small due to cooling, while the IMS exploits the so-called isochronous mode $\gamma = \gamma_t$.

The main cooling method used in the SMS is electron cooling, invented in 1966 by Gersh I. Budker [57]. Electron cooling exploits a constantly renewed flux of mono-energetic electrons, which is used for keeping stored particles at a certain sharp velocity. Due to Coulomb collisions, the longitudinal as well as the transversal momenta of both, electrons and ions, are changing. After short interaction length (in the order of a few meters), the electrons are extracted by a weak toroidal magnetic field, whereas the ions — only slightly disturbed — remain stored and can interact, when coming back, again with new, cold electrons. By means of this ingenious “trick”, the emittance[†] of the ions will be reduced by many orders of magnitude within a short time which amounts — for “hot” fragments — to a couple of ten seconds. As the main result, the ions get the same sharp velocity of the ions with a negligibly small relative velocity spread $\Delta v/v$, and, thus, a simple relation between m/q and revolution frequency is established.

Another cooling method is the stochastic cooling. It was invented by Simon van der Meer, who was awarded with the 1984 Nobel prize for that invention [58]. The main idea is a correction of transversal (betatron) oscillations of stored particles by applying synchronized detector and kicker, the former detects the transversal position offset of an ion and the latter then kicks the ion to the “right” orbit. By means of stochastic cooling the transversal as well as the longitudinal velocity spread can be reduced.

2.2.3. Production and separation of exotic nuclei

In order to investigate radioactive species, the latter have to be produced first and then purified. The production of radioactive species is based on the interaction between the primary beam and target atoms. There are many possible choices for beam and target combinations: the beam can consist of heavy or light particles and can have low or high kinetic energy, the target can also consist of heavy or light particles [59, 60]. There are

[†]emittance shows distribution of beam in phase space; small emittance corresponds to collimated beam in space and momentum

four most often occurring reaction types:

- Projectile fragmentation: a heavy fast beam hits a light-Z target
e.g. ^{209}Bi beam at 600 MeV/u hits ^9Be target producing a large number of fragments with $Z \leq Z_p = 83$ and $N \leq N_p = 126$ [61]
- Fusion: a medium-heavy slow beam hits a heavy-Z target
e.g. ^{70}Zn beam at 5 MeV/u hits ^{208}Pb target thereby producing $Z=112$ element [62]
- Spallation (or target fragmentation): light fast beam hits heavy-Z target
e.g. protons at 1.5 GeV hitting uranium target thus producing hundreds of fragments with $Z \leq Z_t = 92$ and $N \leq N_t = 146$ [63]
- Fission: uranium fast beam hits light-Z target
e.g. ^{238}U beam at energy of 750 MeV/u hits lead target thereby producing neutron-rich fragments in the Zn-Sn region [64]

The production target thickness can be selected based on the reaction type. The target thickness is measured in units of g/cm^2 , which corresponds to the density ρ of material multiplied by the size l of the target: $\rho \left[\frac{\text{g}}{\text{cm}^3} \right] \cdot l[\text{cm}]$.

There are two main techniques for production and separation of a radioactive beam: ISOL (Isotope separation on-line) [65, 66] and in-flight [67, 68], whose main properties are listed in Tab. 2.1. The idea of the ISOL method is to have very thick target (up to a few 100 g/cm^2 or a few ten cm in length) so that accelerated protons (or light-ions) induce many reactions (mainly spallation reaction) until they stop there. Products of reactions have also no initial kinetic energy and therefore have to be extracted from the target. In-flight method supposes thinner target (up to a few g/cm^2 or a few cm in length), where neither projectile nor reaction products, which have high kinetic energy and charge, stick in the target.

Advantages of ISOL method are high production yields (which is the effect of the target thickness) and good beam emittance due to ionization at rest. The disadvantage of ISOL is that due to the target thickness the produced particles stick in the target and they need to be extracted. Various chemical elements have different abilities for being extracted. Furthermore, extracted particles have to be ionized and post-accelerated. On the other hand, in-flight method provides very fast highly-charged particles, whose disadvantage is large beam emittance, which inevitably requires beam cooling, though no post-acceleration is needed.

2.3

Nuclear structure properties derived from mass values

What information about nuclear structure can be extracted from a measured mass value?

Tab. 2.1: Production and separation of radioactive species: ISOL and In-flight techniques

	ISOL	In-flight
Primary beam	protons, light ions	stable ions from proton to U
Primary beam energy	100-1500 MeV/u	from the Coulomb barrier up to a few GeV/u
Target density	up to a few hundred g/cm ²	a few g/cm ²
Target thickness	~ 30 cm	~ 3 cm
Reactions	spallation, fission, fragmentation	fragmentation, fission, fusion
Additional ionization	surface ionization, laser ionization, ionization by electron impact [69]	target backing (Nb foil)
Energy of fragments	a few ten keV (after post-acceleration)	a few hundred MeV/u
Setups	ISOLDE at CERN, Geneva (Switzerland) [70]; ISAC at TRIUMF, Vancouver (Canada) [71]; IGISOL, Jyväskylä (Finland) [72]	GSI, Darmstadt (Germany); GANIL, (France); JINR, Dubna (Russia); MSU, (USA) and RIKEN (Japan)

From the mass value of a single nucleus one can calculate its nuclear binding energy. It is interesting to note, that the highest binding energy per nucleon corresponds not to iron-56, but to nickel-62, although iron-56 is by a factor of 200 more abundant in the solar system than nickel-62. That can be explained as follows: in stars nickel-56 (doubly-magic nucleus) is widely produced, because it has 28 protons and 28 neutrons and thus consist of 14 α -particles. The half-life of ^{56}Ni is 6 days, that means after a supernova explosion all ^{56}Ni decays to ^{56}Co and afterwards to stable ^{56}Fe [73].

Combining two, three or more mass values of neighboring nuclides, one can calculate different quantities, some of which are listed in Tab. 2.2.

The main features of the nuclear structure that can be understood from all these energies are listed below, type of energy that reveals the feature is given in parenthesis.

- The drip-lines (separation energies)

The drip-lines are boundaries of nuclear stability with respect to nucleon emission. The neutron drip-line represents a number of neutrons for a specified element (i.e. specified proton number Z), when the separation energy becomes negative, meaning that every additional neutron is not bound. The analog is the proton drip-line: for a specified number of neutrons N every additional proton is not bound (although it can live for some short as halo-nucleus), when the proton separation energy becomes negative.

Tab. 2.2: Quantities, that can be derived from mass values

for all Z, N	Separation energy	One-nucleon	S_n	$m_{Z,N-1} + m_n - m_{Z,N}$	
			S_p	$m_{Z-1,N} + m_1H - m_{Z,N}$	
		Two-nucleon	S_{2n}	$m_{Z,N-2} + 2m_n - m_{Z,N}$	
			S_{2p}	$m_{Z-2,N} + 2m_1H - m_{Z,N}$	
$Z, N \text{ --- even}$	Pairing-gap energy	3-particle formula	Δ_{n3}	$0.5(m_{Z,N-1} - m_{Z,N} - m(Z, N + 1))$	
			Δ_{p3}	$0.5(m_{Z-1,N} - m_{Z,N} - m_{Z+1,N})$	
		4-particle formula	Δ_{n4}	$0.25(m_{Z,N-2} - 3m_{Z,N-1} + 3m_{Z,N} - m_{Z,N+1})$	
			Δ_{p4}	$0.25(m_{Z-2,N} - 3m_{Z-1,N} + 3m_{Z,N} - m_{Z+1,N})$	
		5-particle formula	Δ_{n5}	$0.125(m_{Z,N-2} - 4m_{Z,N-1} + 6m_{Z,N} - 4m_{Z,N+1} + m_{Z,N+2})$	
			Δ_{p5}	$0.125(m_{Z-2,N} - 4m_{Z-1,N} + 6m_{Z,N} - 4m_{Z+1,N} + m_{Z+2,N})$	
	Shell gap		G_n	$0.5(S_{2n}(Z, N) - S_{2n}(Z, N + 2))$	
			G_p	$0.5(S_{2p}(Z, N) - S_{2p}(Z + 2, N))$	
	Proton-Neutron interaction strength δV_{pn}			$0.25(S_{2n}(Z, N) - S_{2n}(Z - 2, N)) =$ $= 0.25(S_{2p}(Z, N) - S_{2p}(Z, N - 2)) =$ $= 0.25(m_{Z-2,N} - m_{Z,N} - m_{Z-2,N-2} + m_{Z,N-2})$	

One can define one- and two-nucleon drip-lines, the latter is smoother, because on that scale pairing between nucleons of the same type plays an important role; for example, a very neutron-rich nucleus is able to bear one more neutron if it has an odd number of them, but is not able if it has already an even number of neutrons (see in Fig. 2.3).

Up to now, the neutron drip-line is known for only the first eight elements, whereas the proton drip-line is known for many nuclides. The reason is that the neutron drip-line is located much further away from stability than the proton drip-line (see Fig. 2.4). To understand this phenomenon one needs to know, why the drip-lines are present at all. The proton drip-line could be understood in a classical sense that very neutron-deficient nuclei have a shorter distance between protons and Coulomb repulsion overtakes nuclear forces, though this very classical explanation is much oversimplified for a quantum system.

Both drip-lines can also be understood from the perspective of Pauli principle, since protons and neutrons are fermions. As experimental data on shell structure show, neutrons and protons have separate energy levels. It is energetically favorable to fill energy levels of both protons and neutrons equally. However, there is an asymmetry of nuclidic chart toward neutron-rich nuclei, because neutrons do not feel Coulomb repulsion. Roughly speaking it means there is a competition between Coulomb force and proton-neutron symmetry. The neutron drip-line can be explained now as

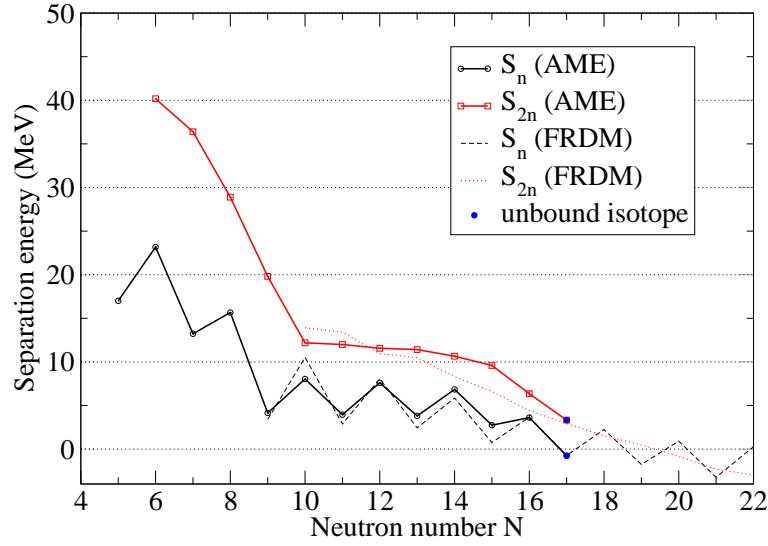


Fig. 2.3: The one- and two-neutron drip-lines location for oxygen isotopes ($Z=8$). Blue points are taken from Ref. [76]

a place where asymmetry between neutrons and protons becomes crucially large.

Very interesting things can happen near the drip-lines because of competing nuclear and Coulomb forces; in Fig. 2.5 potentials for neutrons and protons in a nucleus are described with the Woods-Saxon potential plus an additional potential from the Coulomb force for protons [28]. Protons have a different form of potential barrier, when one sums the Woods-Saxon and the Coulomb potentials, which allows nuclei to exist beyond the proton drip-line (see [74]). On the other hand, neutrons do not have a Coulomb barrier although for a nuclei with non-zero spin a centrifugal barrier can exist, nuclei beyond the neutron drip-line are as a rule very short-lived ($t \leq 10^{-18}$ s) resonances.

- Shell closures (separation energies, shell gap, pairing gap)

It was discovered that nuclei with some certain numbers of neutrons or protons show extra stability. By analogy with magic numbers of electrons in the atom, these numbers are considered as nuclear shell closures. Some measurable properties of nuclei show special features: a drastic change in separation energies (after a shell is filled, it becomes very easy to remove one or two “excess” nucleons off), significant increase in energy of the first 2^+ excited state (the “magic” nuclei are supposed to have a non-deformed spherical shape, which makes vibrational excitations $0^+ \rightarrow 2^+$ [75] energetically less favorable), longer life-time and other properties.

- Deformations (two-nucleon separation energies)

Experimental investigation of deformed nuclei was initiated by Edward Teller and John A. Wheeler in 1930 with search for rotational bands in alpha- and beta-ray spectra. Unfortunately, they didn’t know, that their nucleus of interest, ^{208}Pb , is

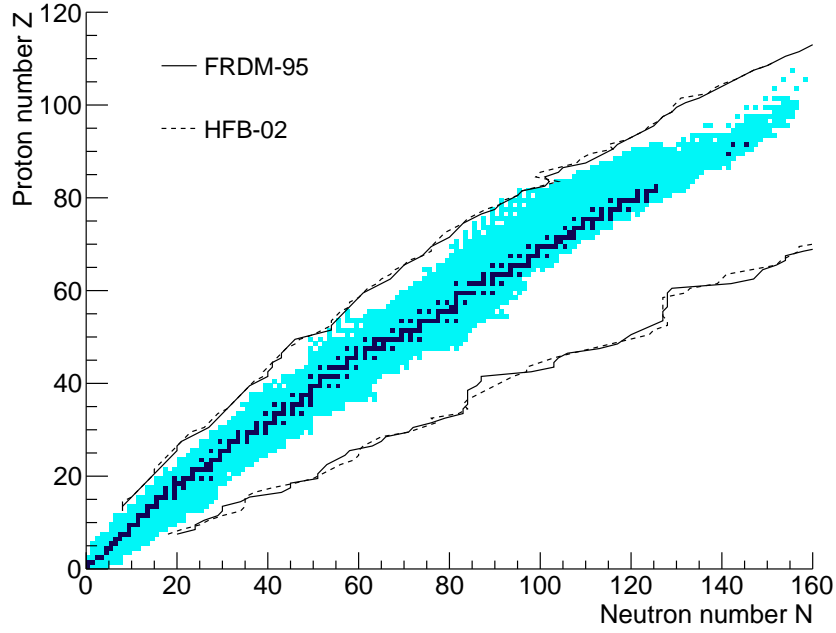


Fig. 2.4: The two-nucleon drip-lines location by predictions of FRDM and HFB mass models. Colored squares correspond to nuclides with measured masses, according to AME-03 table.

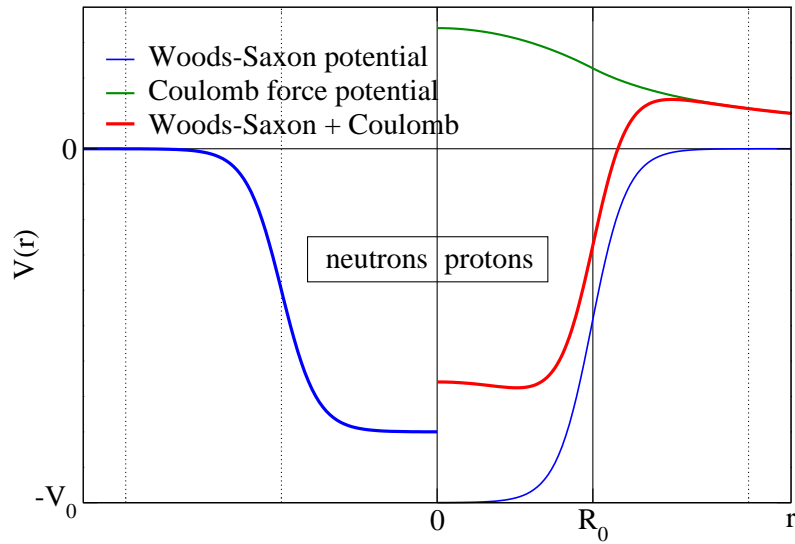


Fig. 2.5: The shell model potentials for neutrons and protons in a heavy nucleus with neutron excess. The nuclear part of the proton potential is deeper due to symmetry energy.

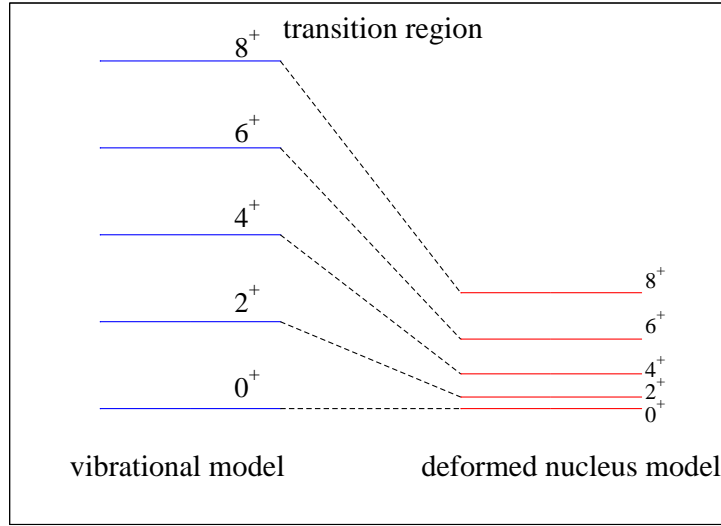


Fig. 2.6: Schematic level schemes of spherical and deformed nuclei. From Ref. [77]

doubly magic and spherical!

The atomic nucleus can be excited by giving energy into its vibrational or rotational motion. The former means multipole surface oscillations, the latter is a collective rotation around an axis different from the symmetry axis. It is commonly supposed that exciting a spherical nucleus the energy can be easier converted into the vibrational motion, while exciting a deformed nucleus causes the energy to be converted into rotation. In Fig. 2.6 one can see level schemes of vibrational states (for spherical nuclei) as harmonic spectrum $E = \hbar\omega(n + 1/2)$ and of deformed nucleus model as $E \sim I(I + 1)$. In nature these pure cases are not exactly realized, but one can observe transition between these limits, for example in the region of stable osmium isotopes [77].

These structures of energy levels can be investigated by spectroscopic studies, usually energy of the first 2^+ state or the ratio $R_{42} = E_{4^+}/E_{2^+}$ can give information about the deformation of the nucleus (see in Fig. 2.7).

2.4

Other applications of experimental mass data

Since the theory of the atomic nucleus is not yet developed well enough in order to precisely predict nuclidic masses, experimental mass data are of high significance for modeling of astrophysical processes. These astrophysical processes proceed in different stellar environments and different sites and are needed to explain the observed element abundances in our Solar system as well as in our Galaxy and beyond it. The main ones are the followings [79]:

- s-process (slow neutron capture process) is introduced to explain the formation of stable nuclides heavier than iron/nickel until bismuth. This process is believed to

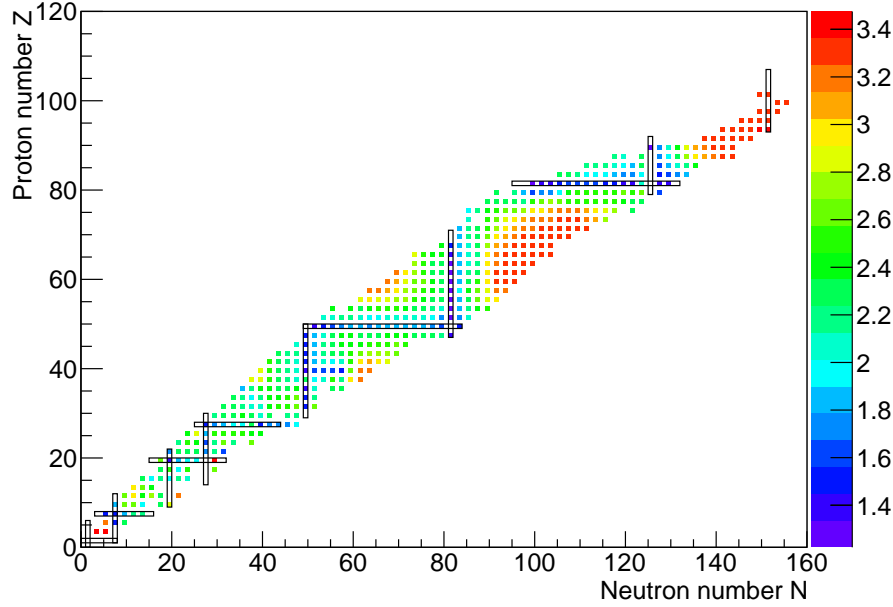


Fig. 2.7: The R_{42} ratio for even-even nuclides is shown. Large numbers correspond to well-deformed nuclei, small values correspond to spherical nuclei with the magic number of protons and/or neutrons. Data are taken from ENSDF tables [78].

occur mainly in AGB stars and on a timescale over thousands of years. About half of element abundance is believed to be produced by s-process.

- r-process (rapid neutron capture process) is a possible explanation of heavy neutron-rich nuclides origin (see Fig. 2.8). It may occur in core-collapse supernovae, where temperature and neutron density are very high. r-process is believed to be responsible for roughly another half of the element abundance. And it is the only process that explains abundance of uranium and thorium.
- rp-process (rapid proton capture process) refers to formation of neutron-deficient nuclides up to tellurium ($Z=52$). This process can occur in accreting binary star systems, in conditions of very high temperature so that protons can overcome Coulomb barrier.
- p-process (proton capture process) explains the formation of the so-called p-nuclei that are certain proton-rich, naturally occurring isotopes of some elements between selenium and mercury ($34 \leq Z \leq 80$), which cannot be produced in either s- or r-process.
- γ -process occurs when nucleus is excited by a captured photon and emits proton (or alpha-particle, or neutron). This process of photodisintegration explains occurrence of some p-nuclei.
- ν p-process is anti-neutrino capture on protons, which can also explain the abundance

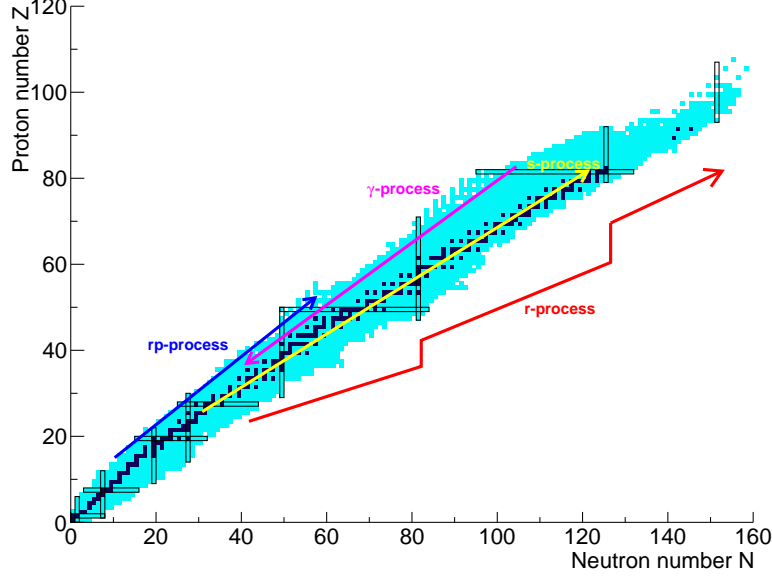


Fig. 2.8: The chart of nuclides with some of nucleosynthesis processes schematically marked.

of some p-nuclei.

Nucleosynthesis pathways depend on parameters of the environment, such as neutron density and the temperature, and on parameters of nuclides themselves. For instance, neutron separation energy S_n can determine the reaction flow in neutron capture processes and proton separation energy S_p — in proton capture processes.

One other important application of mass data is to test the Standard Model and, in particular, to test the unitarity of CKM quark-mixing matrix. Since the weak force is the only interaction that can change the quark flavor and since nucleons are composed of u- and d-quarks, β -decay investigation can be used to determine the $|V_{ud}|$ element of the quark-mixing matrix. By measuring the mass values of parent and daughter nuclei, one can calculate the Q-value of a reaction. Knowing β -decay Q-value, half-life and branching ratio of this decay channel, one can calculate the CKM-matrix coefficient $|V_{ud}|$ and combining it with other particle-data one can test the matrix unitarity [80].

Mass measurements on stable and very long-lived ions provide one interesting application in the neutrino physics, namely, in search of neutrinoless double-beta decay. As a very rare decay mode, double-beta decay ($\beta\beta$) can be studied in order to investigate the nature of neutrino: whether neutrino is Majorana particle $\nu = \bar{\nu}$ or not [81]. The double-beta decay can have one of two possible scenarios: with two neutrino emitted, ($2\nu\beta\beta$), or the neutrinoless double-beta decay, ($0\nu\beta\beta$) [82]. In order to set a limit of the neutrinoless mode, reaction Q-value have to be determined very precisely, less than few keV as it has been determined up to now.

A non-exhaustive list of other applications of high-accuracy mass measurements is e.g.: test of CPT-symmetry, tests of QED, new definition of the kilogram unit and the determination of fundamental constants [54].

Experiment

3.1

Experimental facilities of the GSI Helmholtz Center

The mass measurement experiment discussed within this thesis was performed at the GSI Helmholtzzentrum für Schwerionenforschung in Darmstadt, Germany. In Fig. 3.1 a schematic view of the GSI experimental facilities is shown. A stable heavy-ion beam is produced by an ion source, for this experiment a ^{197}Au beam was used. Then the beam is accelerated up to 11.4 MeV/u in the linear accelerator UNILAC, and then by the synchrotron SIS-18 [83] to an energy of 469.35 MeV/u. Before the fragment separator FRS the beam hits a thin target, initiating the fragmentation reaction. Produced exotic nuclei are focused into the FRS and after the in-flight separation they are injected and stored in the storage ring ESR.

3.1.1. Production target The production target placed after SIS is a relatively thin target as required for the in-flight production and separation. For the present experiment a 1035 mg/cm^2 ^9Be target was used, meaning that the target was made of beryllium (Be) with a density of 1.85 g/cm^3 and a length of 0.56 cm. In addition to beryllium, a 223 mg/cm^2 niobium (Nb) backing on the back side of the target was employed to strip electrons.

When a ^{197}Au beam at an energy of about 500 MeV/u hits a 1 g/cm^2 ^9Be target fragmentation reactions takes place. Based on the EPAX formula [84] production cross-sections of fragments can be estimated as shown in Fig. 3.2. The fragments of this reaction are highly-charged. The charge state distribution of ^{197}Au fragments after the target for a ^{197}Au primary beam at different energies is presented in Fig. 3.3 (left panel). As one can see, at an energy of about 470 MeV/u the charge distribution is as follows: 32% of bare nuclei, 49% of ions with one electron (H-like) and 18% of ions with two electrons (He-like). In order to increase the fraction of bare nuclei, the Nb backing was used. After

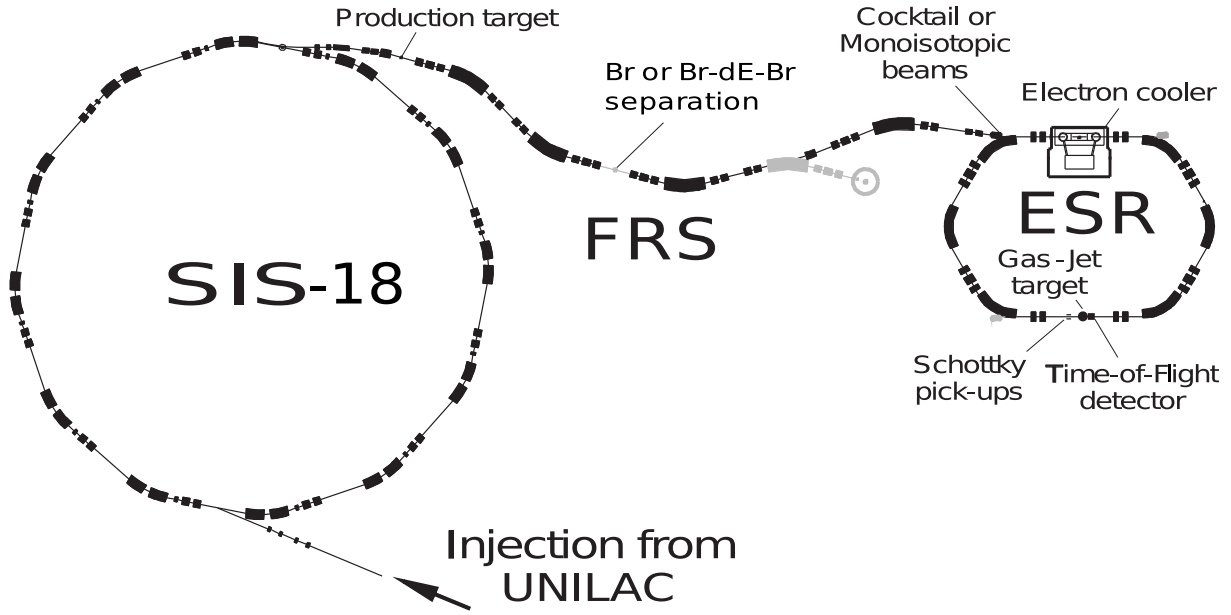


Fig. 3.1: Schematic diagram of some experimental facilities of the GSI Helmholtz Center: the synchrotron SIS-18, the fragment separator FRS and the storage ring ESR. Location of production target, electron cooler, Schottky detector and other facilities is denoted in the figure.

the Nb stripper foil heavy nuclides are delivered as bare nuclei or with up to 3 electrons: the fraction of nuclei with one or more electrons grows with the proton number. Almost 100% of ions with $Z < 30$ are delivered as bare nuclei. The fraction of H-like nuclei surpasses 1% for fragments with $Z \sim 35$, the fraction of He-like and Li-like nuclei comes over 0.1% for $Z \sim 55$ and $Z \sim 78$, respectively (see Fig. 3.3, right panel).

One can also calculate production rates to estimate the minimum cross-section, which could be accessed in the present experiment. The number of produced fragments of a given species per injection can be calculated by

$$N_f = N_b N_t \sigma \varepsilon, \quad (3.1)$$

where N_b is the number of particles in one extraction spill of the primary beam from SIS-18, N_t the number of particles in the target per 1 cm² of target surface, σ the production cross-section in barn* of the fragment of interest and ε the transmission of the ion-optical system between the target and the detector.

The value of N_b for ¹⁹⁷Au beam was approximately 10⁸ particles per spill. N_t can be calculated by the formula

$$N_t = \frac{\rho[g/cm^{-2}] N_A}{m[u]}, \quad (3.2)$$

where ρ is the target thickness, N_A is the Avogadro constant and $m[u]$ is the mass of an atom of the target material in atomic units. For a 1035 mg/cm² ⁹Be target, $N_t =$

*1 barn is 10⁻²⁴ cm²

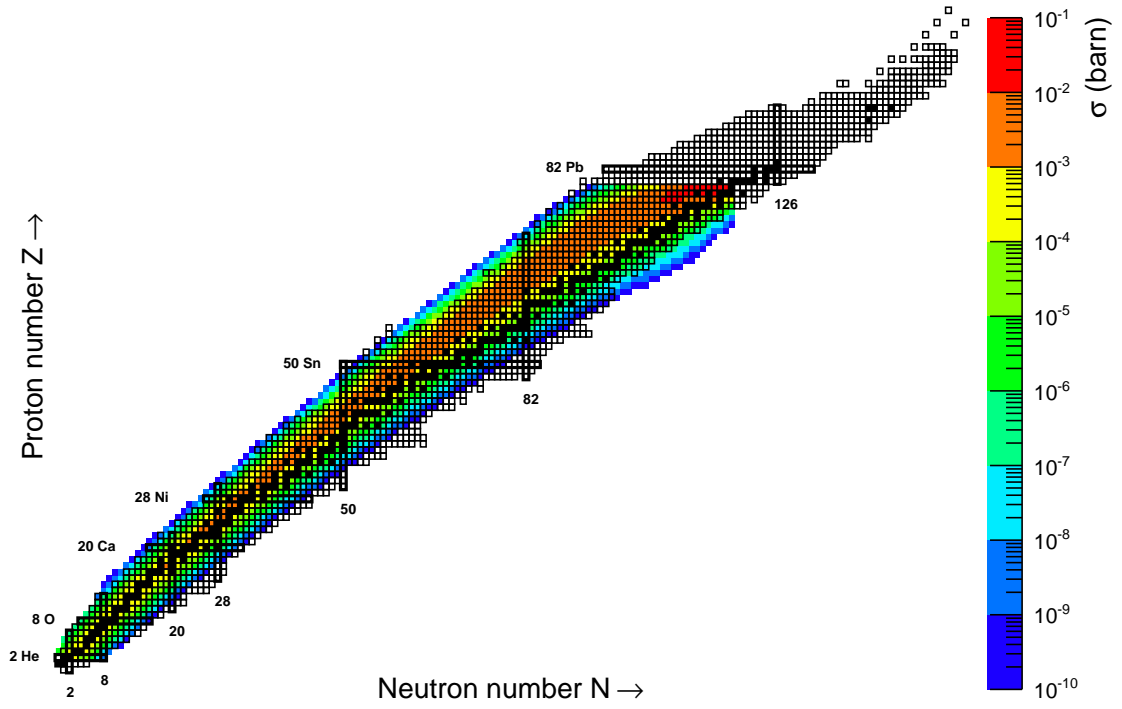


Fig. 3.2: Production cross-sections (in barn) for ^{197}Au projectile-fragments calculated with the EPAX formula [84]. Black-framed squares correspond to nuclides with already measured masses according to [7], full black squares are stable isotopes.

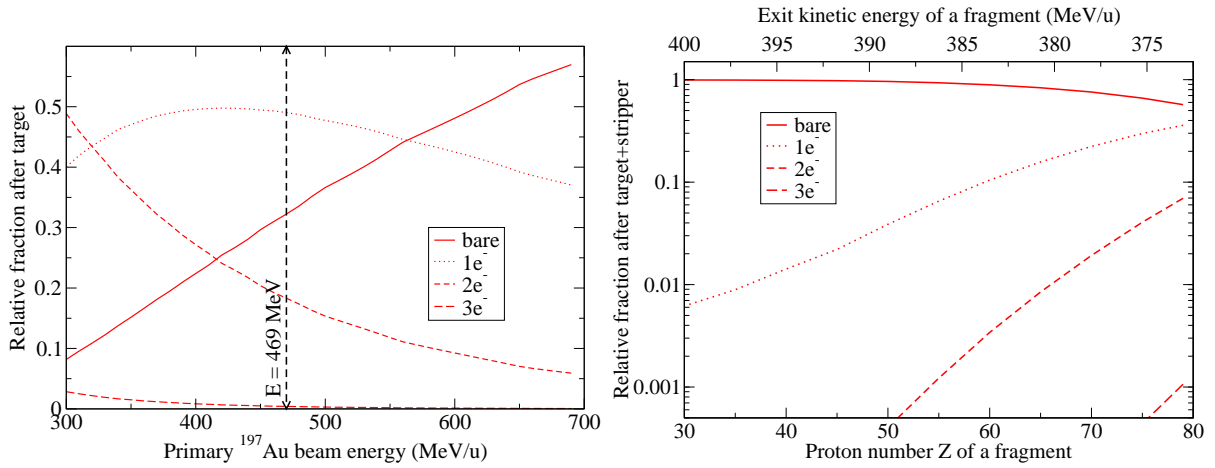


Fig. 3.3: Left panel: charge state distribution of ^{197}Au ions for different energies of the primary beam. Right panel: relative yield of different charge states as a functions of fragment proton number after 1035 mg/cm^2 ^9Be target with 223 mg/cm^2 Nb backing, calculated via LISE++ program [85] and GLOBAL code [86].

$0.069 \cdot 10^{24} [cm^{-2}]$. Transmission efficiency of the FRS-ESR is about 1%.

Having a new injection every 3 minutes and running the experiment for 12 hours one can get 240 injections, which gives us

$$N_f = N_b N_t \sigma \varepsilon \cdot 240. \quad (3.3)$$

If we assume only one particle of a given species $N_f = 1$ in the entire experimental time (which is enough for a mass measurement with the uncertainty of about 100 keV), we can calculate the minimal accessible σ . The minimal production cross-section is $\sigma_{min} = 6 \cdot 10^{-8} \text{ b} = 60 \text{ nb}$.

The calculated σ_{min} allows to measure masses of several nuclides in the neutron-rich region with $67 \leq Z \leq 75$ as well as masses of several nuclides on the neutron-deficient side between $55 \leq Z \leq 70$ for the first time according to Fig. 3.2. However, the present work was focused on the investigation of the neutron-rich nuclides.

3.1.2. The fragment separator FRS The FRS fragment separator is an experimental facility, which consists of dipole and quadrupole magnets (see the scheme in Fig. 3.4).

In the section F2 the degrader can be inserted. FRS allows electromagnetic separation of nuclides of interest via the so-called “ $B\rho - \Delta E - B\rho$ ” procedure [87]. It means the first step of the separation is due to a set value of the magnetic rigidity, that is $B\rho = p/q$, where B is the magnetic field, ρ the effective bending magnet radius, p the momentum and q the charge of particle. It is usually denoted as $B\rho(\text{TA-S2})^\dagger$ and can be tuned by changing the magnetic field of the magnets between the target and the degrader.

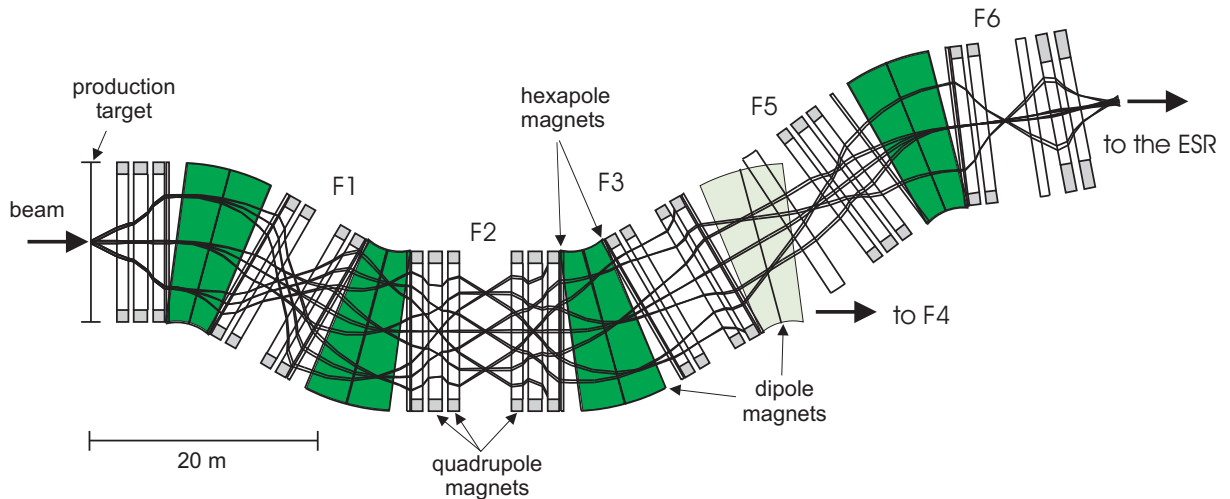


Fig. 3.4: Schematic diagram of the fragment separator magnets

The middle step ΔE means the usage of the energy degrader, which is a piece of matter and provides an additional separation criterion due to an atomic interaction with it, in

[†]TA for target and S2 for F2 section of the FRS

which energy losses are quadratically proportional to the proton number Z ($\sim Z^2$). After the degrader, there are two more magnet sections for the electromagnetic separation. By tuning the magnetic field, one sets $B\rho$ (S2-ESR) on the magnets between the degrader and the storage ring.

At first the FRS is tuned using the primary beam with no target inserted in order to reach maximum possible transmission. In the present experiment we aimed at $^{185}\text{Hf}^{72+}$ fragments and therefore the $B\rho$ settings of FRS-ESR were tuned to this nuclide.

One important point was the elimination of the primary beam particles, since their amount is so large that it overlays all other peaks in the spectrum. After the stripper foil the charge distribution of ^{197}Au ions is: 57% of bare nuclei, 36% of H-like ions, 7% of He-like ions and 0.1% of Li-like ions.

For the mass measurements within this thesis there was no degrader inserted in the FRS in order to have a large diversity of fragments. A $B\rho$ (TA-ESR) of 7.9 Tm was set. The transmission of the FRS $\Delta(B\rho)/(B\rho)$ is of about 1% [88].

3.1.3. The experimental storage ring ESR The ESR experimental storage ring is an experimental facility to store charged particles at a certain energy (see Fig. 3.5).

The storage ring consist of two linear sections and six sections with bending magnets of 60° each. The bending magnet radius is a fixed quantity, but the magnetic field can be varied from 0.08 to 1.6 T. Therefore $B\rho$ can be varied within 0.5 – 10 Tm [47]. Varying the range of $B\rho$ one can store different particles of interest: only ions with $B\rho_{min} \leq mv\gamma/q \leq B\rho_{max}$ can stay in the ring, all other nuclides hit the walls in the bending sections of the ESR.

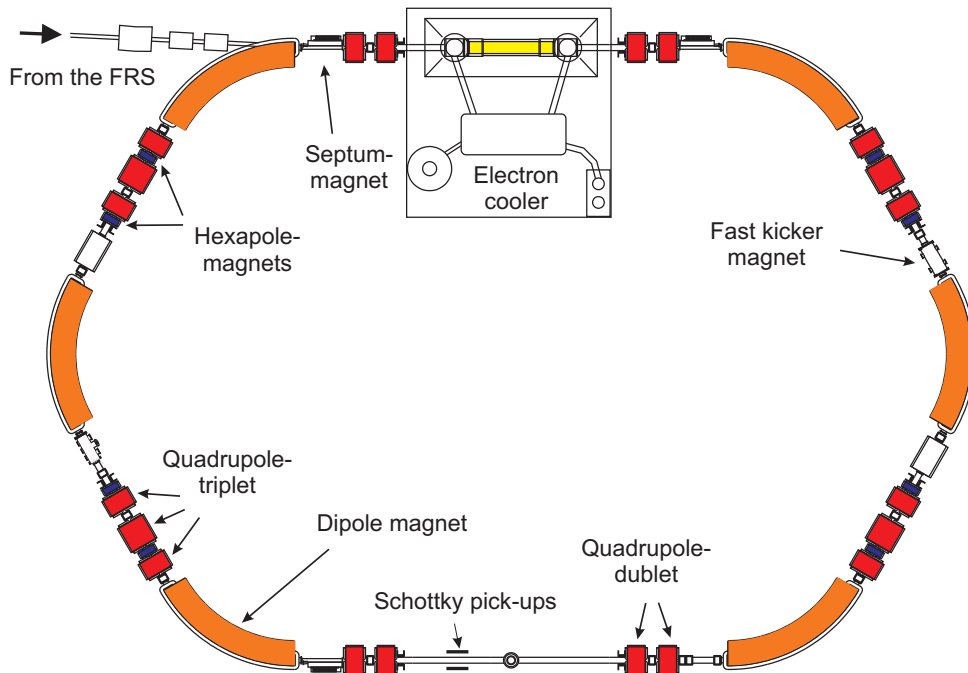


Fig. 3.5: Schematic diagram of the experimental storage ring ESR

The acceptance of the ESR is $\Delta(B\rho)/(B\rho) = \pm 1.5\%$, i.e., $B\rho_{max} - B\rho_{min} = B\rho_{min}$.

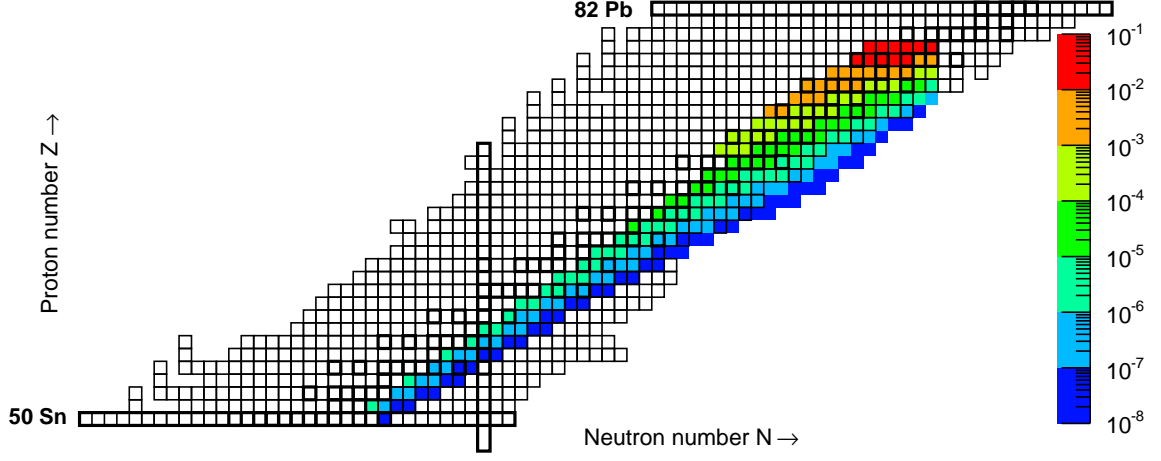


Fig. 3.6: The production cross-sections (in barn) of ^{197}Au fragments, which are expected to be stored under the given experimental settings, i.e. for a range $\frac{m}{q} = 2.52 - 2.62$ and at least in one of the possible charge states.

0.03. As an example, for one of the experimental settings used in the present experiment the ESR acceptance was (7.74–7.98) Tm.

The ESR acceptance is of the same order of magnitude as that of the FRS, i.e. between 1% and 1.5%, though the ESR injection acceptance is only 0.2%. However, during the cooling stored particles change their $B\rho$ and therefore occupy the full ESR acceptance. This fact allows investigation of different species by changing the electron cooler voltage under the same $B\rho$ setting of the FRS-ESR.

As an example of expected nuclides in the storage ring, one can combine calculated production cross-section data and experimental settings to be applied. Since all produced nuclides are bare or have up to 3 electrons, one can choose nuclides fulfilling the condition

$$\left(\frac{m}{q}\right)_{\min} \leq \frac{A}{q} \leq \left(\frac{m}{q}\right)_{\max}, \quad (3.4)$$

where the charge q is Z , $Z - 1$ (for nuclei with $Z > 30$), $Z - 2$ ($Z > 50$) or $Z - 3$ ($Z > 70$). The expected nuclides for $(m/q)_{\min} = 2.52$ and $(m/q)_{\max} = 2.62$ are shown in Fig. 3.6

As mentioned in Section 2.2.2, the revolution frequencies, the mass-to-charge ratios and the velocities of the stored ions in the ESR are connected with the following relationship (for details see Appendix A):

$$\frac{\Delta f}{f} = -\alpha_p \frac{\Delta(m/q)}{(m/q)} + \frac{\Delta v}{v} (1 - \alpha_p \gamma^2), \quad (3.5)$$

where α_p is a non-linear ion-optical parameter of the ring, called momentum compaction factor:

$$\alpha_p = \frac{dC/C}{d(B\rho)/B\rho}, \quad (3.6)$$

where C is the path length of the ions with magnetic rigidity $B\rho$ per one revolution.

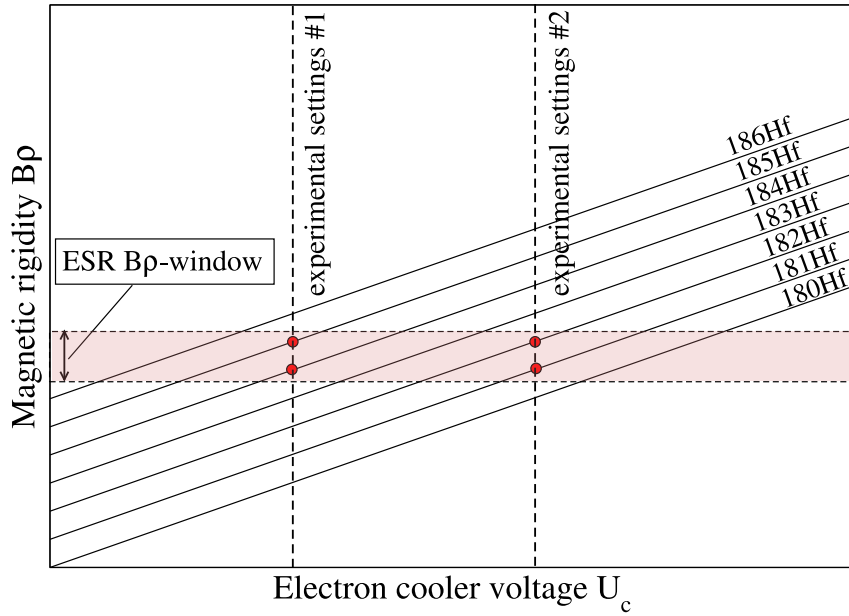


Fig. 3.7: Schematic presentation of the magnetic rigidity as a function of the experimentally set electron cooler voltage U_c (as an example, two arbitrary experimental settings are shown). The pink band represents the ESR $B\rho$ -window. Under fixed other experimental setting, by varying the electron cooler voltage within a few kV, one can store and investigate different isotopes in the ESR.

To apply the SMS, one needs to keep particles at a certain velocity, therefore electron cooling is applied [89]. Varying the electron cooler voltage one changes the velocity of stored particles and therefore the composition of the stored nuclear species, as it is shown in Fig. 3.7. While cooling is applied, all particles stored in the ring have the same velocities, but due to various mass-to-charge ratios they have different trajectories in the magnets and therefore different revolution frequencies. Their path lengths can differ by some tens of centimeters per revolution (the full ring circumference is about 108 m), so that the frequencies differ by only some kHz, while the average revolution frequency is about 2 MHz.

3.2

Schottky Mass Spectrometry (SMS)

SMS is used for mass measurement experiments at GSI since about fifteen years. For a detailed description see Refs. [61, 90, 91]. It is the technique used in the measurements described in this thesis. Practically, the SMS combines two main components: Schottky pick-up detection and electron cooling. Applying electron cooling, one can reach $\Delta v/v \approx 10^{-7}$. Taking this into account, one can consider Eq. (3.5). The typical $\Delta f/f$ value for neighboring ions (with slightly different A/q ratio) is of about 10^{-4} , therefore the second term in the right-hand side of this relationship can be neglected. In the case of isobars, $A/q = \text{const}$, $\Delta f/f$ is of order 10^{-6} , therefore for the α_p calibration ions with different

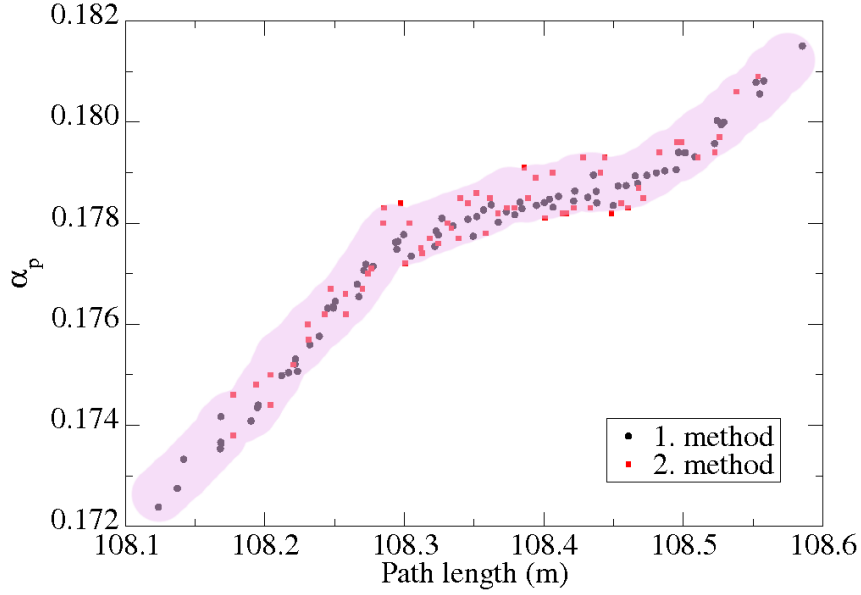


Fig. 3.8: α_p as a function of path length in the ring. Data points on the plot are calculated using Eq. (3.5) in two limiting cases: for a single spectrum with applied electron cooling (shown in black) and for a single nuclear species under different experimental settings (shown in red). The pink band is drawn to highlight places of non-linearity at $C \approx 108.29$ and $C \approx 108.45$. For details see Appendix A.

A/q ratios have to be used.

In Fig. 3.8 α_p is shown as a function of the path length. To calibrate the α_p curve one can take Eq. (3.5) in two limiting cases:

1. calculate α_p from one spectrum, when all ions have approximately the same velocity and $\Delta v/v \rightarrow 0$:

$$\alpha_p = -\frac{\Delta f}{f} \cdot \frac{m/q}{\Delta(m/q)}; \quad (3.7)$$

2. calculate α_p from many spectra but for one species, i.e. scan the revolution frequency as a function of the electron cooler voltage U_c for one specified ion, ($\Delta \frac{m}{q} = 0$):

$$\alpha_p = \frac{1}{\gamma^2} \left(1 - \frac{\Delta f/f}{\Delta v/v} \right). \quad (3.8)$$

For more details about the α_p calibration, see Appendix A.

One notices that the α_p curve is non-linear, which is reflected in the dependence of m/q on f . This is the main complication of the mass evaluation procedure.

The SMS carries its name because of the Schottky noise, which is another name for the shot noise. This phenomenon takes place when the number of particles creating the noise is small enough and independent events can be of significance. First, this type of electronic noise was investigated by Walter Schottky in 1918 in a vacuum tube and therefore named after him. In an electronic circuit this noise occurs due to the quantum nature of the elementary charge. If a current is created by a small number of charged

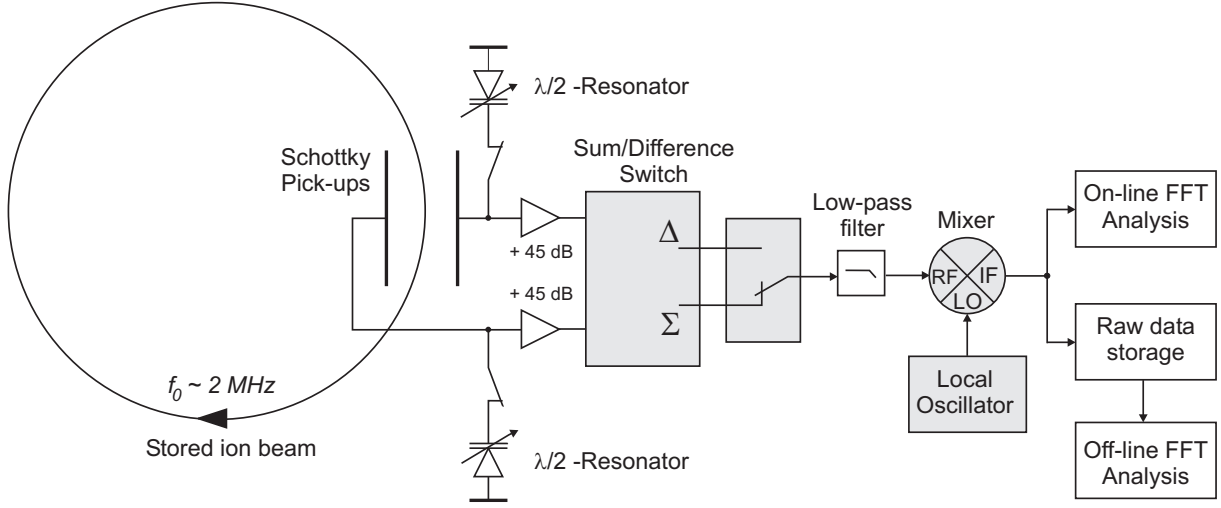


Fig. 3.9: The circuit of the data acquisition system of the Schottky detector. To make use of resonant behavior of the pickups, tunable $\lambda/2$ -resonators can be switched on and adjusted in order to achieve higher signal intensities. Signals from the two horizontal pick-up plates are amplified and summed up. This sum-signal is mixed to the local-oscillator frequency (LO) and splitted for immediate on-line FFT analysis and off-line analysis, for which the signal is digitized and stored with the TCAP system.

particles, then the current intensity apparently fluctuates. These fluctuations are shot noise. In the detector used for SMS, which consists of two pairs of parallel plates, all charged particles that pass by induce image charges on the plates and subsequently a periodic current. The Schottky noise from the pick-up plates consists of signals from the charged ions.

Ions stored in the ring induce a current in the electronic circuits with intervals equal to the period of their revolution, so spectrum of this signal is the main source of information on SMS.

3.3

Data acquisition

The mean revolution frequency of the particles in the ESR is about 2 MHz. To become able to distinguish between isobars, we need to use a higher harmonic of the signal, since higher harmonics require shorter recording time to achieve the same resolution. The 30th-34th harmonic is usually taken, since the Schottky pick-up was designed for them. Signals from both pick-up plates are amplified with low-noise amplifiers and summed up. Before recording the noise from one of these harmonics, one can subtract all frequencies below 60 MHz in order to collect data from only one harmonic. This can be done by mixing the original signal (RF) with a local-oscillator frequency (LO) provided by a frequency synthesizer [92]. The low-frequency intermediate signal (IF) is splitted into two parts: for on-line and for off-line analysis. A schematic view of the electronic circuit is shown in Fig. 3.9. After these transformations of the signal, the ESR storage acceptance

corresponds to about 300 kHz frequency bandwidth. The same data acquisition system was used in previous experiments and is described in Ref. [61, 90, 91, 93, 94].

One can make preliminary on-line analysis mainly to be sure in particle identification and store these data for off-line analysis. The TCAP system was used to collect digitized data for off-line analysis [95].

TCAP data are written in blocks with a sampling rate of 624 kHz. One block is 0.105 s and 131160 bytes, the header of block is 88 bytes, one data point in time domain is 2 bytes, thus every block contains 65536 “time” data points or 32768 “frequency” data points after FFT.

According to the Nyquist relation [96], for a 624 kHz sampling rate the frequency bandwidth is 312 kHz. Taking one block of TCAP data for the digital Fourier transform one has a resolution of 9.54 Hz per channel. In order to have a resolution of 4.77 Hz per channel, 131072 data points (two blocks) were taken.

To perform the discrete Fourier transform a fast Fourier transform (FFT), an algorithm implemented in the FFTW library was used [97, 98].

CHAPTER 4

Data analysis

The analysis of the mass-measurement data consists of the following steps:

1. Off-line production of revolution-frequency spectra by means of FFT
2. Detection of frequency peaks in each FFT-spectrum (in the following *spectrum*)
3. Identification of all peaks in the spectra
4. Selection of reference masses for calibration
5. Finding the dependence of m/q as a function of the revolution frequency, which is needed for the calibration
6. Estimation of unknown mass values using this dependence

All steps are described below in more detail. More information about the software used for the data analysis can be found in [Appendix B](#).

4.1

Schottky frequency spectra

As it was discussed above, the raw data (i.e. Schottky noise) are continuously recorded in the time domain. Since highly charged ions induce mirror charges on the pick-up plates periodically, it is more convenient to work in frequency domain, by using e.g. an FFT.

Since the induced signals are tiny, several hundred thousands of revolutions are necessary to observe a frequency peak corresponding to a single stored ion. FFT-spectrum created from 131072 data points (two data blocks of the data acquisition) corresponds to recording time of 0.21 seconds. We are interested in a more precise measurement of the mass, therefore it is better to average the spectra in order to reduce random noise and thus to increase the signal-to-noise characteristics of the spectra.

Every 50 subsequent spectra are averaged and result in one single spectrum, which corresponds to about 10 seconds of recording time. In Fig. 4.1 an example of a typical single broad-band spectrum is shown. The full frequency span is about 320 kHz. These frequency peaks represent the revolution frequencies of the ions at the 30th harmonic with subtracted LO-frequency. The middle and lower panels of this figure show zooms of the region around 113 kHz. On the lower panel one can see an isobar multiplet with bare tungsten-190, H-like rhenium-190 and He-like osmium-190 ions.

About one hundred sequential spectra are shown on top of each other in a time-resolved 2D-spectrum in Fig. 4.2. The time resolution of this 2D-spectrum is 10 seconds. Note that there are seven injections within 19 minutes, as one can count by the number of segments in each trace (empty gaps between segments correspond to new injections and cooling time). After injection there is often a so-called “cooling tail”: this is a small tail curved to the left/right, which means that the particle was inserted into the ESR with the velocity smaller/larger than the velocity of the cooling electrons and therefore accelerated/decelerated by these electrons. The 2D-spectrum gives a possibility to observe the behavior of particles in the course of time: their appearance, cooling and sometimes decay. It also allows us to distinguish between random noise fluctuations and simply weak traces: the latter appear on the same frequency in a few sequential spectra, though the peaks can have even lower intensity than random fluctuations.

4.2

Correction for magnetic drifts

As one can see in the upper panel of Fig. 4.3, the frequencies of the ions undergo a drift in time. This happens because of fluctuations of the magnetic field of the ESR magnets. One can correct for these drifts. One trace in the spectrum is chosen as a reference for the correction. This trace should be strong enough but it must have no “cooling tails” at the beginning of the injection. One projects this trace on the frequency axis and finds its centroid. The frequency centroid is used as the reference frequency. Afterwards for each spectrum of the time-resolved 2D-spectrum the correction is given in frequency-bins (channels) as the difference between the reference frequency and the local maxima. Then, frame by frame the corrections are applied and every 1D-spectrum in the 2D-spectrum is shifted to the left or to the right by an integer number of bins (see Fig. 4.3, lower panel).

4.3

Peak finding procedure

The software for the automatic peak detection was developed by means of the TSpectrum class of the ROOT libraries [98]. The procedure of the automatic peak detection consists firstly of the detection of peaks in each single 1D-spectrum. A very low threshold is

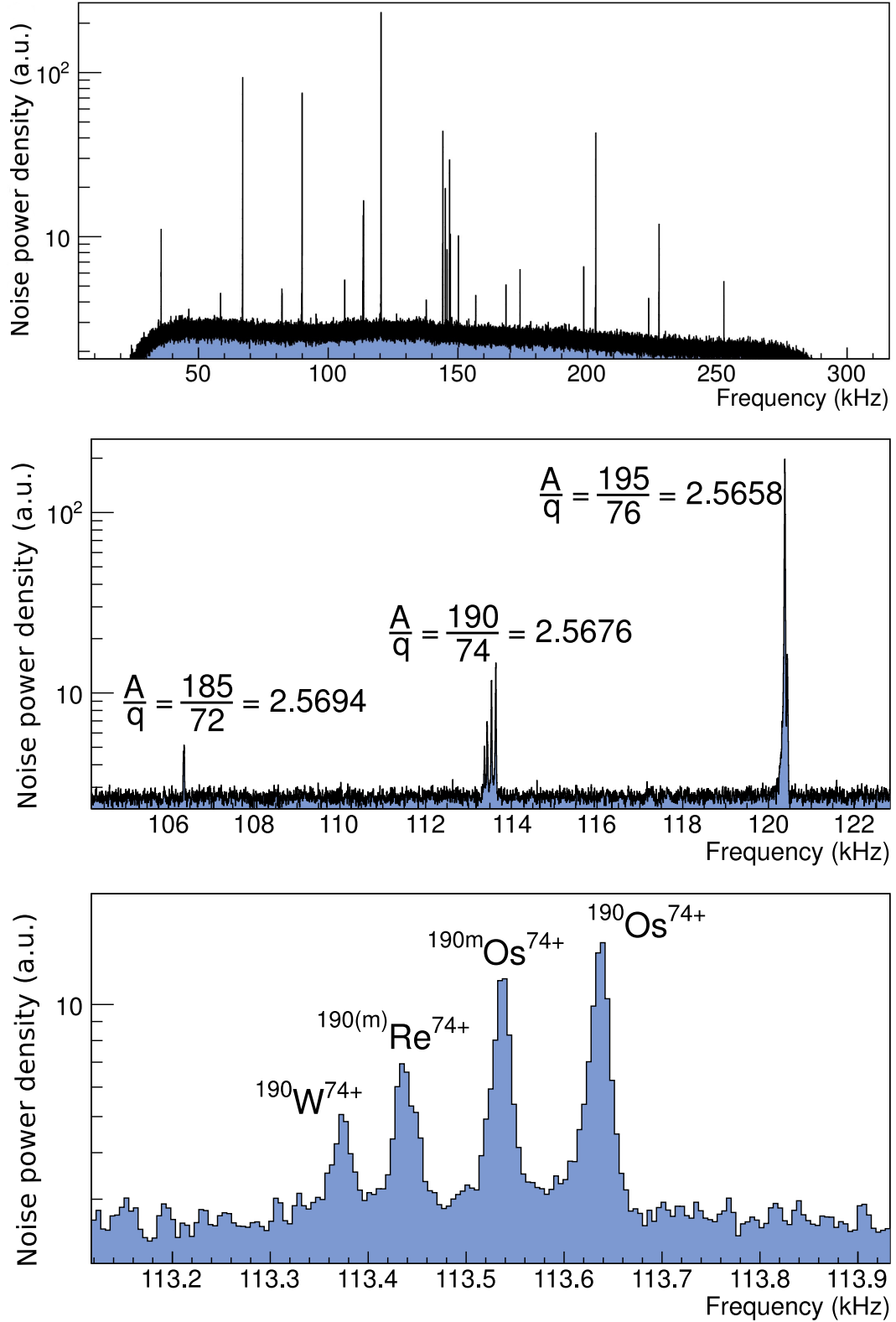


Fig. 4.1: An example of a single spectrum: broad-band spectrum (top) and two zooms (middle, bottom). This spectrum corresponds to about 100 s of recording time (about 200 million revolutions in the ring). On the first zoom there are three isobar groups and on the second zoom there is an isobar with $A = 190$ and $q = 74^+$.

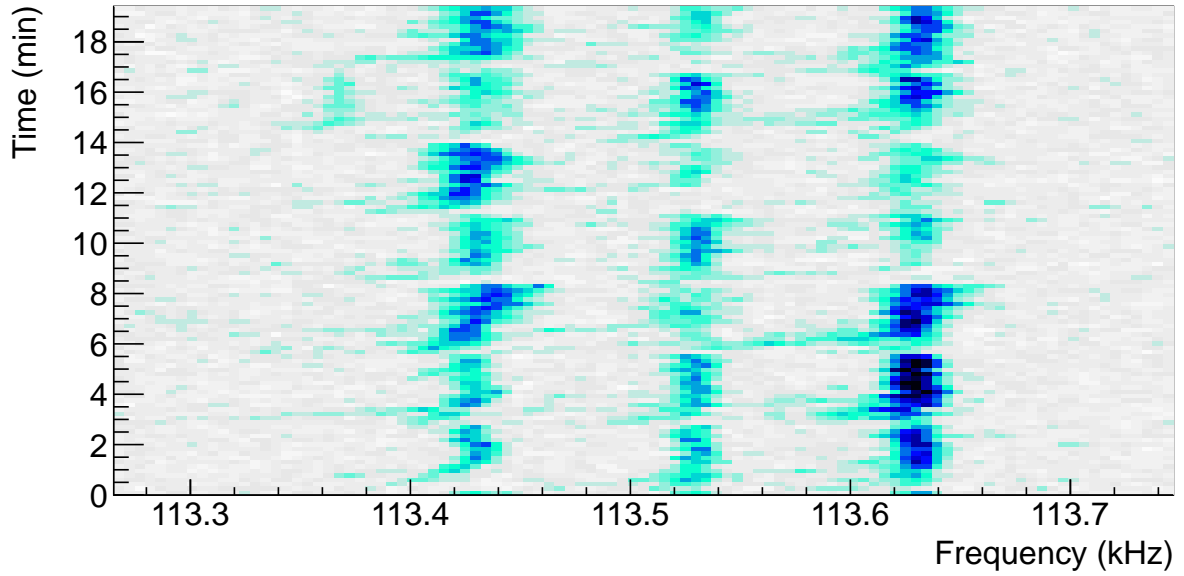


Fig. 4.2: An example of the time-resolved 2D-spectrum, which corresponds to 19 minutes of recording time. Dark colors corresponds to the higher Schottky noise power density in arbitrary units. The four frequencies correspond to the four different stored species with given m/q -ratios. One can count the number of injections by the empty gaps and subsequent “cooling tails”: there are seven injections in this figure.

necessary to detect all weak peaks, as it is shown in Fig. 4.4, upper panel. In order to find the centroid and its uncertainty, one fits a Gaussian function to every detected peak (see Fig. 4.4, lower panel).

The low threshold leads to the detection of noise fluctuations, which do not correspond to real particles. Therefore the automatic noise reduction procedure is implemented. First, one counts all detected peaks on each frequency channel of the 2D-spectrum. The frequency channels that correspond to ions have bigger number of counts than the channels on which only random fluctuations were detected, as it is represented in Fig. 4.5. The frequencies of the ions are selected; it can be done partly automatically, partly only manually, in the case of weak and short traces that have not enough counts to be automatically detected. This unit is called the noise reduction routine, which consists of the following steps:

- Delete points that do not correspond to any real particle;
- Leave only one point that corresponds to an ion in every single spectrum (very often one peak can be detected twice);
- Delete points with a wrong fit.

In the lower panel of Fig. 4.5 one can see an example of a 2D-spectrum with all detected points marked with black dots with horizontal error bars, which come from a Gaussian fitting. On the upper panel of this figure there is a count plot that shows the sums of the points detected in every frequency bin of the lower histogram.

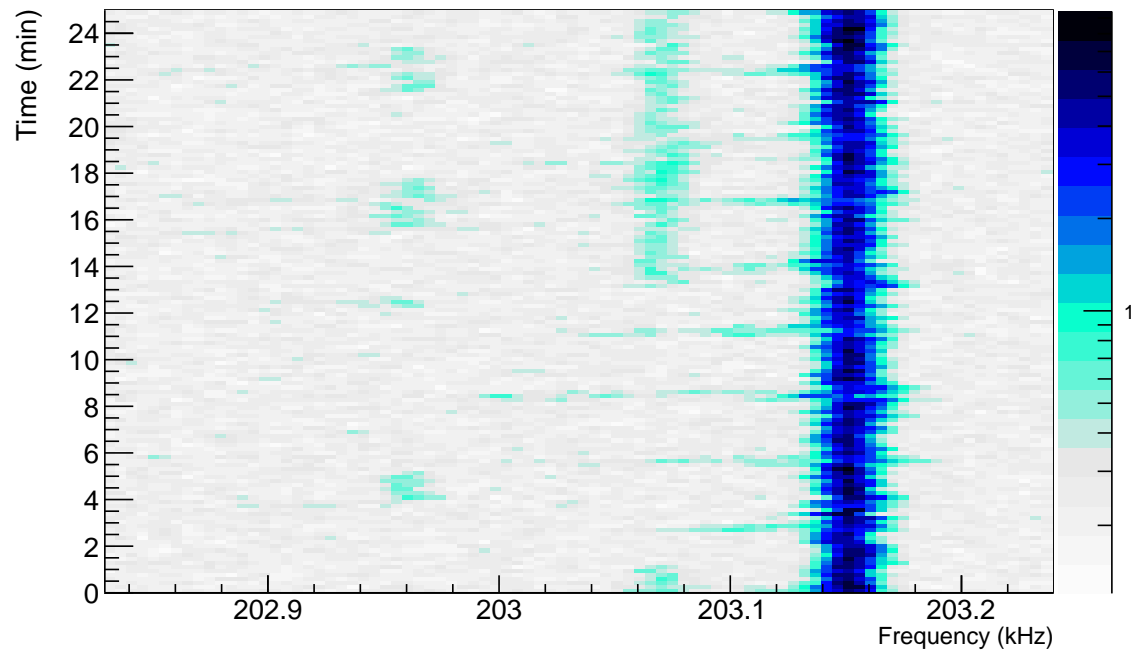
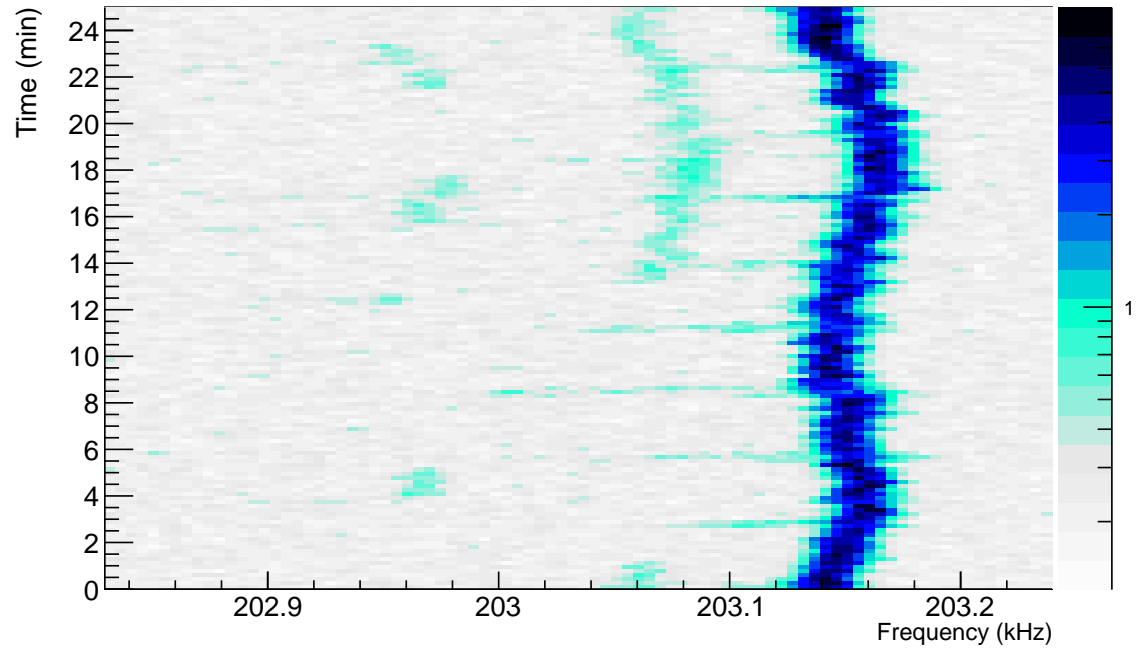


Fig. 4.3: The time-resolved 2D-spectrum before and after the drift correction procedure was applied (for details see text). Every single spectrum is shifted to the left or to the right by some integer number of bins.

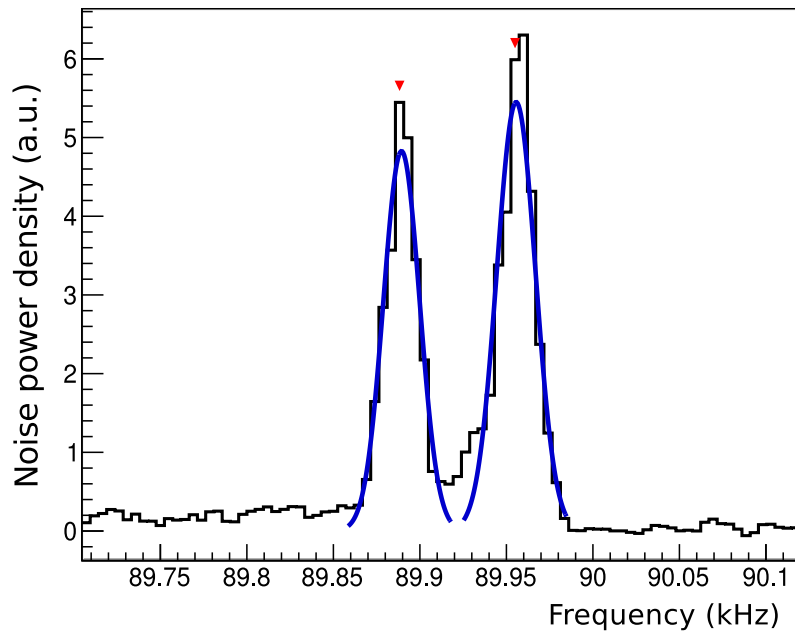
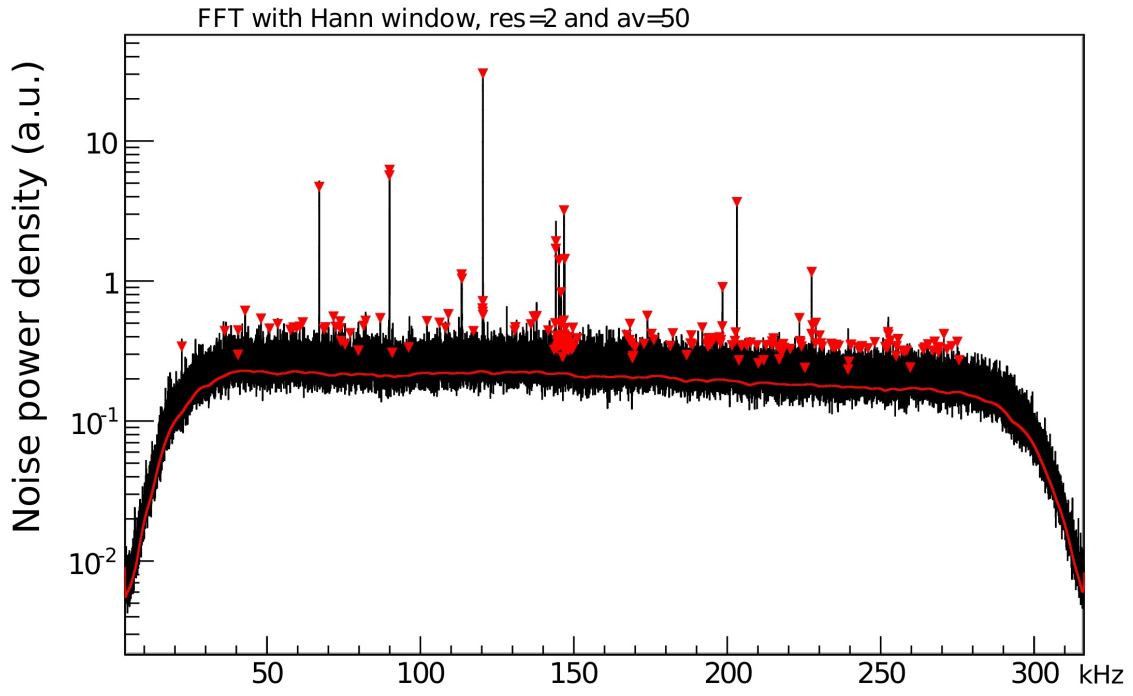


Fig. 4.4: Peak detection in a spectrum. Upper panel: red line is a baseline to subtract. Lower panel: Gaussian fit of detected peaks after subtracting the baseline.

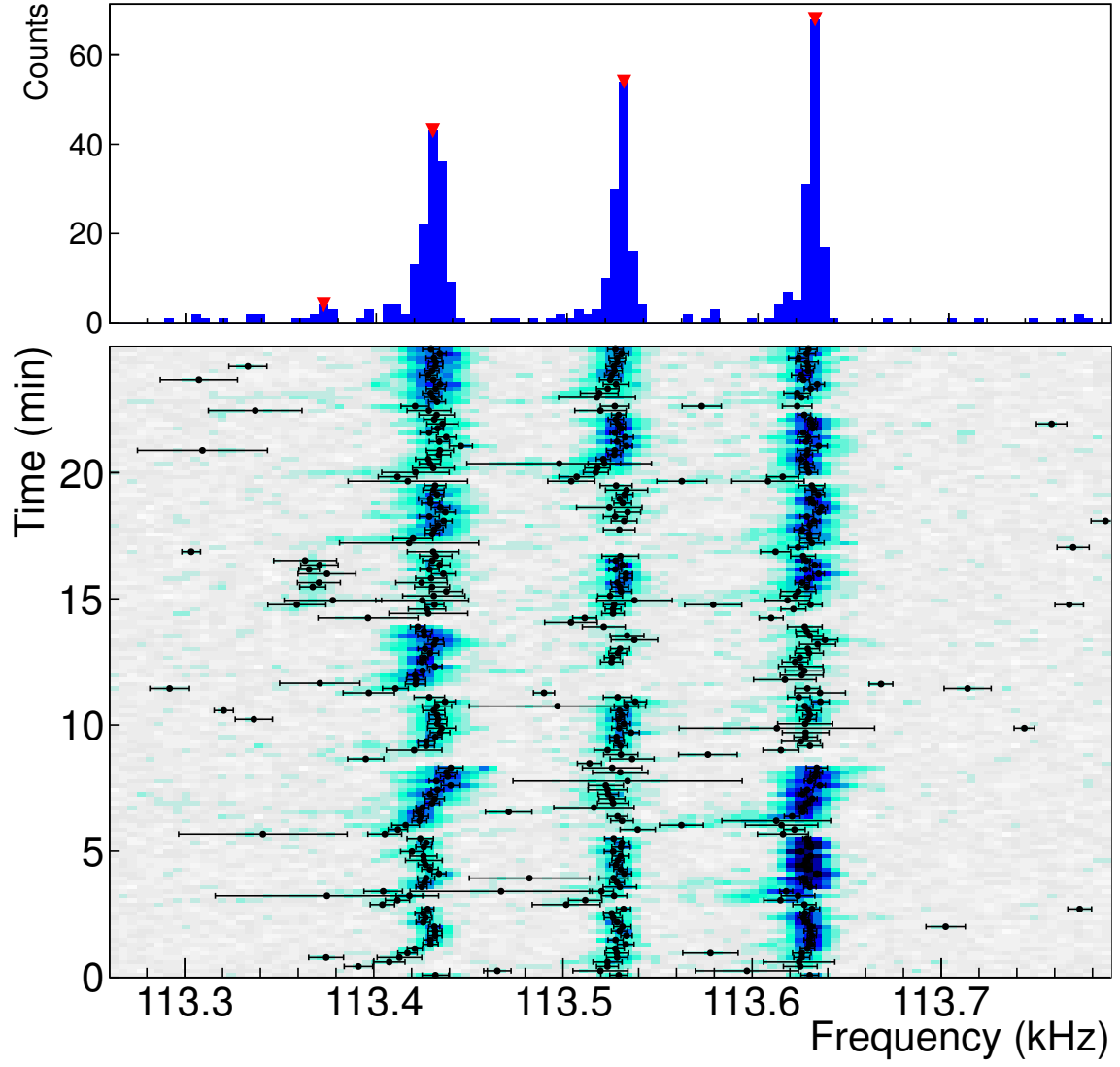


Fig. 4.5: Lower panel: the black points with error bars correspond to Gaussian fit of detected peaks. The task is to delete events that do not correspond to ions but just to random noise fluctuations. Upper panel: number of detected events bin by bin. Peaks marked with red triangles are those, which were found with an automatic peak detection algorithm.

After the noise reduction we have the available information about the particles in the storage ring: their revolution frequencies. Now one has to identify these particles.

4.4

Isotope identification

According to the relationship between the revolution frequencies and the mass-to-charge ratios for the SMS

$$\frac{\Delta f}{f} = -\alpha_p \frac{\Delta \frac{m}{q}}{\frac{m}{q}}, \quad (4.1)$$

one can identify the peaks in the spectra. The differences between the frequencies provide an unique *fingerprint*, which is used for identification.

Lines in the spectra are located as follows: the distances between isobars (ions with the same A/q ratios) are in the order of 10–100 Hz. The distances between the neighboring traces of particles with different A/q are in the order of tens of kHz. Since only bare, H-, He- and Li-like ions can be stored under applied experimental settings, isobar groups usually consist of two or three frequency lines or maybe more due to isomers (nuclear long-lived isomers of an isobar can also be present, which are seen as individual lines). Sometimes two different ions have very similar m/q -ratios and thus their resolution in the spectrum is not feasible, which causes that the spectral line cannot be unambiguously identified.

In our case, the primary $^{197}\text{Au}^{76+}$ beam ions were stored under several experimental settings. The $^{197}\text{Au}^{76+}$ spectral peak is very broad, because it cannot be cooled completely within a given timeframe due to its huge intensity. Therefore it is very easy to recognize the primary beam peak and use it as the starting point of the identification. The experimental settings were changed in small steps, therefore m/q ranges that are available under different settings overlap sufficiently to allow for a continuous identification of all available data.

In Fig. 4.6 the identification under one of the experimental settings is shown. One can see that many nuclides appear in two charge states in the same spectrum, for example $^{190}\text{Os}^{74+}$ and $^{190}\text{Os}^{75+}$ or $^{195}\text{Ir}^{76+}$ and $^{195}\text{Ir}^{77+}$.

4.5

Reference masses

After the identification, one has to specify the references for the further mass evaluation. They must fulfill some criteria:

- Reference isotopes must have an accurately known mass, which was measured more than once by direct measurements. Only isotopes with mass uncertainties of below 15 keV were considered.

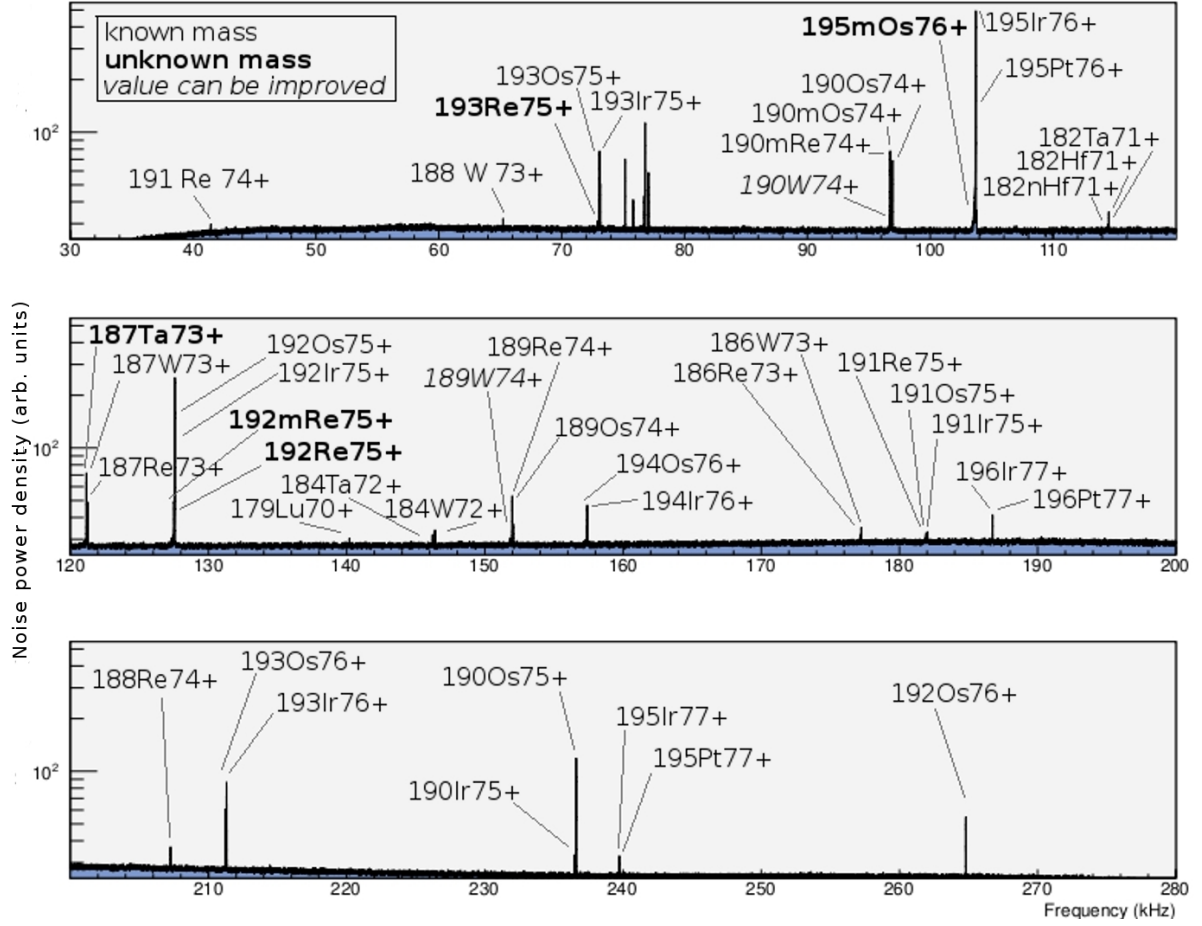


Fig. 4.6: An example of the identification of frequencies in a broad-band spectrum. This spectrum was acquired under experimental settings with the electron cooler voltage $U_c = 209$ kV. Nuclides written in bold face are measured for the first time, and these written in italics have uncertainties larger than 100 keV.

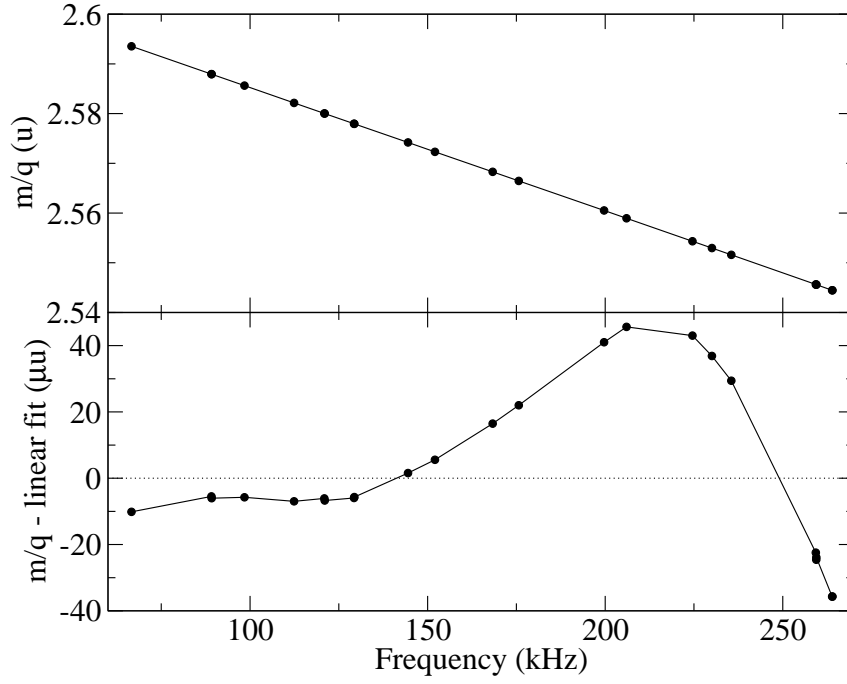


Fig. 4.7: The mass-to-charge ratio as a function of the revolution frequency. Upper panel: the general view, lower panel: same data with subtracted linear fit.

- All traces in the spectra that correspond to a reference nuclide must be well separated from the neighbors and be disambiguously identified.

Practically that means that about 50% of the identified nuclides are references. The selected reference nuclides with their tabulated masses, taken from AME-03 [7], are given in Tab. 5.1.

4.6

Mass evaluation

The goal of the mass evaluation is to describe the mass-to-charge ratio m/q as a function of the revolution frequency f and to evaluate unknown mass values of given frequencies using this function.

In Fig. 4.7 it is shown that, as a rough approximation, the m/q ratio depends linearly on the frequency. After subtracting the linear fit the non-linearity becomes obvious, therefore the $\frac{m}{q}(f)$ dependence requires more complicated fitting procedure.

In general, after choosing the references for the calibration of the $\frac{m}{q}(f)$ function, one can estimate the mass-to-charge value between two references (interpolation) as well as outside of the references (extrapolation). It is more reliable to use only interpolations, since the $\frac{m}{q}(f)$ dependence is strongly non-linear (see Fig. 4.7).

4.6.1. The correlation matrix method (CMM) The dependence of the m/q ratio on the frequency f can be found by means of polynomial fitting. The correlation matrix method (CMM), which is based on the polynomial fitting, was used in previous mass measurements at GSI [61, 91].

Since the various experimental settings were applied, the spectra obtained under different conditions have to be analyzed separately. However, most of the ions appear in many spectra recorded under various experimental settings. Therefore, all spectra can be treated together, in order to take correlations between different fits into account. The origin of these correlations is the very fact that same nuclides exist in many spectra.

For calibration a polynomial function can be assumed. By applying the fitting procedure to every spectrum separately, one minimizes the χ^2 for each polynomial. Since the fit polynomial does not pass exactly through data points, there are some deviations $\Delta_i = y_i - y_i^{fit}$. The χ^2 of the fit is:

$$\chi^2 = \sum_i \frac{\Delta_i^2}{\sigma_i^2}, \quad (4.2)$$

where σ_i are the standard deviations of data points. In general, the fitting procedure finds polynomial coefficients that give the minimal χ^2 .

However, in the case of correlated spectra all fitting polynomials can be treated as a system with a joint χ^2

$$\chi_{joint}^2 = \sum \chi_s^2, \quad (4.3)$$

where χ_s^2 are the χ^2 of single polynomials, which are *not* independent of each other. By minimizing the χ_{joint}^2 one finds fitting polynomials for each spectrum. However, these polynomials cannot be considered as best fits for the data points in a given spectrum, although all together they give the best fit of the whole dataset.

For each spectrum one can assume the P -degree polynomial:

$$\frac{m}{q} - \sum_{p=0}^P a_p(f)^p = l \pm \Delta, \quad (4.4)$$

where m, q, f, l and Δ (mass, charge, frequency, deviation of real m/q from the polynomial value and an uncertainty that will be defined later) have three indices σ, η, ν :

- $\sigma = 0, \dots, S-1$ corresponds to the spectrum index, where S is the number of spectra;
- $\eta = 0, \dots, I-1$ is an index counting different nuclides (Z, A) in spectra (different charge states of the same nucleus correspond to the same index η), where I is the total number of all nuclides in all spectra;
- $\nu = 0, 1, 2$ is a number of occurrences of a given nuclide in a given spectrum (can be 2 or 3 in case the nuclide occurs in this spectrum in different charge states q).

Explicit form of (4.4) reads

$$\frac{m_{\sigma\eta\nu}}{q_{\sigma\eta\nu}} - \sum_{p=0}^P a_{\sigma p} (f_{\sigma\eta\nu})^p = l_{\sigma\eta\nu} \pm \Delta_{\sigma\eta\nu}. \quad (4.5)$$

The deviations l should be normally distributed around zero.

From Gaussian fitting (generated in the peak-finding step) one obtains the uncertainty of the frequency centroid and transforms it in the following way:

$$\Delta_{\sigma\eta\nu} = \frac{d \sum_p a_{\sigma p} (f_{\sigma\eta\nu})^p}{df_{\sigma\eta\nu}} \sigma_{f_{\sigma\eta\nu}}, \quad (4.6)$$

where $\sigma_{f_{\sigma\eta\nu}}$ are uncertainties from Gaussian fittings.

In order to increase the number of correlations within the dataset one can transform all masses to the same charge state, e.g. to the bare ones, by subtracting electron masses and the corresponding electron binding energies, which are well-known [5, 6]:

$$m_{\sigma\eta\nu} = m_{\eta} + E_{\sigma\eta\nu}, \quad (4.7)$$

$$E_{\sigma\eta\nu} = m_e \cdot (Z_{\eta} - q_{\sigma\eta\nu}) - BE(Z_{\eta}, Z_{\eta} - q_{\sigma\eta\nu}), \quad (4.8)$$

where m_e is the electron mass and $BE(Z, Z - q)$ is the electron binding energy for a nucleus with Z protons and $(Z - q)$ electrons.

Due to correlations with other references in all spectra, reference masses may have some deviations from their table values (AME-03 [7])

$$m_r - m_r^c = l_r \pm \Delta m_r^c, \quad (4.9)$$

where m_r are masses of nuclides used as references ($r = 0, \dots, R \in I$, where R is the total number of the references), m_r^c are table values for the reference masses and Δm_r^c are the uncertainties of these reference masses.

The correlations between the polynomials can be taken into account by applying the maximum likelihood method [97]; one writes joint probability density function (or likelihood function) L , which consists of the calibration likelihood function L_c and of the experimental likelihood function L_{exp} :

$$L = L_c \cdot L_{exp} = \prod_r f(l_r, \Delta m_r^c) \cdot \prod_{\sigma\eta\nu} f(l_{\sigma\eta\nu}, \Delta_{\sigma\eta\nu}), \quad (4.10)$$

where $f(l, \sigma)$ is a Gaussian distribution

$$f(l, \sigma) = \frac{1}{\sqrt{2\pi}\sigma} \exp\left(-\frac{l^2}{2\sigma^2}\right). \quad (4.11)$$

In order to find the maximum of L , one solves the following equations:

$$\frac{\partial \ln L}{\partial a_{\sigma p}} = 0, \quad (4.12)$$

$$\frac{\partial \ln L}{\partial m_\eta} = 0. \quad (4.13)$$

The solving procedure of these equations is described in detail in Appendix C. While solving the equations the $I \times I$ matrix is created, which contains information about all ions in all spectra, therefore this method is called the correlation matrix method.

The statistical error can be estimated using diagonal elements of the correlation matrix (see Appendix C). The systematic error can be estimated by “turning-off” one by one all reference masses as if they were unknown and by solving the equations again; afterwards one applies the following formula:

$$\sum_{\eta=r=0}^R \frac{(m_r - m_r^c)^2}{(\Delta m_r^c)^2 + (\sigma_\eta^{st})^2 + (\sigma^{sys})^2} = R. \quad (4.14)$$

One varies σ^{sys} until the sum is equal to the number of references.

The main disadvantage is that the $\frac{m}{q}(f)$ dependence is not well-described by a quadratic polynomial ($P = 2$). For polynomials of higher degree there are not enough points in single spectra or, in other words, too much freedom to draw the polynomial, which leads to huge uncertainties and failures to converge the correlation matrix.

In order to be able to use higher than second degree polynomials, one should have many well-overlapping spectra with a relatively big number of points in each of them.

In the present case there were only ten different experimental settings applied, under each of them about 200 ten-second-spectra were recorded. In order to have as much points as possible in the spectrum, all data from one experimental setting were collected and averaged. Therefore only ten different overlapping spectra were created, with 13–23 points (overall) in every spectrum. This is not enough for fitting a polynomial function of degree higher than two; for the second degree polynomials the χ^2/DoF^* is between 50 and 100, which is too high to claim that the fit describes the data well (see Fig. 4.8).

One should also mention, that the correlation matrix method can be applied without averaging as well. In that case every single spectrum can be described very well by a quadratic polynomial with $\chi^2/DoF = 0.1 - 1$ due to the higher uncertainties of data points, but in that case extrapolations are necessary, since single spectra may contain small number of points, which is not sufficient for fitting. The overall result is dramatically worse than in the case with averaging, if one judges by the estimated systematic errors.

* $\chi_{red}^2 = \chi^2/DoF$ is the reduced chi-squared statistic, which is simply the chi-squared divided by the number of degrees of freedom. The number of degrees of freedom can be estimated as the number of data points minus the number of parameters of the fitting function, see Ref. [99].

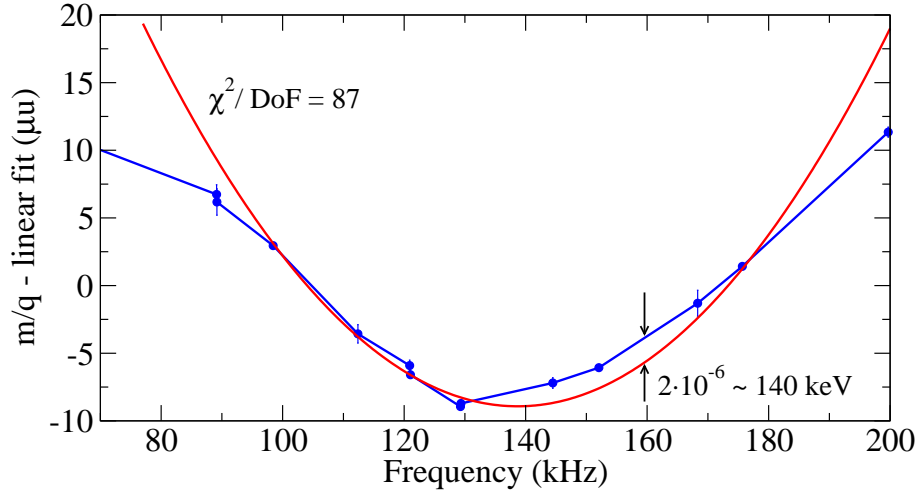


Fig. 4.8: The mass-to-charge ratio as a function of the revolution frequency with the subtracted linear fit in the range 77-200 kHz. The spline is shown in blue and the quadratic fit is shown in red.

4.6.2. Spline method Another method for mass evaluation is a newly implemented spline method. Instead of fitting polynomials to the $\frac{m}{q}(f)$ dependence, one can directly connect all reference points with straight lines, which is named *linear spline* [97].

From the Gaussian fits one obtains centroids and their uncertainties df (the peak-finding step). One can convert these uncertainties to the m/q uncertainties $d(m/q)$. For this purpose the linear fit for the dependence of m/q on f is found:

$$\frac{m}{q} = a_0 + a_1 f. \quad (4.15)$$

Since non-linearities in the $m/q(f)$ are in the order of 10^{-5} u (see Fig. 4.7); therefore the coefficient a_1 can be simply taken to transform df to $d(m/q)$:

$$d\left(\frac{m}{q}\right) = a_1 \cdot df. \quad (4.16)$$

The comparison between linear spline and quadratic polynomial is shown in Fig. 4.8; one can see that the difference between the data points and the polynomial is inadmissibly huge for the quadratic fit. The χ^2 value indicates that the fit hardly describes the data.

An underlying idea of the spline method is simple: in order to evaluate unknown masses one needs to take a value of the spline at required frequency. Because of the multiple spectra with the same experimental settings, one needs to average data at some stage. There are two possible methods:

1. average frequencies for each nuclide and then create a spline and evaluate unknown masses
2. create a spline for each single spectrum, evaluate unknown mass values and after-

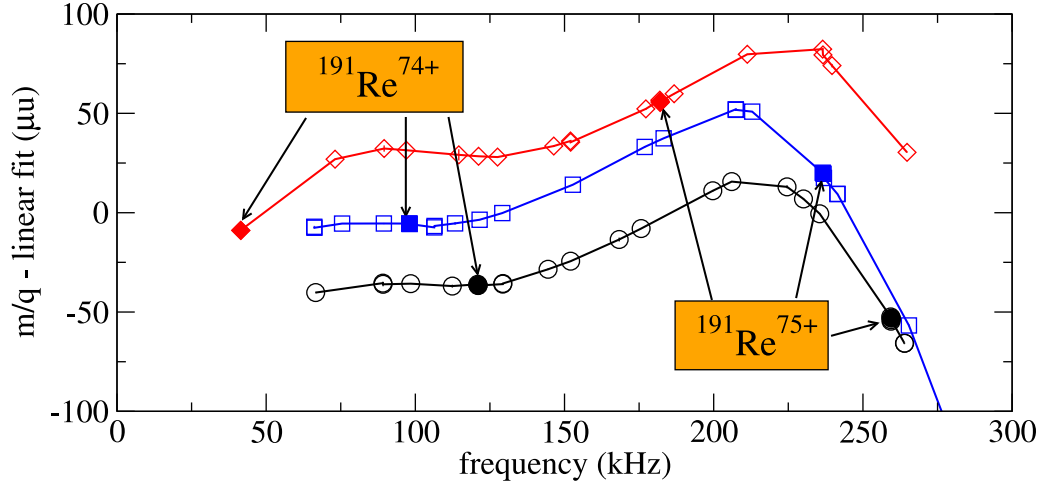


Fig. 4.9: Mass-to-charge ratio m/q as a function of frequency f with subtracted (arbitrary) linear fit for different experimental settings. As example $^{191}\text{Re}^{74+}$ and $^{191}\text{Re}^{75+}$ ions are shown in three spectra (settings are $U_c = 206, 206.5, 209$ kV and $LO = 58.06, 58.11, 58.3$ MHz for black, blue and red curves correspondingly).

wards average these values.

The second method is better in the sense that one does not introduce additional errors while averaging all spectra. This additional error can appear for the following reason: frequencies undergo some drifts and even after the software drift correction there exist residual shifts. On the other hand the centroid uncertainty is almost always larger than the residual drift (see Fig. 4.5). The first method has a clear advantage in the statistical sense: probability to have a reference in every isobar group is much larger after averaging. The latter argument is very significant, therefore the first method is applied.

As it was mentioned above, in the present experiment ten various settings were applied. The electron cooler potential U_c and the local-oscillator frequency were being changed in small steps. Therefore there is a significant overlap between all spectra. That means, under different settings ions have slightly different trajectories. By varying settings one moves ions along the $\frac{m}{q}(f)$ curve, as it is illustrated in Fig. 4.9.

The statistical uncertainty of mass value can be estimated as a sum of the uncertainty from the frequency centroid σ_f and the error from the spline calibration σ_{spline} . The latter is determined as a difference between the value of the spline passing through experimental points and the value of the spline passing through the upper edge of the corresponding error bars, as it is illustrated in Fig. 4.10:

$$\sigma_{stat}^2 = \sigma_f^2 + \sigma_{spline}^2. \quad (4.17)$$

Since the mass of each nuclide is calculated from several spectra independently, the

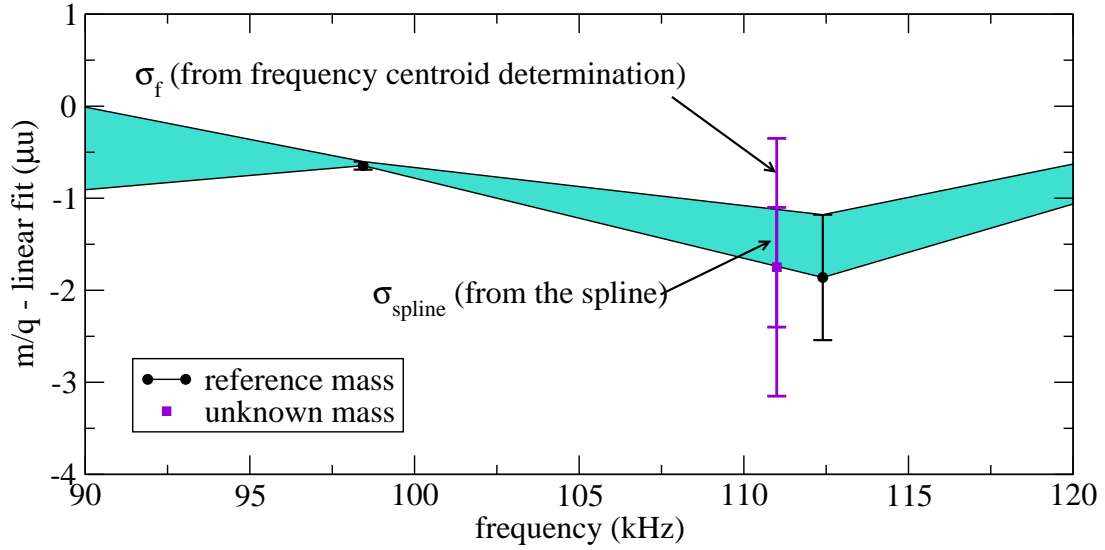


Fig. 4.10: The m/q ratio as a function of revolution frequency with subtracted linear fit. Turquoise color denotes areas between two splines: one goes directly through the data points, while the other passes through the upper edge of the data-point error bars. The error of the evaluated point would be the difference between these two spline values at a specified point summed up in quadrature with the uncertainty from the frequency centroid determination.

weighted mean is taken as its mass value. The weight w of a data point is determined as

$$w = \frac{1}{\sigma_{stat}^2}. \quad (4.18)$$

The statistical uncertainty depends on the number of spectra, in which the nuclide appears. The more spectra contain this nuclide, the smaller is the uncertainty. The systematic uncertainty can be estimated in the same way, as in the CMM, namely by “turning-off” all references and calculating their values as if they were unknown, then applying Eq. (4.14).

CHAPTER 5

Results and discussion

The analysis of the mass-spectrometry data acquired during the experiment described in this thesis was successfully accomplished. The mass evaluation was performed via two different methods: the CMM and the spline method, which are described in the previous chapter. In total 49 nuclides were identified in frequency spectra. Many of these nuclides were seen in two or three different atomic charge states. It is noted that isomeric states of some of these nuclides were resolved. Masses of eleven nuclides could not be calculated due to unresolved spectral traces or ambiguous identification. From the other 38, nine mass values were measured for the first time, three other mass values were measured with a higher accuracy than previously available. 18 nuclides were used as references for mass evaluation. The description and discussion of the results are given in this chapter.

5.1

Mass values measured for the first time

The mass values of the nine nuclides $^{181,183}\text{Lu}$, $^{185,186}\text{Hf}$, $^{187,188}\text{Ta}$, ^{191}W and $^{192,193}\text{Re}$ were measured for the first time. Also mass uncertainties for the three nuclides $^{189,190}\text{W}$ and ^{195}Os were significantly improved compared to their tabulated values [7]. All measured values, including the nuclides used as references, are listed in Tab. 5.1. As it was discussed above, the mass values for nuclides whose masses were known before were re-determined in the present analysis as if they were unknown, i.e. each reference nuclide was set one-by-one to “no-reference” and its mass value was obtained from the remaining 17 references. In Tab. 5.1 mass excess values ME (see Section 1 Eq. (1.3)) of the investigated nuclides obtained by the spline method are shown. A comparison to the alternative CMM method is discussed below.

In Fig. 5.1 the comparison of the obtained masses with the atomic-mass evaluation table (AME-03) [7] and the NuBase table [100] is shown. As can be seen, most of the masses agree well with the table values within about 100 keV. However, in order to be

Tab. 5.1: Mass excess values (ME) obtained with the spline method. Mass values measured for the first time and improved values are highlighted in dark gray (and bold font) and light-gray, respectively.

	El	Z	A	is*	ref [†]	exp [‡]	N_{set} [§]	ME , keV	$ME(AME)$, keV	$\delta^¶$, keV
1	Lu	71	181	0	0	1	1	-44797(126)	-44740(298)	-57
2		71	183	0	0	1	1	-39716(80)	-39523(298)	-196
3	Hf	72	181	0	1	0	1	-47412(55)	-47412(2)	0
4		72	182	1	0	0	4	-44840(50)	-44886(6)	46
5		72	183	0	0	0	1	-43214(47)	-43286(30)	76
6		72	184	0	0	0	1	-41603(76)	-41501(40)	-103
7		72	185	0	0	1	1	-38320(64)	-38359(196)	40
8		72	186	0	0	1	1	-36424(51)	-36431(298)	6
9	Ta	73	181	0	1	0	1	-48383(55)	-48442(2)	59
10		73	182	0	1	0	3	-46466(48)	-46433(2)	-32
11		73	183	0	1	0	3	-45276(41)	-45296(2)	20
12		73	184	0	0	0	6	-42804(42)	-42841(26)	37
13		73	185	0	1	0	6	-41350(41)	-41396(14)	46
14		73	186	0	0	0	5	-38520(40)	-38609(60)	90
15		73	187	0	0	1	2	-36896(56)	-36766(196)	-126
16		73	188	0	0	1	2	-33612(55)	-33813(196)	198
17	W	74	184	0	1	0	5	-45663(42)	-45707(1)	44
18		74	186	0	1	0	7	-42493(40)	-42510(2)	17
19		74	186	2	0	0	1	-38916(92)	-38967(3)	51
20		74	187	0	1	0	8	-39863(39)	-39905(2)	41
21		74	189	0	0	0	5	-35618(40)	-35478(200)	-138
22		74	190	0	0	0	7	-34388(41)	-34296(165)	-88
23		74	191	0	0	1	1	-31176(42)	-31112(196)	-66
24	Re	75	189	0	1	0	9	-38063(39)	-37978(8)	-85
25		75	191	0	1	0	9	-34364(38)	-34349(10)	-15
26		75	192	0	0	1	1	-31589(71)	-31708(196)	121
27		75	193	0	0	1	7	-30232(39)	-30302(196)	68
28	Os	76	188	0	1	0	7	-41115(40)	-41136(1)	21
29		76	190	0	1	0	7	-38637(41)	-38706(1)	69
30		76	190	1	0	0	9	-36998(38)	-37001(2)	3
31		76	192	0	1	0	7	-35833(39)	-35881(3)	48
32		76	193	0	1	0	7	-33329(39)	-33393(3)	63
33		76	195	0	0	0	1	-29512(56)	-29690(500)	178
34	Ir	77	190	2	0	0	2	-36372(62)	-36375(2)	3
35		77	191	0	1	0	1	-36650(80)	-36706(2)	56
36	Pt	78	194	0	1	0	4	-34779(45)	-34763(1)	-16
37		78	196	0	1	0	9	-32655(38)	-32647(1)	-7
38	Au	79	196	0	1	0	5	-31126(38)	-31140(3)	14

*Isomeric state: 0 — ground state, 1(2) — first (second) excited state

[†]Reference nuclides are marked with 1

[‡]0 — measured mass value, 1 — value estimated from systematic trends in AME-03 [7]

[§]The number of experimental settings, from which the mass value was obtained

[¶]Difference with AME-03 values: $\delta = m_{Spline} - m_{AME} = ME_{Spline} - ME_{AME}$

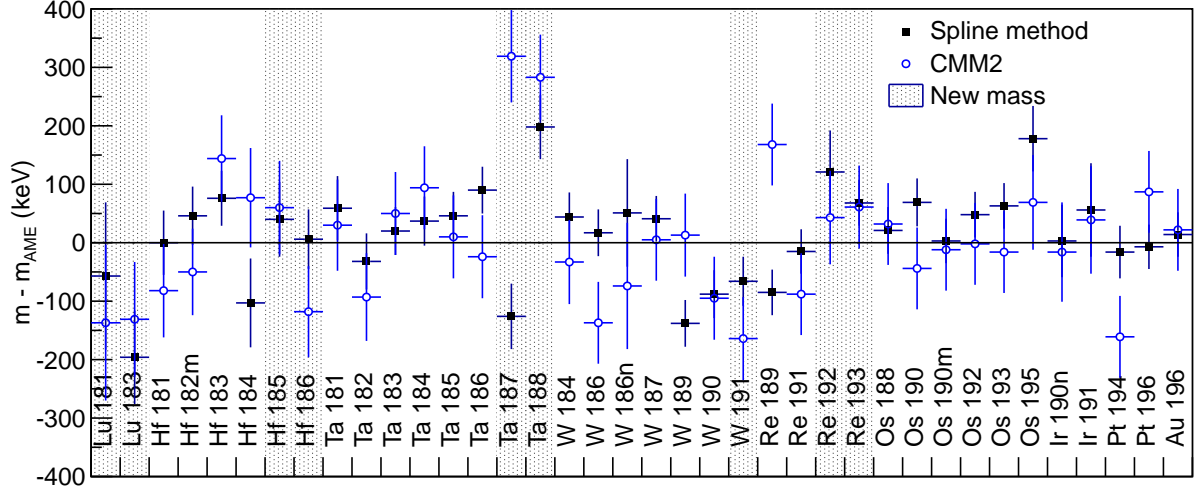


Fig. 5.1: A comparison of the new measured masses obtained with the CMM (blue open circles) and the spline method (black squares) with the AME-03 table [7] (and the NuBase table [100] from which the information for isomeric states was extracted). The error bars represent the total uncertainty $\sigma_{tot} = \sqrt{\sigma_{stat}^2 + \sigma_{sys}^2}$.

able to choose one of the methods, the CMM or the spline one, one needs to make a deeper investigation.

One can take the difference between values obtained by the different methods for each nuclide, as it is shown in Fig. 5.2. Note that most of the points are above the zero-axis, which can be due to overstating or understating trends in either or both methods. It should also be mentioned that although most of the values differ within 100 – 150 keV, the value of ^{187}Ta differs by 400 keV. This can be due to quadratic polynomial fitting in the CMM as shown in Fig. 5.3. To investigate further the overall shift of the differences, it is useful to investigate the distributions of the δ -values of the re-calculated reference masses.

In Fig. 5.4 histograms of corresponding differences $\delta_i^{Spline} = m_i^{Spline} - m_i^{AME}$ as well as $\delta_i^{CMM} = m_i^{CMM} - m_i^{AME}$ for reference masses are shown. The histograms are filled with deviation values δ_i with the weights

$$w_i = \frac{1}{\sigma_i^2} = \frac{1}{\Delta\delta_i^2}, \quad (5.1)$$

where $\Delta\delta = \sqrt{\sigma_{st}^2 + \sigma_{AME}^2}$.

As can be seen from the histograms in Fig. 5.4, the distributions of δ corresponding to the two methods look different: the spline distribution is narrower, all reference masses are re-determined within approximately 100 keV, the CMM distribution is broader, and therefore the systematic error of this method (which is essentially a standard deviation of this distribution) is larger. One can find the centroids of these distributions by calculating

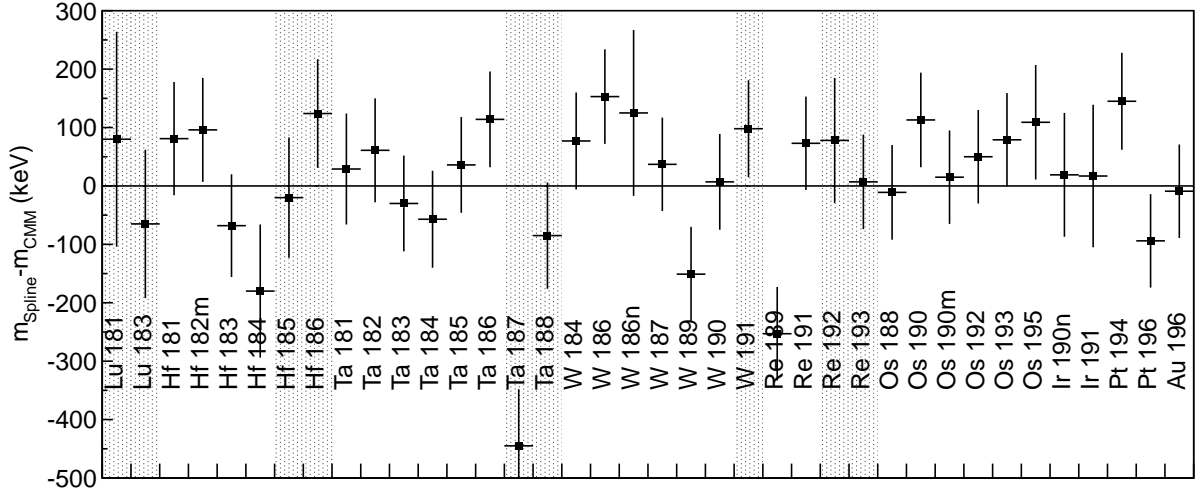


Fig. 5.2: A comparison of the measured masses between the CMM and the spline methods. Each point on the plot corresponds to $m_i^{Spline} - m_i^{CMM}$, with an uncertainty $\sqrt{(\Delta m_i^{Spline})^2 + (\Delta m_i^{CMM})^2}$.

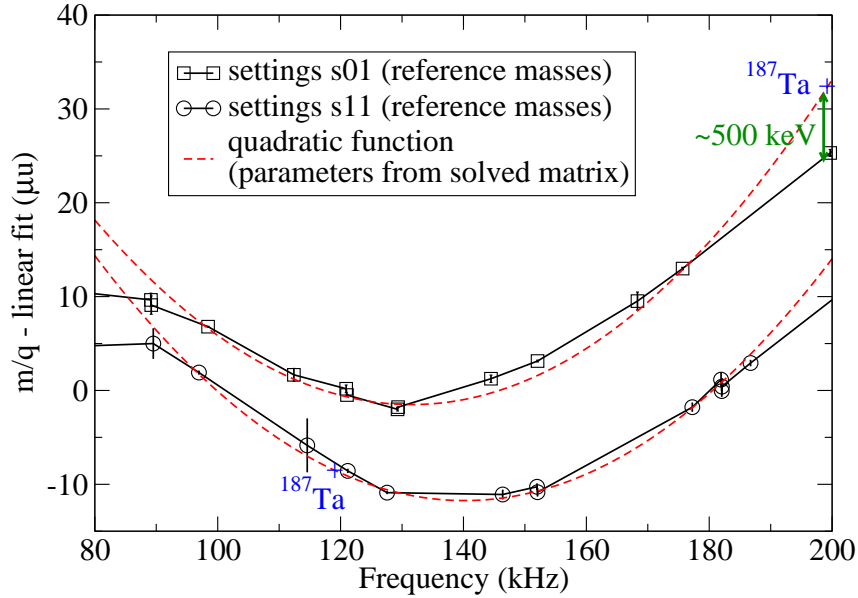


Fig. 5.3: The $\frac{m}{q}(f)$ dependence curves, which corresponded to two different experimental settings. The ^{187}Ta placement is marked with blue crosses. The plot shows why the CMM and the spline methods give different estimations of the ^{187}Ta mass: the reason is the extreme off-center location of the nuclide in one of two spectra, in which it is available.

Tab. 5.2: The weighted means of δ -values for 18 nuclides used as references.

	$\bar{\delta}$	\pm	$\Delta\bar{\delta}$
Spline method	(13	\pm	7) keV
CMM	(-3	\pm	19) keV

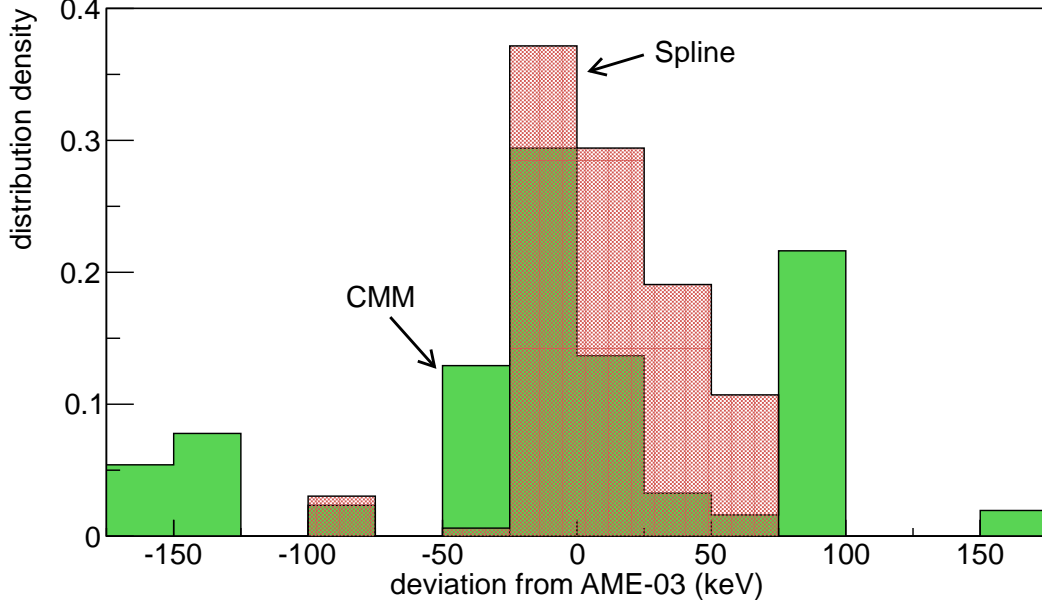


Fig. 5.4: The distributions of δ -values for the masses used as references. One bin of the histogram corresponds to 25 keV. The spline distribution is shown in orange color while the CMM one in green. The distributions are normalized to 1.

the weighted means:

$$\bar{\delta} = \frac{\sum(\delta_i w_i)}{\sum w_i}, \quad (5.2)$$

where the summation runs over the number of references. The standard deviation of the weighted mean is:

$$\Delta\bar{\delta} \equiv \sigma_{\bar{\delta}} \cdot \chi_{red} = \sqrt{\frac{1}{\sum w_i}} \sqrt{\frac{\sum(\delta_i - \bar{\delta})^2 w_i}{N - 1}}, \quad (5.3)$$

where $N = 18$ is the number of references.

The weighted means $\bar{\delta}$ of distributions of δ shown in Fig. 5.4 are given in Tab. 5.2. One can find, that the spline mean $\bar{\delta}_{spline}$ is 13 keV above zero, while the CMM mean $\bar{\delta}_{CMM}$ is 3 keV below zero, though both mean values are compatible with zero within two σ . This confirms the observation in Fig. 5.2 that most of the points are above the zero-axis.

The systematic error can be calculated as a standard deviation of the δ distribution of the references in the following way:

$$\sigma_{st.dev.}^2 = \frac{\sum[(\delta_i - \bar{\delta})^2 w_i] \sum w_i}{(\sum w_i)^2 - \sum w_i^2}. \quad (5.4)$$

This formula is essentially very similar to the previously discussed procedure of error

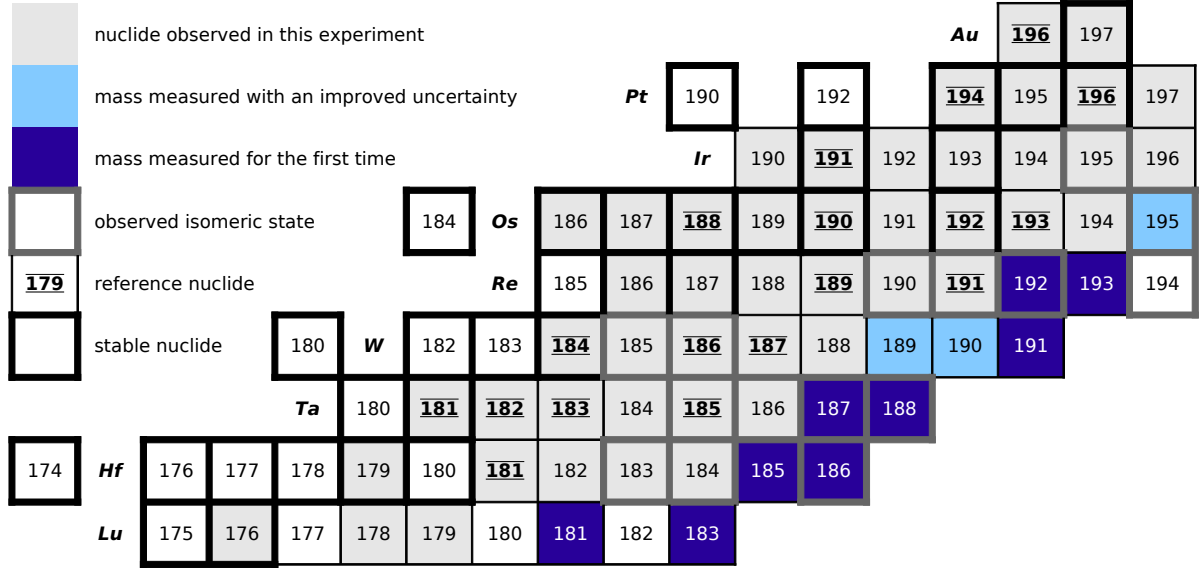


Fig. 5.5: All nuclides that were identified in the experiment are marked with colored squares. The dark-blue ones correspond to nuclides, whose masses were measured for the first time; the light-blues correspond to nuclides, whose mass uncertainties were significantly improved compared to their previous values. Nuclides with observed isomeric states have grey frames.

propagation, see Eq. (4.14).

The systematic errors given by Eq. (5.4) are 34 and 82 keV for the spline and for the CMM methods, respectively (38 and 70 keV if calculated by Eq. (4.14)).

As a conclusion to what was said above, the spline method was chosen, because it has smaller systematic uncertainty. The CMM method is less reliable. This is caused by second degree polynomials (higher degrees are not possible due to low statistics). Low reliability results in the higher systematic uncertainty of the CMM.

A general view of identified nuclides in the spectra is shown in Fig. 5.5.

5.2

Comparison to mass models

A comparison of newly measured masses to several often used mass models is illustrated in Fig. 5.6. In order to characterize the predictive power of theoretical models the *rms* deviation σ_{rms} can be introduced [101]:

$$\sigma_{rms}^2 = \frac{1}{n} \sum (m_{theory} - m_{exp})^2, \quad (5.5)$$

where the summation runs through n compared nuclides (here $n = 9$).

Interesting to note is that older macroscopic-microscopic models, e.g. FRDM-95 [17] and Duflo-Zuker [32] models (both were developed around 1995) have relatively large *rms* deviations: $\sigma_{rms} = 1.11$ and 1.00 MeV respectively. While the most recent microscopic

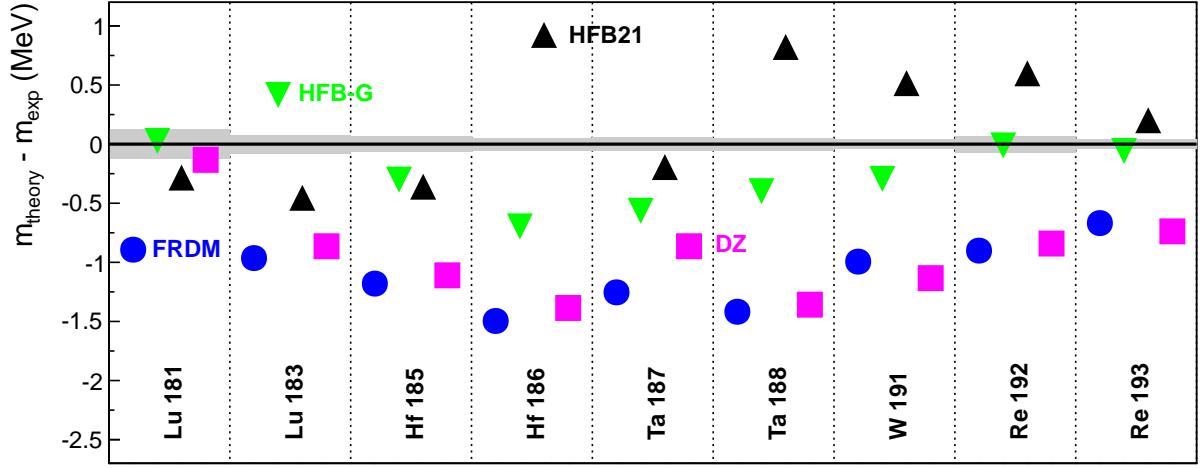


Fig. 5.6: The comparison of masses measured for the first time in this work with prediction of mass models. The experimentally measured mass values for nine nuclides are compared with HFB21 [30] (black triangles), HFB-Gogny [31] (green triangles), Duflo-Zuker [32] (magenta squares) and FRDM-95 [17] (blue circles) models. Grey band represents uncertainties of mass evaluation.

models, HFB21 [30] and HFB-Gogny [31] developed in 2009, have *rms* deviations of 0.54 and 0.38 MeV respectively.

5.3

Two-neutron separation energies

Since the present mass measurements aimed at the neutron-rich side of the nuclear chart, information on the neutron drip-line or on the r-process pathway can be gained. Therefore the two-neutron separation energies should be investigated. However, the region between $110 \leq N \leq 120$ and $71 \leq Z \leq 76$ is far away from both the drip-line and the assumed r-process pathway. The newly calculated two-neutron separation energies (the formulae are given in Tab. 2.2) are of about 11-12 MeV (see Fig. 5.7), while the r-process takes place around neutron separation energies of about 5 MeV and the neutron drip-line is the zero separation energy by definition.

As described in Section 2.3, the shell structure and deformations can also be investigated based on the separation energies. However, this (Z, N) region is far from nuclear shell closures, the closest magic numbers are $N = 126$ and $Z = 82$. Nevertheless, this region is interesting for the investigation of nuclear deformations. This region is also known for the unique interplay of single-particle orbitals which favor high-K high-energy long-lived isomeric states [102]. Part of the data from this experiment were analyzed in this respect and several new isomeric states were discovered (see Ref. [103]).

The two-neutron separation energies S_{2n} in the investigated region are plotted in Fig. 5.7. By inspecting this figure one can observe “knees” and “ankles” in the monotonic

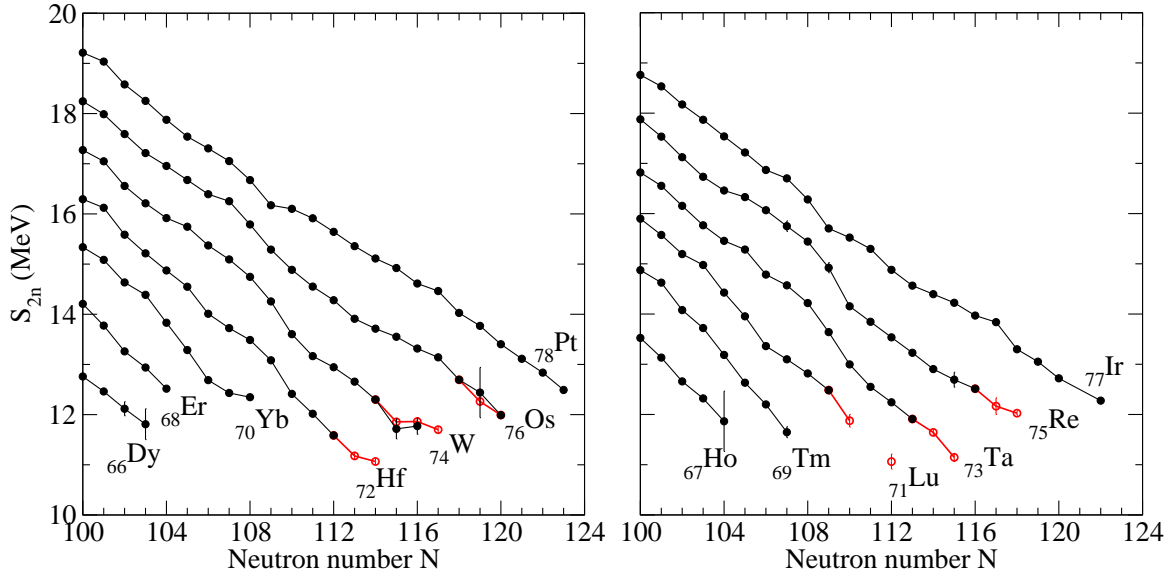


Fig. 5.7: Two-neutron separation energies for the region covered by the present mass measurements. The values obtained from improved masses or from masses measured for the first time within this thesis are marked in red color. The left panel shows the two-neutron separation energies for the nuclei with even number of protons, the right panel with odd number of protons.

decrease of the separation energies.

In order to find out, whether these features correspond to some changes in the collective behavior of nucleons (deformations), one can compare the separation energies of given nuclides with other nuclear properties, for which a known relation exists between their behavior and collectivity. Examples of such nuclear properties are excitation energies of the first 2^+ state and the ratio between excitation energies of the first 4^+ and first 2^+ states R_{42} , which are available from spectroscopic data (see Section 2.3).

In order to see features more clearly, we can look at the difference between $S_{2n}(N)$ and a linear fit (in order to see features more clearly) and compare it with the first 2^+ level energies (see Fig. 5.8).

There are “knees” (\wedge) in the S_{2n} at the places, where the 2^+ energies show sudden drops (Pt and Os at $N = 98 - 100$, Os at $N = 106 - 108$), and there are “ankles” (\vee) in the S_{2n} at the places, where the 2^+ energies show sudden jumps (Pt at $N = 108 - 110$ and W at $N = 114 - 116$). The improved mass values of W at $N = 115 - 116$ reproduce well this behavior. However, the newly improved value for Os at $N = 117$ does not show any significant feature, as it could be expected from systematic discussed above.

Sudden drops in the energies of 2^+ states is typically associated with growing collectivity, while sudden jumps show the approach to spherical shapes. However, the energies of the first 2^+ level are a more direct indicator of these collective effects than the S_{2n} energies.

The two-neutron separation energy can be divided in two parts: regular part S_{2n}^r , caused by regular binding between nucleons, and collective part S_{2n}^{col} , caused by collective

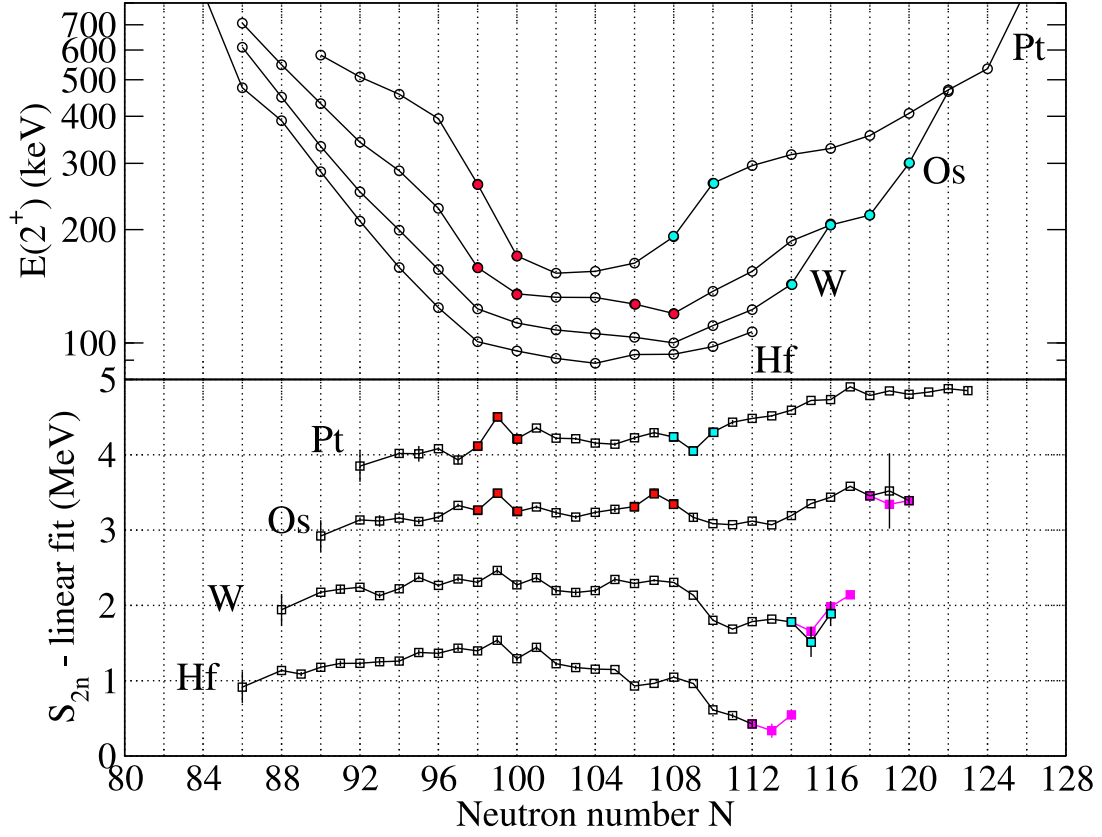


Fig. 5.8: Comparison between energies of the first 2^+ states and the two-neutron separation energies (S_{2n}) for the elements with even Z numbers in the region of the present mass measurements. Magenta squares correspond to newly measured and improved data. Red squares and circles correspond to the places of “knees” in S_{2n} and sudden drops in 2^+ energies, respectively. Cyan squares and circles correspond to the places of “ankles” in S_{2n} and sudden jumps in 2^+ energies, respectively.

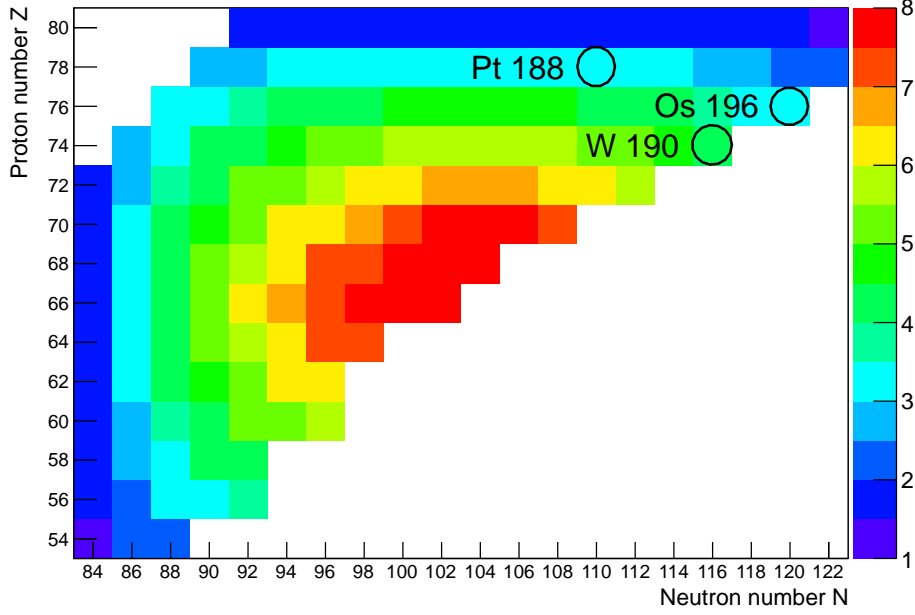


Fig. 5.9: The P -factor ($\frac{N_p N_n}{N_p + N_n}$) reflects the number of valence nucleons and holes. ^{188}Pt and ^{190}W (P-values 3.2 and 4.4, respectively) show higher sensitivity to collective effects in S_{2n} than ^{196}Os (P-value 3).

effects:

$$S_{2n} = S_{2n}^r + S_{2n}^{col}. \quad (5.6)$$

A useful quantity is the P-factor which is defined as [104]:

$$P = \frac{N_p N_n}{N_p + N_n}, \quad (5.7)$$

where N_p and N_n are the numbers of valence protons and neutrons, respectively. By analogy with the valence electrons, the number of valence nucleons is the number of nucleons or holes with respect to nearest closed shell. The P-factor can be used as a measure of possible collectivity: large numbers correspond to strongly deformed nuclei, while the zero value to spherical nuclei with magic neutron or proton numbers (see in Fig. 5.9).

The ^{188}Pt and ^{190}W marked in Fig. 5.9 have P -factor values of 3.2 and 4.4, respectively, while ^{196}Os also marked with a circle has $P = 3$. One can conclude that there is no significant drop in the $S_{2n}(\text{Os})$, because it is closer to sphericity, where the collective binding only gives a nonsignificant contribution to the total S_{2n} energy.

For more information about collective contributions to two-neutron separation energies see Ref. [105].

Pairing-gap energies

The pairing-gap energies are fundamental quantities that characterize the strength of nucleon-nucleon pairing correlations in nuclei. It is not possible to measure pairing-gap energies directly. However they can be related to odd-even staggering of nuclear binding energies (OES), that is the distance between the odd- A and even- A mass parabolas for even- Z isotopes (see Fig. 5.10). The OES can be calculated from 3, 4 or 5 masses of neighboring nuclides (see Tab. 2.2).

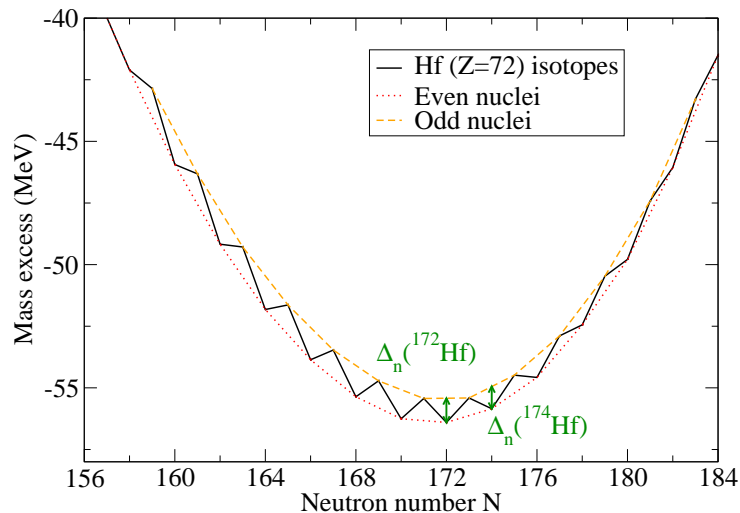


Fig. 5.10: The neutron pairing-gap energies for Hf isotopes. The orange dashed line corresponds to the isotopes with an odd number of neutrons. The red dotted line corresponds to the isotopes with an even number of neutrons. The distance between these two lines at a given neutron number represents the odd-even staggering and can be calculated using 3, 4 or 5 neighboring isotopes via the formulae from Tab. 2.2.

The OES can also contain some information about deformation; therefore it is interesting to compare pairing-gap energies with some other properties of nuclei to find possible explanations of observed trends. As it can be seen in Fig. 5.11, there is an overall decrease of the neutron and proton pairing-gap energies with the neutron number. For magic neutron numbers the R_{42} ratio is minimal, while the neutron pairing-gap energies exhibit sudden peaks.

Interesting to note is that some regions of the pairing-gap energies show steeper slope, for example both the neutron and the proton pairing-gap energies around $N = 90 - 100$. The comparison of experimental and theoretical data of the neutron pairing-gap energies in this region is shown in Fig. 5.12; the dependence of Δ_n on isospin projection ($I_z = \frac{N-Z}{2}$) was discovered and discussed in Ref. [106]. The most interesting fact is that many presently available mass models, e.g. FRDM [17], Duflo-Zuker [32] and HFB [30], cannot reproduce this behavior.

The comparison of the pairing-gap energies with the R_{42} ratio reveals interesting phe-

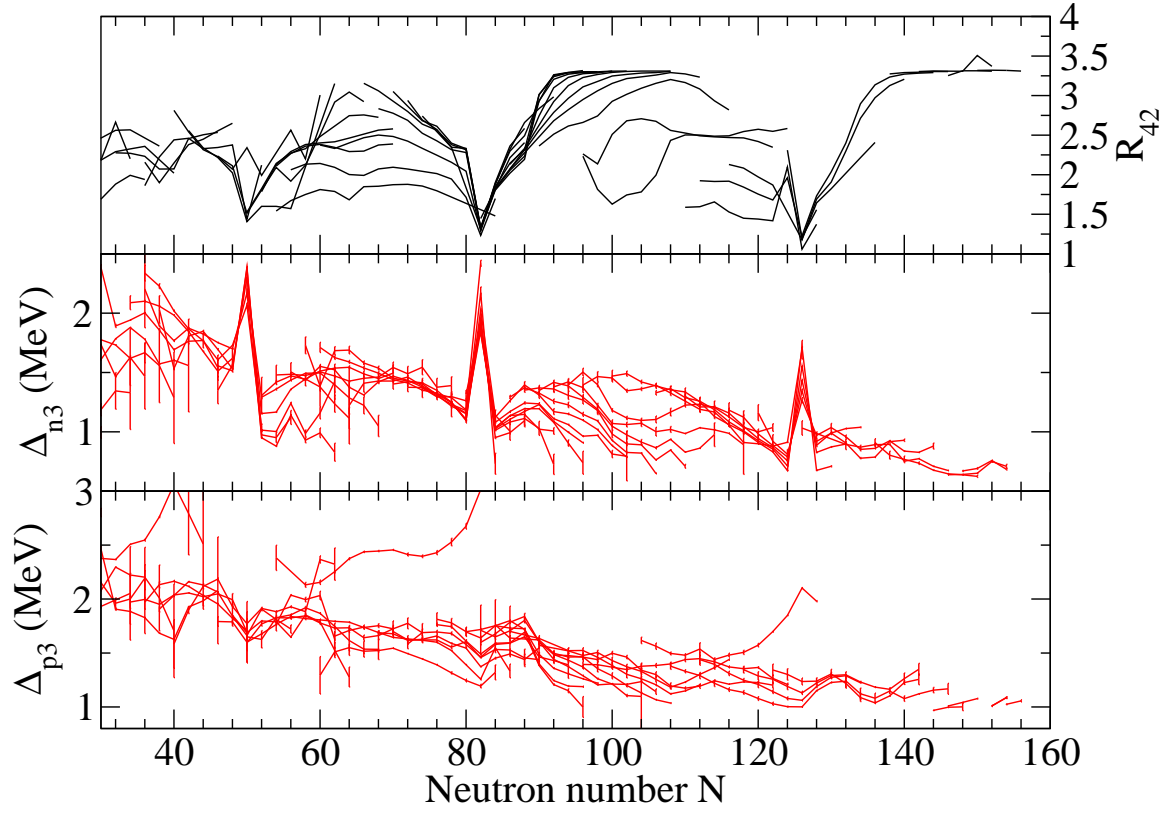


Fig. 5.11: The neutron (middle panel) and the proton (lower panel) pairing-gap energies as functions of neutron number in comparison with the R_{42} quantity (upper panel). Points connected with a line represent different isotopes of one element.

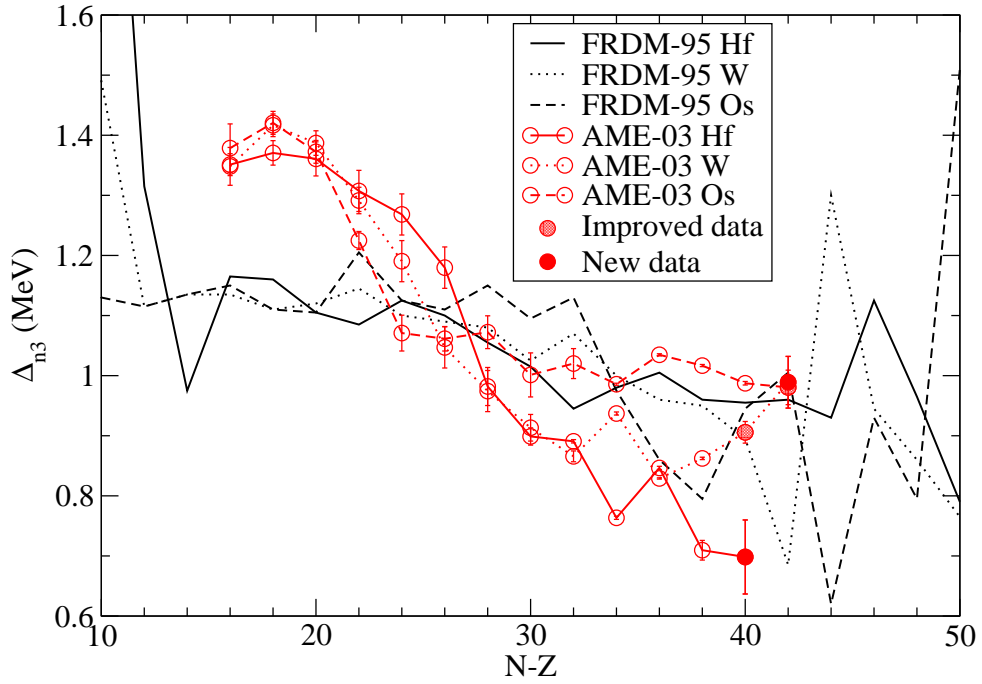


Fig. 5.12: Neutron pairing-gap energy for Hf-W-Os isotopes in comparison with values from the FRDM mass model.

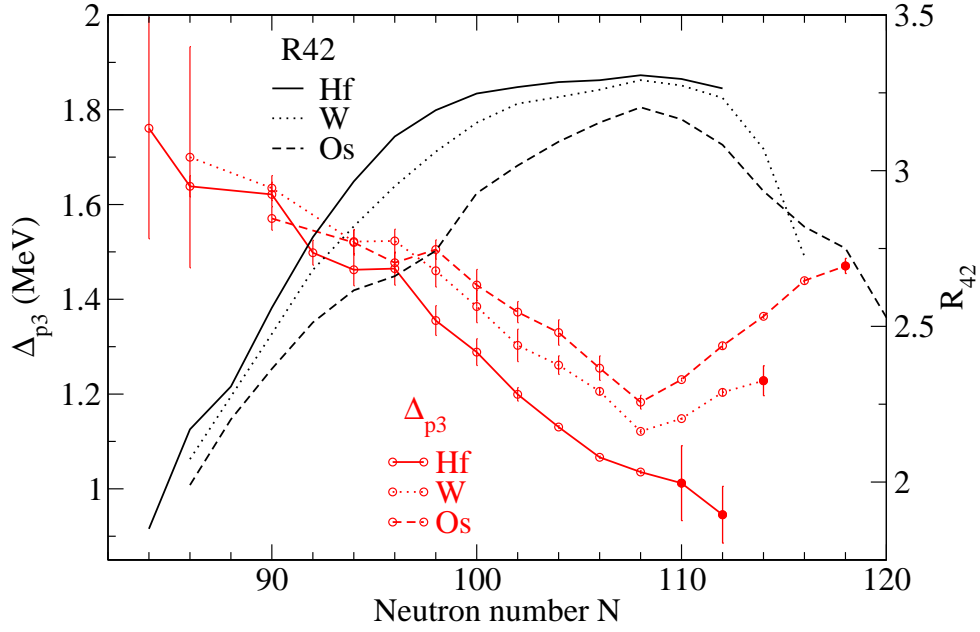


Fig. 5.13: The proton pairing-gap energies for Hf-W-Os isotopes in comparison with the R_{42} ratios. The turning point is observed at $N = 108$ for W and Os in both the R_{42} ratios and the pairing-gap energies; the new data points for the Hf isotopes (marked with full circles) show no turning point in the proton pairing-gap energy.

nomena around $N = 108$ (see Fig. 5.13). At $N = 108$ the pairing gaps in one hand and R_{42} values in the other hand have an apparent turning point for Os, which is however less obvious for W. The neutron number $N = 108$ corresponds to the region of maximum deformations for Os and W. The subsequent decrease of the R_{42} is a signature of decreasing deformations.

For Hf it is clear that the pairing gap has monotonic decreasing trend. The $R_{42}(\text{Hf})$ ratio also has constant slope for $N = 100 - 112$. Therefore it is very desirable to do further investigations in this region in order to find out, whether this turning point in the proton pairing-gap energies can be related to collectivity or it is just a coincidence.

CHAPTER 6

Summary and outlook

The present thesis is dedicated to the Schottky mass spectrometry of heavy nuclides on the neutron-rich side of the chart of nuclides. This part of the chart of nuclides is still not well-investigated, though the short-lived neutron-rich nuclides between proton shell closures at $Z = 50$ and 82 are expected to provide indispensable information for our understanding of nuclear structure as well as for network calculations of r-process nucleosynthesis in stellar environments. The experiment providing new data in this region was conducted in 2009 at GSI with ^{197}Au fragmentation. The motivation for this mass measurement and possible applications of results are discussed in Chapter 2. The experiment and employed settings are described in Chapter 3. The analysis of the acquired data and the description of existing and newly developed mass-evaluation methods, the CMM and the spline method, are discussed in detail in Chapter 4. Obtained results, among which are newly measured masses of nine nuclides $^{181,183}\text{Lu}$, $^{185,186}\text{Hf}$, $^{187,188}\text{Ta}$, ^{191}W and $^{192,193}\text{Re}$ and improved uncertainties of mass values of three nuclides $^{189,190}\text{W}$ and ^{195}Os , are listed in Tab. 5.1. Further applications of the new data in nuclear structure studies are discussed in Chapter 5, where the main focus is given to a connection of two-neutron separation energies as well as pairing-gap energies to nuclear collective effects. In this chapter the perspectives of in-ring mass spectrometry at the future new-generation radioactive beam facilities worldwide are outlined.

6.1

Past and future of the ESR

In Fig. 6.1 a chart of nuclides is shown. The nuclides with the masses measured by storage-ring mass spectrometry at the ESR and the masses of a few proton-rich nuclides measured at CSRe are marked in red color, and the nuclides with the masses measured by Penning-trap mass spectrometry are shown in blue. As one can see, over the past decades many hundreds of masses were measured at the ESR facility, using both the SMS and the

IMS techniques. Nuclides described in this thesis are not shown in this figure (they are presented in Fig. 5.5).

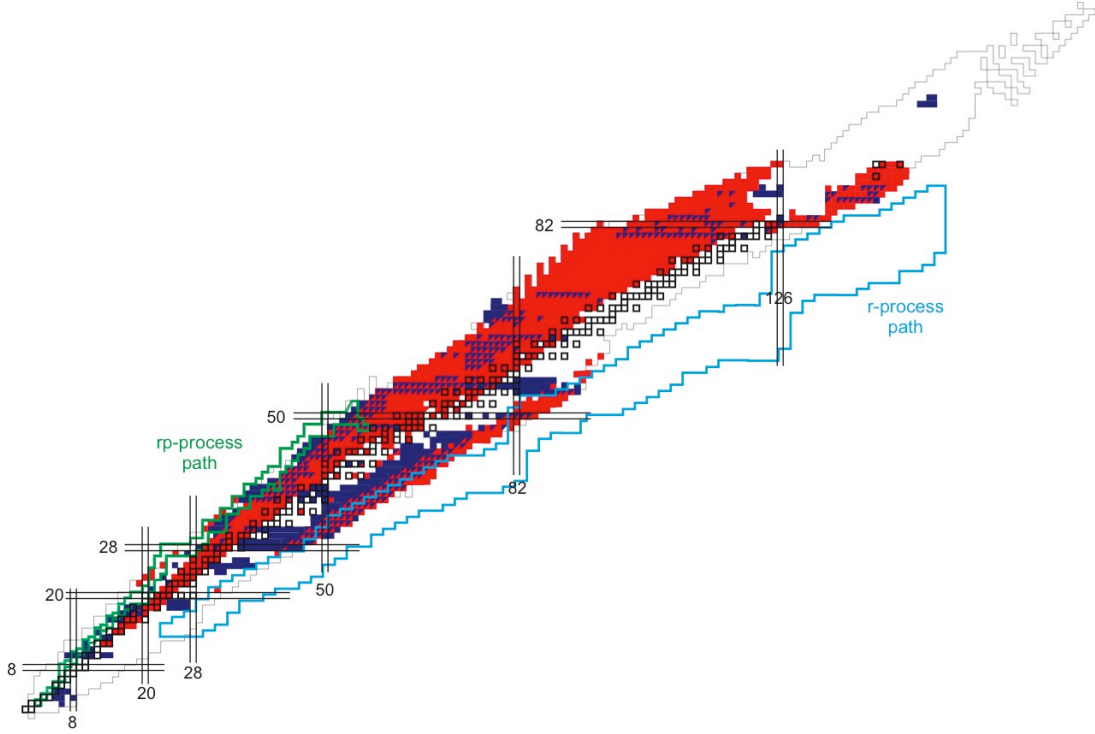


Fig. 6.1: The chart of nuclides, where nuclides whose masses were measured with storage rings (ESR at GSI and CSRe in Lanzhou) are marked with red color and whose masses were measured with different Penning traps with blue color. The chart considers only the most precisely measured values. Nuclides with the mass measured with other methods are colorless. Masses measured for the first time in the measurements described in this thesis are not shown in the chart (they are presented in Fig. 5.5).

In 2010 a new Schottky resonant detector was installed in the ESR [107]. The new detector is based on a resonant cavity principle. The working frequency is around 250 MHz, which corresponds to 125th harmonic of the ions revolution frequency, while the older capacitive pick-up detector operates on 30th harmonic. The new detector has a much better signal-to-noise characteristics, which is by a factor of about 100 higher than that of the older detector. The new resonator has a much higher sensitivity, however it covers a narrower band of frequencies, which makes it not possible to do the broad-band mass measurements, as discussed in this thesis. Nevertheless, narrow-band measurements can be done with a much higher quality. More information about the new resonant pick-up can be found in Ref. [108].

Narrow-band mass measurements are well-suited for isomer studies, when one needs to focus on a particular ion, as well as for the half-life measurements.

The high time resolution allows the application of the detector to accurate measurements of in-ring radioactive decays. Examples of this are studies of β -decays and β -delayed decays [109]. The three-body β -decay results in a decrease of charge state, if the electron

goes away. The Q -values of three-body β -decays extend from several hundred keV to a few MeV, in case of β -delayed neutron emission about several MeV. This difference in $B\rho$ between parent and daughter nuclei does not allow to have them both in the narrow-band spectrum. However, two narrow-band devices placed along in the storage ring could solve this problem.

The SMS technique requires cooling and therefore has limitation concerning the lifetime of an investigated particle, because of relatively long cooling times (up to some ten seconds). To study short-lived nuclei in a storage ring the IMS technique is usually applied and a TOF detector is used. Usage of the new Schottky resonant detector with the ESR tuned to the isochronous mode allowed us to investigate particles with half-lives on a time scale of below 100 ms [110].

6.2

CSRe storage ring

Another storage ring for mass measurements is the cooler storage ring (experimental) CSRe at the Institute for Modern Physics (IMP) in Lanzhou, China [111]. The schematic view of the experimental facilities at IMP is shown in Fig. 6.2. There are two storage rings: one, cooler storage ring (main) CSRm, is used as synchrotron for acceleration of the primary beam, another, CSRe, for storage and subsequent measurements. Combination of two rings CSRm+CSRe is analogous to the combination of SIS-18+ESR at GSI. At present time there is only IMS available. A mass-measurement program on neutron-deficient nuclei started in 2007 and lead in 2009 to the very successful measurements of the masses of ^{63}Ge , ^{65}As , ^{67}Se , and ^{71}Kr ($A = 2Z - 1$) for the first time using the IMS with a TOF-detector [112]. The IMS-measurement program was continued in 2011 on nuclei with $A = 2Z - 2$ in the region of $23 \leq Z \leq 29$, resulting in several newly measured masses [113]. Furthermore a new Schottky resonant detector, identical to the one installed in the ESR at GSI, was built and already tested for further measurements [108, 114].

6.3

FAIR and ILIMA

While the number of Penning trap facilities for high-precision mass measurements in the world grows rapidly, the storage-ring spectrometry has also bright future perspectives. The construction of the new FAIR (FaciLity for Antiproton and Ion Research) project is being started at GSI. FAIR foresees in its final form much more powerful synchrotrons SIS-100/300, which will accelerate beams up to 10 GeV/u, the Super-FRS — a fragment separator of a new generation designed to separate fission fragments — and a complex of storage rings: CR + RESR, HESR and a NESR (collector ring, recuperated, high-energy and new ESR). These storage rings and the fragment separator are the basis of the new

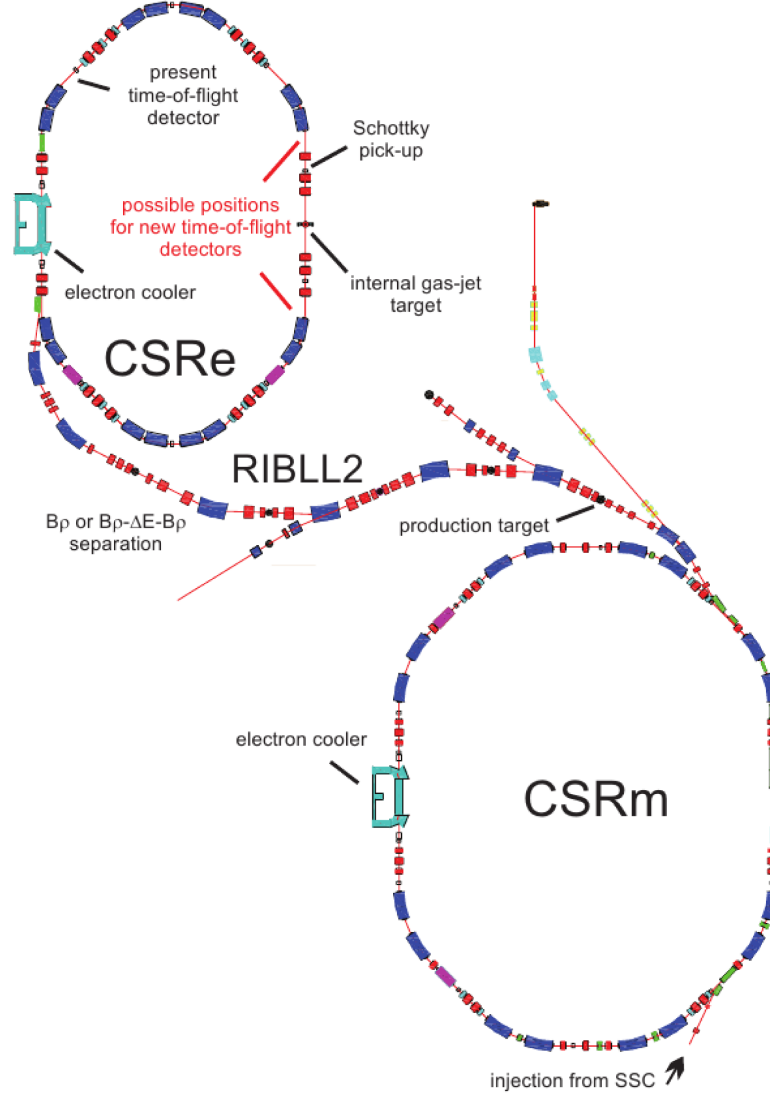


Fig. 6.2: Schematic view of the radioactive beam facility at IMP, Lanzhou [111]. The synchrotron CSRm accelerates primary beams which are then fragmented in a production target located in front of the in-flight fragment separator RIBLL2. Separated radioactive ions are injected and stored in the storage ring CSRe. The revolution frequencies of the electron-cooled ions can be measured by means of a Schottky pick-up. If the CSRe is tuned to the isochronous ion-optical mode, the revolution frequencies can be obtained also for uncooled particles by using dedicated time-of-flight detectors.

experimental project ILIMA (**I**someric Beams, **L**ifetimes and **M**asses) [115].

In Fig. 6.3 nuclides that will be available for investigation by ILIMA are shown. The main improvement of the present capability of GSI is the number of particles that can be accelerated by the new synchrotron: while SIS-18 allows — due to space-charge limits for heavy ions — presently only about 10^9 particles per spill, SIS-100/300 will allow 10^{11} or even more (accelerating in the synchrotron the ions at a lower charge state). That will increase the production yields of fragments by at least two orders of magnitude. Another significant improvement is the connection between the new fragment separator and storage rings, well-adjusted to have high transmission: about 80%, while FRS-ESR provides today transmissions of only about 1%. This will also increase the number of stored particles by a factor of 100. All these improvements will allow us to study nuclides with production cross-section of about 10^{-16} b. GSI allows minimal production cross-section of about 10^{-12} b*.

New regions on the chart of nuclides, which become available at FAIR, will allow us to study nuclides closer the astrophysical r-process as well as the end part of rp-process. In Fig. 6.3 assumed locations of r-process pathways are shown, the area between the red lines correspond to the r-process pathways at neutron densities of 10^{20-26} cm⁻³ and a temperature of $1.35 \cdot 10^9$ K.

*These numbers correspond to production rate of 1 particle per week in respect to an injection rate of one per second.

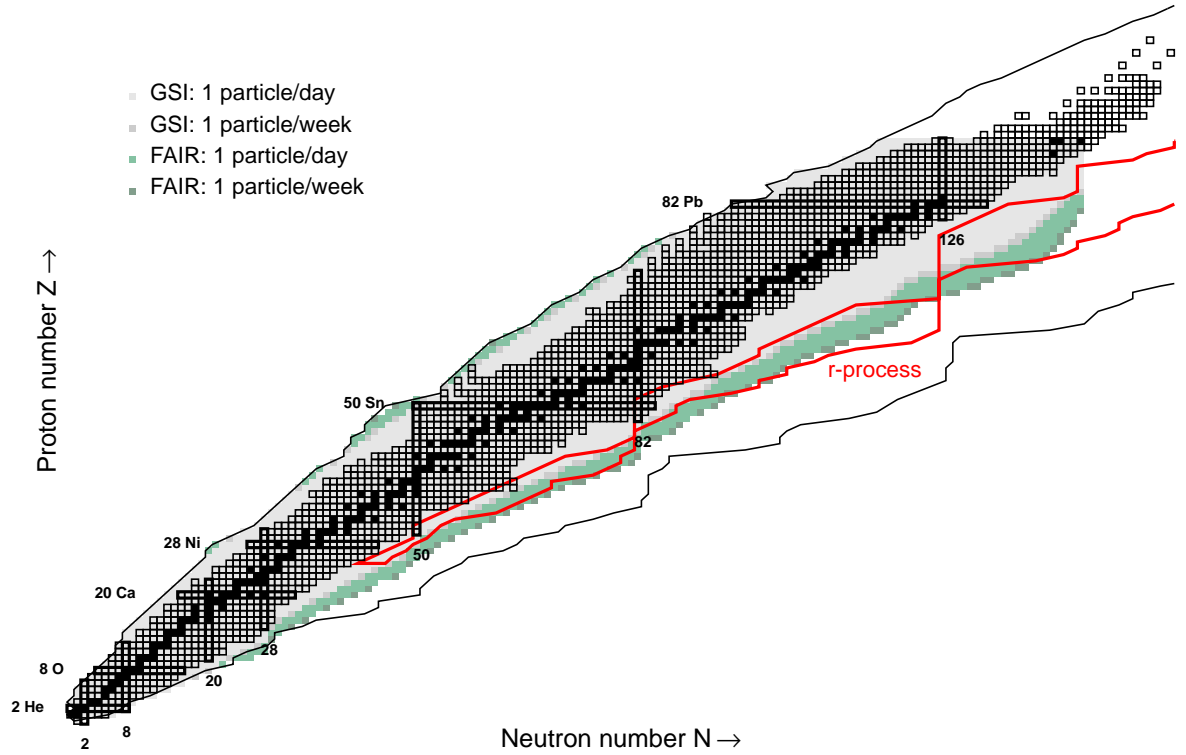


Fig. 6.3: The chart of nuclides that shows all nuclides with measured masses according to AME-03 [7] (black-framed squares are radioactive nuclides, full black squares are stable nuclides), the nuclides with the production rate (via fragmentation of the most appropriate beam for this nuclide) down to 1 particle per day and 1 particle per week for GSI (light and dark grey colored squares) and FAIR (light and dark green colored squares). The solid black lines correspond to the proton and presumable neutron drip-lines (according to FRDM model). The red solid line corresponds to presumable locations of the r-process pathways.

APPENDIX A

The α_p curve

The revolution frequencies f , the mass-to-charge ratios m/q and the velocities v of stored ions in the ESR storage ring are connected with the following relationship:

$$\frac{\Delta f}{f} = -\alpha_p \frac{\Delta(m/q)}{(m/q)} + \frac{\Delta v}{v} (1 - \alpha_p \gamma^2), \quad (\text{A.1})$$

where α_p is a non-linear ion-optical parameter of the ring, called momentum compaction factor:

$$\alpha_p = \frac{dC/C}{d(B\rho)/B\rho}, \quad (\text{A.2})$$

where C is the path length of the ions with a magnetic rigidity $B\rho$ per one revolution.

Derivation of Eq. (A.1)

It is interesting to derive this equation, let us do it here. One can start from the definition of revolution frequency:

$$f = \frac{v}{C}, \quad (\text{A.3})$$

where v is the velocity of a particle in the storage ring and C is the pathway length (circumference).

By differentiating Eq. (A.3) one gets:

$$\frac{df}{f} = \frac{dv}{v} - \frac{dC}{C}. \quad (\text{A.4})$$

In Fig. A.1 (left panel) the particle trajectory with the coordinate system (x,y,s) is

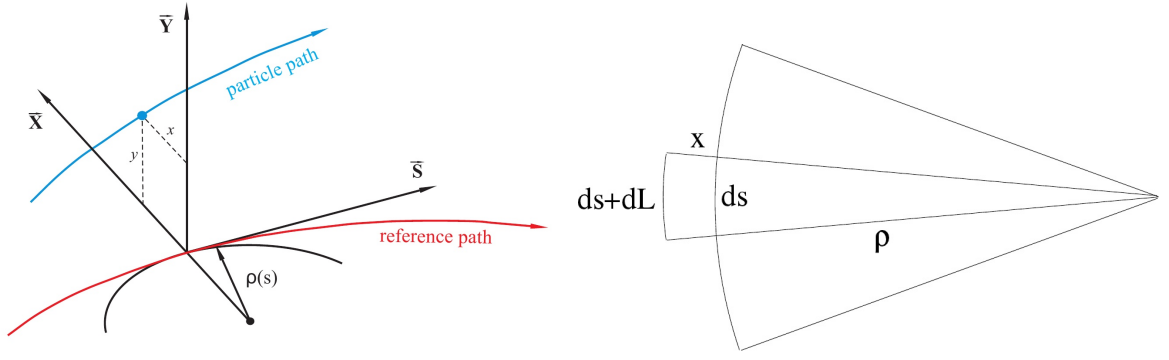


Fig. A.1: Left panel: the moving curvilinear coordinate system (x, y, s) in ion-optics. The particle motion is described by a deviation from a reference path (taken from Ref. [116]). Right panel: a comparison of a central orbit trajectory with a shifted trajectory. The ion with the magnetic rigidity $B\rho$ moves on the trajectory ds , while the ion with $B\rho + dB\rho$ moves on the trajectory $ds + dL$ (taken from Ref. [117]).

shown. Let us introduce the momentum compaction factor α_p as

$$\alpha_p = \frac{1}{C} \oint \frac{D(s)}{\rho} ds, \quad (\text{A.5})$$

where ρ is the bending radius of a magnet, s a coordinate in horizontal plane and $D(s)$ a dispersion function. The dispersion function is defined as:

$$D(s) = \frac{x(s)}{d(B\rho)/(B\rho)}, \quad (\text{A.6})$$

where $x(s)$ is shift from a central orbit of a particle with magnetic rigidity $B\rho$.

As can be seen from Fig. A.1 (right panel)

$$\frac{\rho}{\rho + x} = \frac{ds}{ds + dL} \quad \text{or} \quad (\text{A.7})$$

$$\frac{x}{\rho} = \frac{dL}{ds}. \quad (\text{A.8})$$

Inserting this and Eq. (A.6) into Eq. (A.5) we obtain:

$$\alpha_p = \frac{1}{C} \oint \frac{dL}{d(B\rho)/(B\rho)} = \frac{dC/C}{d(B\rho)/(B\rho)}, \quad (\text{A.9})$$

where $dC = \oint dL$ is the difference in the full revolution trajectory.

The magnetic rigidity $B\rho$ by definition is

$$B\rho = \frac{p}{q} = \gamma \frac{mv}{q}. \quad (\text{A.10})$$

Differentiating Eq. (A.10) we obtain

$$d(B\rho) = \frac{\partial(B\rho)}{\partial(m/q)}d(m/q) + \frac{\partial(B\rho)}{\partial v}dv = \gamma v d(m/q) + (m/q)d(\gamma v) \quad (\text{A.11})$$

or

$$\frac{d(B\rho)}{B\rho} = \frac{d(m/q)}{m/q} + \frac{d(\gamma v)}{\gamma v} = \frac{d(m/q)}{m/q} + \frac{dv}{v}\gamma^2. \quad (\text{A.12})$$

Now inserting this into Eq. (A.9) and then the obtained expression for dC/C into Eq. (A.4) we have

$$\begin{aligned} \frac{df}{f} &= \frac{dv}{v} - \alpha_p \frac{d(B\rho)}{B\rho} = \frac{dv}{v} - \alpha_p \left(\frac{d(m/q)}{m/q} + \gamma^2 \frac{dv}{v} \right) = \\ &= -\alpha_p \frac{d(m/q)}{m/q} + \frac{dv}{v} (1 - \alpha_p \gamma^2). \end{aligned} \quad (\text{A.13})$$

Calculation of α_p

The compaction factor (non-linear ion-optical parameter of the ring) α_p can be calculated using the measured value of revolution frequency, the mass-to-charge ratio of identified ions (known from table) or/and the given values of the electron cooler voltage U_c and current I_c .

The electron cooler voltage and current determine the velocity of the cooling electrons and accordingly the velocities of all ions stored in the ring. This velocity (and Lorentz factor) can be calculated via

$$\gamma = \frac{U_{cr}}{m_e} + 1, \quad (\text{A.14})$$

$$\beta = \sqrt{1 - \frac{1}{\gamma^2}} = \frac{v}{c}, \quad (\text{A.15})$$

where m_e is the electron mass in eV and U_{cr} is the real voltage of the electron cooler and can be found by the following formula:

$$U_{cr} = U_c - \frac{113 \cdot I_c}{\sqrt{1 - \frac{1}{(U_c/m_e + 1)^2}}}. \quad (\text{A.16})$$

The path length of an ion per one revolution can be calculated by the formula

$$C = \frac{v}{f_r}, \quad (\text{A.17})$$

where $f_r = (f + LO)/h$ is the real frequency of the ion, f its frequency from spectrum (on h -th harmonic), LO the subtracted local-oscillator frequency and h is the signal harmonic.

The magnetic rigidity of a specified ion in Tesla-meters is

$$B\rho[Tm] = \frac{m}{q}v\gamma = \left(\frac{m}{q}\right)_{in\ u} \frac{a.m.u.[kg]}{e[C]}v \left[\frac{m}{s}\right] \gamma, \quad (A.18)$$

where m/q is the mass-to-charge ratio in atomic mass units, $a.m.u.[kg]$ the atomic mass unit value in kilograms and $e[C]$ the elementary charge value in Coulomb.

The α_p can be calculated using Eq. (A.1). There are two methods (see Fig. 3.8):

The first method is to calculate α_p from a single spectrum, where all ions have the same velocity and $\Delta v/v \rightarrow 0$, then one has

$$\alpha_p = -\frac{\Delta f}{f} \cdot \frac{m/q}{\Delta(m/q)}, \quad (A.19)$$

where f is obtained from spectrum and m/q is taken from the table, e.g. AME-03 [7], as peaks are identified. In order to find the dependence of the α_p on the path length C knowing the frequency f and the electron cooler settings (U_c and I_c), it is necessary to calculate the corresponding path length C using Eq. (A.14) – (A.17). For every pair of neighboring lines in a spectrum one has

$$\alpha_p\left(\frac{C_1 + C_2}{2}\right) = -\frac{f_1 - f_2}{f_1 + f_2} \cdot \frac{(m/q)_1 + (m/q)_2}{(m/q)_1 - (m/q)_2}. \quad (A.20)$$

The second method is to scan the frequency as a function of the electron cooler voltage U_c for one specified ion. Then $\Delta(m/q) = 0$ and

$$\alpha_p = \frac{1}{\gamma^2} \left(1 - \frac{\Delta f/f}{\Delta v/v}\right), \quad (A.21)$$

where v can be calculated using Eq. (A.14) – (A.16). For every two neighboring values of U_c one has

$$\alpha_p\left(\frac{C_1 + C_2}{2}\right) = \frac{4}{(\gamma_1 + \gamma_2)^2} \left(1 - \frac{(f_1 - f_2)/(f_1 + f_2)}{(v_1 - v_2)/(v_1 + v_2)}\right). \quad (A.22)$$

APPENDIX B

Software for data analysis

For the data analysis several programs were used. There are separate programs for the different steps of the analysis (see Section 4): for FFT, for the peak identification, for the spectra processing and for the mass evaluation, which are listed in Tab. B.1. Most of the programs are based on the ROOT libraries [98].

Tab. B.1: Software

getheaderinfo	reads information from the headers of blocks in TCAP .dat files.
root_fft	<ul style="list-style-type: none">• performs FFT with a given averaging number and a given number of blocks;• performs the peak finding in the created FFT spectrum;• performs Gaussian fitting of the found peaks.
roottrace	<ul style="list-style-type: none">• displays time-resolved 2D-spectra (many single spectra one above another);• corrects magnetic drifts in a 2D-spectrum with respect to a given reference peak;• allows for loading the found peak coordinates in ASCII format;• performs the “noise reduction” procedure automatically and allows for the manual one;• allows for loading the peak-identification information and for storing the data in the format $\langle frequency \rangle$ - $\langle identification \rangle$ for further mass evaluation.
twocalcit	<ul style="list-style-type: none">• calculates the α_p via two given frequencies and their identification;• identifies a particle via a given reference and the α_p value.
cmm	performs the mass evaluation by means of the CMM method.
mass_spline	performs the mass evaluation by means of the spline method.

APPENDIX C

The correlation matrix method

Introduction The dependence of the mass-to-charge ratio on the revolution frequency can be described with a P -degree polynomial for each spectrum:

$$\frac{m}{q} - \sum_{p=0}^P a_p(f)^p = l \pm \Delta, \quad (\text{C.1})$$

where m, q, f, l and Δ are functions defined in the lattice with indexes σ, η, ν , where

- $\sigma = 0, \dots, S - 1$ corresponds to spectrum index, with S — number of spectra;
- $\eta = 0, \dots, I - 1$ is an index counting different nuclides (Z, A) in spectra (different charge states of the same nucleus correspond to the same index η);
- $\nu = 0, 1, 2$ is a number of occurrences of a given nuclide in a given spectrum (can be 2 (or 3) in case the nuclide occurs in this spectrum in different charge states q).

Explicit form of Eq. (C.1) reads

$$\frac{m_{\sigma\eta\nu}}{q_{\sigma\eta\nu}} - \sum_{p=0}^P a_{\sigma p}(f_{\sigma\eta\nu})^p = l_{\sigma\eta\nu} \pm \Delta_{\sigma\eta\nu}. \quad (\text{C.2})$$

The deviations l of the mass-to-charge ratio from polynomial should be normally distributed around zero.

From Gaussian fitting (generated in the peak-finding procedure) one obtains the uncertainty of the frequency centroid and transforms it in the following way:

$$\Delta_{\sigma\eta\nu} = \frac{d \sum_p a_{\sigma p}(f_{\sigma\eta\nu})^p}{df_{\sigma\eta\nu}} \sigma_{f_{\sigma\eta\nu}}. \quad (\text{C.3})$$

In order to increase the number of correlations within the dataset one can transform all masses to the same charge state, e.g. to the bare ones, by subtracting electron masses and the corresponding electron binding energies, which are well-known [5, 6]:

$$m_{\sigma\eta\nu} = m_\eta + E_{\sigma\eta\nu}, \quad (\text{C.4})$$

$$E_{\sigma\eta\nu} = m_e \cdot (Z_\eta - q_{\sigma\eta\nu}) - BE(Z_\eta, Z_\eta - q_{\sigma\eta\nu}), \quad (\text{C.5})$$

where m_e is the electron mass and $BE(Z, Z - q)$ is the electron binding energy for a nucleus with Z protons and $(Z - q)$ electrons.

Due to correlations with other references in all spectra, reference masses may have some deviations from their table values (AME-03 [7])

$$m_r - m_r^c = l_r \pm \Delta m_r^c, \quad (\text{C.6})$$

where m_r are masses of nuclides used as references ($r = 0, \dots, R \in I$, where R is the total number of the references), m_r^c are table values for the reference masses and Δm_r^c are the uncertainties of these reference masses.

Maximum likelihood method The correlations between the polynomials can be taken into account by applying the maximum likelihood method [97]. One writes the joint probability density function (or likelihood function) L , which consists of the calibration likelihood function L_c and of the experimental likelihood function L_{exp} :

$$L = L_c \cdot L_{exp} = \prod_r f(l_r, \Delta m_r^c) \cdot \prod_{\sigma\eta\nu} f(l_{\sigma\eta\nu}, \Delta_{\sigma\eta\nu}), \quad (\text{C.7})$$

where $f(l, \sigma)$ is a Gaussian distribution

$$f(l, \sigma) = \frac{1}{\sqrt{2\pi}\sigma} \exp\left(-\frac{l^2}{2\sigma^2}\right). \quad (\text{C.8})$$

To find the maximum of L one solves the following equations:

$$\frac{\partial \ln L}{\partial a_{\sigma p}} = 0, \quad (\text{C.9})$$

$$\frac{\partial \ln L}{\partial m_\eta} = 0. \quad (\text{C.10})$$

Solving equations Let us solve Eq. (C.9).

$$\frac{\partial \ln L}{\partial a_{\sigma p}} = -\frac{1}{2} \frac{\partial}{\partial a_{\sigma p}} \left(\sum_{\sigma\eta\nu} \frac{\left(\frac{m_{\sigma\eta\nu}}{q_{\sigma\eta\nu}} - \sum_P a_{\sigma p} (f_{\sigma\eta\nu})^p \right)^2}{(\Delta_{\sigma\eta\nu})^2} \right) = 0. \quad (\text{C.11})$$

In what follows $\mathbf{f}_{\sigma\eta\nu}$ means a vector whose p^{th} element is $(f_{\sigma\eta\nu})^p$, thus $\sum_P a_{\sigma p} (f_{\sigma\eta\nu})^p$ replaced with $\mathbf{a}_\sigma \cdot \mathbf{f}_{\sigma\eta\nu}$, which is a scalar product of two vectors:

$$\sum_P a_{\sigma p} (f_{\sigma\eta\nu})^p = \mathbf{a}_\sigma \cdot \mathbf{f}_{\sigma\eta\nu} = \mathbf{a}_\sigma^T \mathbf{f}_{\sigma\eta\nu} = \begin{pmatrix} a_{\sigma 1} & a_{\sigma 2} & \cdots & a_{\sigma P} \end{pmatrix} \begin{pmatrix} 1 \\ f_{\sigma\eta\nu} \\ \vdots \\ f_{\sigma\eta\nu}^P \end{pmatrix}. \quad (\text{C.12})$$

Here we should note that for a given σ the summation $\sum_{\eta\nu}$ runs simply over all masses in this spectrum.

Although $\Delta_{\sigma\eta\nu}$ depend on coefficients $a_{\sigma p}$, we consider them as independent in the present run to simplify the equations (this will be discussed later, c.f. on page 76). After the differentiation we get $S \times (P + 1)$ equations for every $p = 0, \dots, P$ and every $\sigma = 0, \dots, S - 1$:

$$\sum_{\eta\nu} \frac{1}{(\Delta_{\sigma\eta\nu})^2} \left(\frac{m_{\sigma\eta\nu}}{q_{\sigma\eta\nu}} - (\mathbf{a}_\sigma \cdot \mathbf{f}_{\sigma\eta\nu}) \right) f_{\sigma\eta\nu}^p = 0 \quad (\text{C.13})$$

or

$$\sum_{\eta\nu} \frac{1}{(\Delta_{\sigma\eta\nu})^2} (\mathbf{a}_\sigma \cdot \mathbf{f}_{\sigma\eta\nu}) f_{\sigma\eta\nu}^p = \sum_{\eta\nu} \frac{1}{(\Delta_{\sigma\eta\nu})^2} \frac{m_{\sigma\eta\nu}}{q_{\sigma\eta\nu}} f_{\sigma\eta\nu}^p. \quad (\text{C.14})$$

For each σ the system of $(P + 1)$ equations can be written as

$$\mathbf{a}_\sigma \cdot \mathbf{A}_\sigma = \mathbf{b}_\sigma, \quad (\text{C.15})$$

where $(A_\sigma)_{p,q}$ and $b_{\sigma p}$ can be defined as:

$$(A_\sigma)_{p,q} = \sum_{\eta\nu} \frac{1}{(\Delta_{\sigma\eta\nu})^2} (f_{\sigma\eta\nu})^{p+q}, \quad p, q = 0, \dots, P \quad (\text{C.16})$$

$$b_{\sigma p} = \sum_{\eta\nu} \frac{1}{(\Delta_{\sigma\eta\nu})^2} \frac{m_{\sigma\eta\nu}}{q_{\sigma\eta\nu}} (f_{\sigma\eta\nu})^p. \quad (\text{C.17})$$

The solution for the vector \mathbf{a}_σ is

$$\mathbf{a}_\sigma = \mathbf{A}_\sigma^{-1} \mathbf{b}_\sigma, \quad (\text{C.18})$$

$$\mathbf{a}_\sigma = \mathbf{A}_\sigma^{-1} \sum_{\eta\nu} \frac{1}{(\Delta_{\sigma\eta\nu})^2} \frac{m_{\sigma\eta\nu}}{q_{\sigma\eta\nu}} \mathbf{f}_{\sigma\eta\nu}, \quad (\text{C.19})$$

where \mathbf{A} is a matrix $(P+1) \times (P+1)$. For each spectrum there is one matrix.

Now we will solve Eq. (C.10):

$$\frac{\partial \ln L}{\partial m_\eta} = -\frac{1}{2} \frac{\partial}{\partial m_\eta} \left[\sum_{r\eta} \delta_{r\eta} \frac{(m_\eta - m_\eta^c)^2}{(\Delta m_\eta^c)^2} + \sum_{\sigma\eta\nu} \frac{\left(\frac{m_{\sigma\eta\nu}}{q_{\sigma\eta\nu}} - \mathbf{a}_\sigma \cdot \mathbf{f}_{\sigma\eta\nu} \right)^2}{(\Delta_{\sigma\eta\nu})^2} \right] = 0.$$

For every mass with the index η we have an equation

$$\sum_{\sigma\nu} \frac{\frac{m_{\sigma\eta\nu}}{q_{\sigma\eta\nu}} - \mathbf{a}_\sigma \cdot \mathbf{f}_{\sigma\eta\nu}}{q_{\sigma\eta\nu} (\Delta_{\sigma\eta\nu})^2} = -\delta_{r\eta} \frac{m_\eta - m_\eta^c}{(\Delta m_\eta^c)^2}. \quad (\text{C.20})$$

If η is not a reference mass ($\eta \notin R$), then the right part is zero. In other case $m_r \equiv m_\eta$.

Now let us apply Eq. (C.4) and substitute \mathbf{a}_σ with Eq. (C.19):

$$\begin{aligned} & \sum_{\sigma\nu} \frac{m_\eta + E_{\sigma\eta\nu}}{(q_{\sigma\eta\nu})^2 (\Delta_{\sigma\eta\nu})^2} - \\ & \sum_{\sigma\nu} \frac{1}{q_{\sigma\eta\nu} (\Delta_{\sigma\eta\nu})^2} \left(\mathbf{A}_\sigma^{-1} \sum_{\theta\mu} \frac{m_\theta + E_{\sigma\theta\mu}}{q_{\sigma\theta\mu} (\Delta_{\sigma\theta\mu})^2} \mathbf{f}_{\sigma\theta\mu} \right) \mathbf{f}_{\sigma\eta\nu} = \\ & -\delta_{r\eta} \frac{m_\eta - m_\eta^c}{(\Delta m_\eta^c)^2}, \end{aligned} \quad (\text{C.21})$$

where $\theta = 0, \dots, I$ and $\mu = 0, 1, 2$.

$$\begin{aligned} & \sum_{\sigma\nu} \frac{m_\eta}{(q_{\sigma\eta\nu})^2 (\Delta_{\sigma\eta\nu})^2} - \sum_{\sigma\nu} \sum_{\theta\mu} \frac{m_\theta}{q_{\sigma\eta\nu} q_{\sigma\theta\mu} (\Delta_{\sigma\eta\nu})^2 (\Delta_{\sigma\theta\mu})^2} (\mathbf{A}_\sigma^{-1} \mathbf{f}_{\sigma\theta\mu}) \mathbf{f}_{\sigma\eta\nu} + \delta_{r\eta} \frac{m_\eta}{(\Delta m_\eta^c)^2} = \\ & - \sum_{\sigma\nu} \frac{E_{\sigma\eta\nu}}{(q_{\sigma\eta\nu})^2 (\Delta_{\sigma\eta\nu})^2} + \sum_{\sigma\nu} \sum_{\theta\mu} \frac{E_{\sigma\theta\mu}}{q_{\sigma\eta\nu} q_{\sigma\theta\mu} (\Delta_{\sigma\eta\nu})^2 (\Delta_{\sigma\theta\mu})^2} (\mathbf{A}_\sigma^{-1} \mathbf{f}_{\sigma\theta\mu}) \mathbf{f}_{\sigma\eta\nu} + \delta_{r\eta} \frac{m_\eta^c}{(\Delta m_\eta^c)^2}. \end{aligned} \quad (\text{C.22})$$

The term $\mathbf{A}_\sigma^{-1} \mathbf{f}_{\sigma\theta\mu} \mathbf{f}_{\sigma\eta\nu}$ is the scalar product of the vector $\mathbf{A}_\sigma^{-1} \mathbf{f}_{\sigma\theta\mu}$ with $\mathbf{f}_{\sigma\eta\nu}$, which gives us the number $\lambda = \lambda(\sigma, \eta, \nu, \theta, \mu)$:

$$\lambda = \left[\mathbf{A}_\sigma^{-1} \cdot \begin{pmatrix} 1 \\ f_{\sigma\theta\mu} \\ \vdots \\ (f_{\sigma\theta\mu})^P \end{pmatrix} \right] \cdot \begin{pmatrix} 1 & f_{\sigma\eta\nu} & \cdots & (f_{\sigma\eta\nu})^P \end{pmatrix} \quad (\text{C.23})$$

Now we can write

$$\mathbf{W}\mathbf{m} = \mathbf{v}, \quad (\text{C.24})$$

with

$$W_{\eta,\theta} = - \sum_{\sigma\nu} \sum_{\theta\mu} \frac{1}{q_{\sigma\eta\nu} q_{\sigma\theta\mu} (\Delta_{\sigma\eta\nu})^2 (\Delta_{\sigma\theta\mu})^2} \cdot \lambda \quad (\text{C.25})$$

$$W_{\eta,\eta} = \sum_{\sigma\nu} \frac{1}{(q_{\sigma\eta\nu})^2 (\Delta_{\sigma\eta\nu})^2} + \frac{1}{(\Delta m_r^c)^2} + W(\eta, \theta)|_{\eta=\theta} \quad (\text{C.26})$$

$$v_\eta = \frac{m_r^c}{(\Delta m_r^c)^2} + B_\eta \quad (\text{C.27})$$

$$B_\eta = - \sum_{\sigma\nu} \frac{E_{\sigma\eta\nu}}{(q_{\sigma\eta\nu})^2 (\Delta_{\sigma\eta\nu})^2} + \sum_{\sigma\nu} \sum_{\theta\mu} \frac{E_{\sigma\theta\mu}}{q_{\sigma\eta\nu} q_{\sigma\theta\mu} (\Delta_{\sigma\eta\nu})^2 (\Delta_{\sigma\theta\mu})^2} \cdot \lambda. \quad (\text{C.28})$$

$$(\text{C.29})$$

The matrix \mathbf{W} is a $I \times I$ matrix. And the \mathbf{m} is a vector with mass values. By solving Eq. (C.24) we can find the masses.

Iterations The program is working by iterations. For the first one $\Delta_{\sigma\eta\nu}$ were simply taken from a linear fit of the data. The next iteration uses $\Delta_{\sigma\eta\nu}$ calculated from previous one.

After solving Eq. (C.24) one can calculate coefficients $a_{\sigma p}$ applying Eq. (C.19):

$$\mathbf{a}_\sigma = \mathbf{A}_\sigma^{-1} \sum_{\eta\nu} \frac{1}{(\Delta_{\sigma\eta\nu})^2} \frac{m_\eta + E_{\sigma\eta\nu}}{q_{\sigma\eta\nu}} \mathbf{f}_{\sigma\eta\nu}, \quad (\text{C.30})$$

where m_η is the η^{th} element of the vector \mathbf{m} with calculated mass values. Then one can find $(\Delta_{\sigma\eta\nu})^2$

$$(\Delta_{\sigma\eta\nu})^2 = \left(\sum_p p a_{\sigma p} (f_{\sigma\eta\nu})^{p-1} \sigma_{f_{\sigma\eta\nu}} \right)^2. \quad (\text{C.31})$$

Uncertainty calculation The statistical errors can be estimated as the square root of the corresponding diagonal element of the inverted W matrix:

$$\sigma_{m_\eta}^{stat} = \sqrt{\mathbf{W}_{\eta\eta}^{-1}}. \quad (\text{C.32})$$

The systematic error can be estimated in the following way. Each reference nuclide is “switched off” and its mass is calculated as if it were unknown and its statistical uncertainty is found. Afterwards one can adjust the systematic error σ^{sys} using the equation:

$$\sum_{\eta=r=0}^R \frac{(m_r - m_r^c)^2}{(\Delta m_r^c)^2 + (\sigma_\eta^{st})^2 + (\sigma^{sys})^2} = R, \quad (\text{C.33})$$

where R is number of references.

Implementation in program The program code is based on the ROOT Matrix Linear Algebra package. Matrixes are numerically inverted by LU-decomposition method [97].

Bibliography

- [1] H.A. Enge, M.R. Wehr and J.A. Richards, Introduction to atomic physics. Addison-Wesley Pub. Co., (1972). (page 1)
- [2] AME 2013 preview: private Communication April 2011 by Georges Audi and Wang Meng. (page 3)
- [3] M. Dworschak *et al.*, [Phys. Rev. C](#) **81**, 064312 (2010). (page 3)
- [4] T. Beier *et al.*, [Can. J. Phys.](#) **80**, 1241 (2002). (page 3)
- [5] D.R. Plante *et al.*, [Phys. Rev. A](#) **49**, 3519 (1994). (pages 3, 43, 73)
- [6] G.C. Rodrigues *et al.*, [At. Data Nucl. Data Tables](#) **86**, 117 (2004). (pages 3, 43, 73)
- [7] G. Audi, H. Wapstra and C. Thibault, [Nucl. Phys. A](#) **729**, 337 (2003).
<http://amdc.in2p3.fr/web/masseval.html> (pages 3, 4, 5, 24, 41, 43, 48, 48, 49, 50, 66, 70, 73)
- [8] G.T. Garvey and I. Kelson, [Phys. Rev. Lett.](#) **16**, 197 (1966). (page 5)
- [9] I.O. Morales and A. Frank, [Phys. Rev. C](#) **83**, 054309 (2011). (page 5)
- [10] S.C. Pieper and R.B. Wiringa, [Annu. Rev. Nucl. Part. Sci.](#) **51**, 53 (2001). (page 5)
- [11] D. Lunney, J.M. Pearson and C. Thibault, [Rev. Mod. Phys.](#) **75**, 1021 (2003). (pages 5, 11)
- [12] <http://www.nuclearmasses.org/resources.html> (page 5)
- [13] C.F. von Weizsäcker, [Z. Phys.](#) **96**, 431 (1935). (page 5)
- [14] H.A. Bethe and R.F. Bacher, [Rev. Mod. Phys.](#) **8**, 82 (1936). (page 5)
- [15] V.M. Strutinski, [Nucl. Phys. A](#) **95**, 420 (1967); [Nucl. Phys. A](#) **122**, 1 (1968). (page 5)
- [16] J. Bardeen, L.N. Cooper and J.R. Schrieffer, [Phys. Rev.](#) **108**, 1175 (1957). (page 6)

- [17] P. Moller, J.R. Nix, W.D. Myres and W.J. Swiatecki, *At. Data and Nuc. Data Tables* **59**, 185 (1995). (pages 6, 8, 53, 54, 58)
- [18] P. Moller *et al.*, *Phys. Rev. Lett.* **108**, 052501 (2012). (page 6)
- [19] A. Sobiczewski and K. Pomorski, *Prog. Part. Nucl. Phys.* **58**, 292 (2007). (page 6)
- [20] S. Liran and N. Zeldes, *At. Data Nucl. Data Tables* **17**, 431 (1976). (page 6)
- [21] R.D. Woods and D.S. Saxon, *Phys. Rev.* **95**, 577 (1954). (page 6)
- [22] O. Haxel, J.H.D. Jensen and H.E. Suess, *Phys. Rev.* **75**, 1766 (1949). (page 7)
- [23] M. G. Mayer, *Phys. Rev.* **75**, 1969 (1949). (page 7)
- [24] T.H.R. Skyrme, *Phil. Mag.* **1**, 1043 (1956); *Nucl. Phys.* **9**, 615 (1959). (page 7)
- [25] D. Gogny, in Proceedings of the International Conference on Nuclear Self-consistent Fields, Trieste, 1975 (North-Holland, Amsterdam, 1975) (page 7)
- [26] D.R. Hartree, *Proc. Camb. Phil. Soc.* **24**, 89 (1928). (page 7)
- [27] V.A. Fock, *Z. Phys.* **61**, 126 (1930). (page 7)
- [28] P. Ring and P. Schuck, *The Nuclear Many-Body Problem*. Springer (1980). (pages 7, 17)
- [29] G.A. Lalazissis *et al.*, *At. Data Nucl. Data Tables* **71**, 1 (1999). (page 7)
- [30] S. Goriely, N. Chamel and J.M. Pearson, *Phys. Rev. C* **82**, 035804 (2010). (pages 8, 54, 54, 58)
- [31] S. Goriely, S. Hilaire, M. Girod and S. Peru, *Phys. Rev. Lett.* **102**, 242501 (2009). (pages 8, 54, 54)
- [32] J. Duflo and A.P. Zuker, *Phys. Rev. C* **52**, R23 (1995). (pages 8, 53, 54, 58)
- [33] M. Stanczak, *A Brief History of Copper*, (2005). (page 9)
- [34] *The History of Ancient Chemistry*. (pages 9, 10)
- [35] W. Reville, Robert Boyle, *The father of chemistry*, University College, Cork. (page 9)
- [36] Lavoisier, Antoine (1743-1794) — from Eric Weisstein's World of Scientific Biography, ScienceWorld. (page 9)
- [37] D.I. Mendeleev, *Principles of Chemistry*. New York: Collier. (1901);
D. Mendelejeff, *Zeitschrift für Chemie* **12**, 405 (1869) (page 10)

- [38] Yu.Ts. Oganessian *et al.*, *Phys. Rev. C* **74**, 044602 (2006). (page 10)
- [39] F. Soddy, *Chemical News* **107**, 97 (1913). (page 10)
- [40] J.J. Thomson, *Proceedings of the Royal Society, A* **89**, 1 (1913). (page 10)
- [41] F.W. Aston, *Nature (London)* **195**, 617 (1920). (page 10)
- [42] K.T. Bainbridge and E.B. Jordan, *Phys. Rev.* **50**, 282 (1936). (page 10)
- [43] A. Einstein, *Annal. Phys.* **18**, 639 (1905). (page 10)
- [44] B.G. Hogg and H.E. Duckworth, *Phys. Rev.* **91**, 1289-1290 (1953);
R. C. Barber *et al.*, *Phys. Rev. Lett.* **12**, 597 (1964). (page 10)
- [45] R. Klapisch *et al.*, *Phys. Rev. Lett.* **31**, 118 (1973). (page 10)
- [46] G. Audi, *Int. J. Mass Spectrom.* **251**, 85 (2006). (page 10)
- [47] B. Franzke, *Nucl. Instr. and Meth. in Phys. Res. B.* **24-25**, 18 (1987). (pages 11, 26)
- [48] W.L. Zhan *et al.*, *Nucl. Phys. A* **834**, 694 (2010). (page 11)
- [49] D. Lunney *et al.*, *Phys. Rev. C* **64**, 054311 (2001). (page 11)
- [50] H. Savajols, *Hyperne Interact.* **132**, 245 (2001). (page 11)
- [51] M. Matos *et al.*, *J. Phys. G: Nucl. Part. Phys.* **35**, 014045 (2008). (page 11)
- [52] H. Dehmelt, *Rev. Mod. Phys.* **62**, 525 (1990). (page 11)
- [53] W. Paul, *Rev. Mod. Phys.* **62**, 531 (1990). (page 11)
- [54] K. Blaum, *Phys. Rep.* **425**, 1 (2006). (pages 11, 11, 12, 12, 21)
- [55] B. Franzke *et al.*, *Phys. Scr. T* **59**, 176 (1995). (page 13)
- [56] M. Hausmann *et al.*, *Nucl. Instr. and Meth. A* **446**, 569 (2000). (page 13)
- [57] G.I. Budker, Rep. on Intern. Conf. at Orsay, (1966); "Atomnaya Energia" **22** (1967).(in Russian) (page 13)
- [58] C. Rubbia and S. van der Meer, Press Release: The 1984 Nobel Prize in Physics (page 13)
- [59] W. Mittig, A. Lépine-Szily and N.A. Orr, *Ann. Rev. Nucl. Part. Sci.* **47**, 27 (1997). (page 13)
- [60] Yu.A. Litvinov and F. Bosch, *Rep. Prog. Phys.* **74**, 016301 (2011). (page 13)

- [61] Yu.A. Litvinov, “Basic Nuclear Properties of Neutron-Deficient Nuclei Investigated via High Precision Mass Measurements in the Element Range of $36 \leq Z \leq 92$ ”, PhD thesis, Justus-Liebig Universität Giessen (2003). (pages 14, 28, 31, 42)
- [62] S. Hofmann *et al.*, *Zeitschrift für Physik A* **354**, 1 (1996). (page 14)
- [63] U. Köster *et al.*, *Nucl. Instr. and Meth. B* **204**, 347 (2003). (page 14)
- [64] M. Bernas *et al.*, *Phys Lett. B* **331**, 19 (1994). (page 14)
- [65] H.L. Ravn *et al.*, *Nucl. Instr. and Meth. B* **88**, 441 (1994). (page 14)
- [66] U. Köster, “Ausbeuten und Spektroskopie radioaktiver Isotope bei LOHENGRIN und ISOLDE”, PhD Thesis, Technische Universität, München (2000). (page 14)
- [67] H. Geissel, G. Münzenberg and K. Riisager, *Annu. Rev. Nucl. Part. Sci.* **45**, 163 (1995). (page 14)
- [68] D.J. Morrissey, *Eur. Phys. J. A* **15**, 105 (2002). (page 14)
- [69] U. Köster, *Nucl. Phys. A* **701**, 441 (2002). (page 15)
- [70] *Hyperfine Interactions* **129**, 1, ISOLDE - a laboratory portrait (2000). (page 15)
- [71] P. Bricault *et al.*, *Nucl. Phys. A* **701**, 49 (2002). (page 15)
- [72] J. Äystö, *Nucl. Phys. A* **693**, 477 (2001). (page 15)
- [73] http://en.wikipedia.org/wiki/Nuclear_binding_energy
M.P. Fewell, *American Journal of Physics* **63**, 653 (1995). (page 15)
- [74] P. Woods and C. Davids, *Annu. Rev. Nucl. Part. Sci.* **47**, 541 (1997). (page 17)
- [75] P.H. Stelson, F.K. McGowan, R.L. Robinson and W.T. Milner, *Phys. Rev. C* **2**, 2015 (1970). (page 17)
- [76] C.R. Hoffman, “Investigation of the neutron-rich oxygen isotopes at the drip line”, PhD thesis, Florida State University (2009). (page 17)
- [77] G. Scharff-Goldhaber, C.B. Dover and A.L. Goodman, *Ann. Rev. Nucl. Sci.* **26**, 239 (1976). (page 19, 19)
- [78] *The National Nuclear Data Center (NNDC)* (page 20)
- [79] E.M. Burbidge, G.R. Burbidge, W.A. Fowler and F. Hoyle, *Rev. Mod. Phys.* **29**, 547 (1957). (page 19)
- [80] I.S. Towner and J.C. Hardy, *J. Phys. G: Nucl. Part. Phys.* **29**, 197 (2003). (page 21)

- [81] S.R. Elliot and P. Vogel, *Annu. Rev. Nucl. Part. Sci.* **52**, 115 (2002). (page 21)
- [82] J.D. Vergados, *Phys. Rep.* **361**, 1 (2002). (page 21)
- [83] K. Blasche, D. Böhne, B. Franzke and H. Prange, *IEEE Transact. Nucl. Science* **32**, 2657 (1985). (page 22)
- [84] K. Sümmerer and B. Blank, *Phys. Rev. C* **61**, 034607 (2000). (pages 22, 24)
- [85] B. Tarasov and D. Bazin, *Nucl. Instr. and Meth. B* **226**, 4657 (2008).
<http://lise.nscl.msu.edu/lise.html> (page 24)
- [86] C. Scheidenberger *et al.*, *Nucl. Instr. and Meth. B* **142**, 441 (1998). (page 24)
- [87] H. Geissel *et al.*, *Nucl. Instr. and Meth. B* **70**, 286 (1992). (page 25)
- [88] T. Radon *et al.*, *Nucl. Phys. A* **677**, 75 (2000). (page 26)
- [89] M. Steck, *Nucl. Phys. A* **626**, 473 (1997). (page 28)
- [90] B. Schlitt, “Schottky Mass Spectrometry at the Heavy Ion Storage Ring ESR”, PhD Thesis, Universität Heidelberg (1997). (pages 28, 31)
- [91] T. Radon, “Massenmessung neutronenarmer Wismutfragmente am Experimentierspeicherring der GSI”, PhD Thesis, Justus-Liebig Universität Giessen (1998). (pages 28, 31, 42)
- [92] U. Schaaf, “Schottky-Diagnose und BTF-Messungen an Gekühlten Strahlen im Schwerionenspeicherring ESR”, PhD Thesis, Universität Frankfurt (1991). (page 30)
- [93] T. Beha, “Direkte Massenmessungen neutronenarmer Goldfragmente am Experimentierspeicherring der GSI”, PhD Thesis, Ludwig-Maximilians Universität München (1995). (page 31)
- [94] T. Kerscher, “Systematische Massenmessungen am Experimentierspeicherring der GSI”, PhD Thesis, Ludwig-Maximilians Universität München (1996). (page 31)
- [95] M. Falch, “Schottky Massenmessungen mit TCAP Datenaufnamesystem am Experimentierspeicherring der GSI”, PhD Thesis, Ludwig-Maximilians Universität München (2001). (page 31)
- [96] A. Papoulis, *Signal Analysis*, McGraw Int. Book Company, Tosho Printing, Tokyo (1977). (page 31)
- [97] W.H. Press, S.A. Teukolsky, W.T. Vetterling and B.P. Flannery, *Numerical Recipes* 3rd ed., Cambridge University Press (2007). (pages 31, 43, 45, 73, 77)

- [98] <http://root.cern.ch/drupal/> (pages 31, 33, 71)
- [99] R. Andrae, T. Schulze-Hartung and P. Melchior, [arXiv:1012.3754v1](#) (page 44)
- [100] G. Audi, O. Bersillon, J. Blachot and A.H. Wapstra, *Nucl. Phys. A* **729**, 3 (2003).
http://amdc.in2p3.fr/web/nubase_en.html (pages 48, 50)
- [101] Yu.A. Novikov *et al.*, *Nucl. Phys. A* **697**, 92 (2002). (page 53)
- [102] P. M. Walker and G. D. Dracoulis, *Hyperfine Interactions* **135**, 83 (2001). (page 54)
- [103] M.W. Reed *et al.*, *Phys. Rev. Lett.* **105**, 172501 (2010). (page 54)
- [104] R.F. Casten, D.S. Brenner and P.E. Haustein, *Phys. Rev. Lett.* **58**, 658 (1987). (page 57)
- [105] R.B. Cakirli *et al.*, *Phys. Rev. Lett.* **102**, 082501 (2009). (page 57)
- [106] Yu.A. Litvinov *et al.*, *Phys. Rev. Lett.* **95**, 042501 (2005). (page 58)
- [107] F. Nolden *et al.*, *Nucl. Instr. and Meth. A* **659**, 69 (2011). (page 62)
- [108] M.S. Sanjari, “Resonant pick-ups for non-destructive single-particle detection in heavy ion storage rings and first experimental results”, PhD thesis, Goethe-Universität, Frankfurt am Main (2012). (pages 62, 63)
- [109] F.-K. Thielemann, J. Metzinger und H.V. Klapdor, *Zeitschrift für Physik A. Hadrons and Nuclei*. **309**, 301 (1983). (page 62)
- [110] B. Sun *et al.*, *GSI Scientific Report* 2011. (page 63)
- [111] J.W. Xia *et al.*, *Nucl. Instrum. Methods A* **488**, 11 (2002). (pages 63, 64)
- [112] X.L. Tu *et al.*, *Phys. Rev. Lett.* **106**, 112501 (2011). (page 63)
- [113] Yu.A. Litvinov and H. Xu, *Nucl. Phys. News* **21**, 13 (2011). (page 63)
- [114] Y.-D. Zang *et al.*, *Chinese Phys. C* **35**, 1124 (2011). (page 63)
- [115] <http://www.fair-center.de> (page 65)
- [116] S. Litvinov, “Investigation of the Isochronous Mode of the Experimental Storage Ring (ESR) and the Collector Ring (CR). Decay Spectroscopy of Highly Charged Stored ^{140}Pr Ions at the FRS-ESR Facility”, PhD thesis, Justus-Liebig Universität Giessen (2008). (page 68)
- [117] M. Matos, “New Mass Measurements of Short-Lived Neutron Rich ^{238}U Fission Fragments at the FRS-ESR Facilities”, PhD thesis, Justus-Liebig Universität Giessen (2004). (page 68)

Acknowledgements

I would like to acknowledge the financial support of the International Max Planck Research School for Precision Tests of Fundamental Symmetries.

I want to thank my supervisors, Yuri Litvinov and Klaus Blaum. The former gave me an opportunity to perform my doctoral studies in nuclear physics in his group at GSI, while the latter granted me a privilege to work in his division of stored and cooled ions at MPIK.

I would not have accomplished my work without the help and support of Vladimir Skokov, who was for me an example of how one can love physics and perform research with passion.

I am very thankful to the people with whom I have been working and sharing an office at GSI through all these years, viz., Shahab Sanjari and Nicolas Winckler. Shahab, you demonstrated to me how to not be afraid of new things and how to be confident in my abilities to learn them. Nicolas, looking at you I realized how to become an expert in something without efforts and being driven only by interest. Thank you both for those hours of discussions about the ultimate question of life, the universe and everything.

I want to thank Fritz Bosch, who has been very kind to me since my very first day at GSI, when he gave me a tour around the experimental facilities. I appreciate that Fritz always has been caring toward me and my work all this time.

I also acknowledge all my collaborators and GSI staff for their contribution to my research.